Material Processing and Forming Approaches for Enhancing Room Temperature Formability of Automotive Mg Sheet

Material Processing and Forming Approaches for Enhancing Room Temperature Formability of Automotive Mg Sheet

By
Mahdi Habibnejad-korayem, B.Sc., M.Sc.

A Thesis

Submitted to the School of Graduate Studies

in Partial Fulfillment of the Requirements

for the Degree

Doctor of Philosophy

McMaster University

Ph.D. Candidate (2015) McMaster University
Mechanical Engineering Hamilton, Ontario

TITLE: **Material Processing and Forming approaches for Enhancing Room Temperature Formability of Automotive Mg Sheet**

AUTHOR: Mahdi Habibnejad-Korayem
B.Sc. (University of Tehran)
M.Sc. (University of Tehran)

SUPERVISOR: Professor Mukesh K. Jain

NUMBER OF PAGES: viii, 151

Abstract

Automotive magnesium sheets typically exhibit poor room temperature ductility which makes them unsuitable for room temperature sheet stamping applications. This research involved aspects of re-processing and forming of AZ31 automotive magnesium sheet to improve its room temperature ductility and bendability (and, more generally, formability). The sheet re-processing studies for formability improvement were carried out by two different methods, (i) cyclic bending-unbending and annealing (or CBUA) and (ii) wire brushing and annealing (or WBA). These two processing methods led to a complex stress and strain distribution through the thickness and a multi-layered microstructure after annealing. The grain structure, micro-texture, and micro-hardness of each of the layers were studied by optical microscopy, electron back-scattered diffraction (EBSD) and indentation measurements, respectively. The through-thickness grain structure study indicated grain refinement and texture randomization in the surface layers for both CBUA and WBA processed materials.

In addition, the as-received (and fully annealed) sheet as well as processed materials were subsequently deformed in uniaxial tension and bending by a process referred to in the literature as pre-strain annealing (or PSA). The PSA process was studied as a single step as well as multi-step process to assess its effect on formability improvement, underlying changes in microstructural and mechanical behavior, and to explore practical limitations and advantages of the process.

The results from single-step PSA process were also used to develop a microstructure-based constitutive material model to capture and predict the observed mechanical and microstructural response of AZ31 sheet to PSA variables. This model explicitly considered the effect of recovery on recrystallization kinetics, and non-constant nucleation and growth rate. The model was extended to predict the grain size at the end of recrystallization and within the grain growth stage as well as post-PSA yield and work hardening characteristics. The mechanical property prediction was based on considering the microstructure as a composite of un-recrystallized, recrystallized and coarsened grain structure and by employing a rule of mixture.

The processing and forming methods led to significantly increased cumulative uniaxial tensile ductility and plane strain cumulative bendability of AZ31 sheet at room temperature depending upon PSA process parameters. The experimental and modeling studies collectively helped correlate mechanical properties from various processing conditions and forming methods with microstructural parameters, and to explain the improvement in room temperature formability based on microstructural and textural considerations.

Research Contributions

- Two new material processing methods of cyclic bending-unbending and annealing (CBUA) and wire brushing and annealing (WBA) for enhancing room temperature uniaxial tensile ductility and bendability of AZ31 sheet were developed. The CBUA method led to surface grain refinement and through thickness texture modification and to improved bendability from minimum radius to sheet thickness value of 2.92 to 2.32. Surface grain refinement (from 10 μm to 2.5 μm up to a depth of about 40 μm) and texture randomization on the sub-surface layer of AZ31 to a depth of 30 μm were achieved from wire brushing and annealing. The modified microstructure and texture resulted in increased uniaxial tensile strain from 0.22 to 0.32. Fundamental studies related to these processes were carried out at the microstructural level to understand how microstructure affects the mechanical properties.

- Two forming methods of multi-step uniaxial stretching and annealing (MUSA) and multi-step bending and annealing (MBA) were developed to enhance room temperature formability of AZ31 sheet. Cumulative uniaxial tensile ductility equivalent to that from high temperature (400˚C) continuous tensile was achieved at room temperature in several steps. Also, cumulative bendability values similar to those from high temperature bending of AZ31 in the literature were achieved using the MBA process. Fundamental studies related to these forming processes were carried out at the microstructural level to understand how microstructure affects the mechanical properties and bendability.

- A microstructure-based model to analyze the effect of single-step pre-straining and annealing related phenomena such as recovery, recrystallization, and grain growth kinetics based on nucleation rate, dislocation density, grain growth and stored energy considerations was developed. The model was further extended to predict post-annealing mechanical properties.

Acknowledgements

Firstly, I would like to express my gratitude to my PhD supervisor, Prof. Mukesh Jain for his continued support throughout my research work. I am grateful for his constant encouragement and invaluable mentorship while providing me with a remarkable freedom to explore new ideas in my own way.

I would also like to thank Dr. Raja Mishra of General Motors R and D Center, Warren, MI, USA, Profs. Marek Niewczak, Hatem Zurob, Joseph McDermid and Sumanth Shankar from McMaster University for their valuable suggestions and advice.

Special thanks are also to the Department of Mechanical Engineering at McMaster University, McMaster Automotive Recourse Center (MARC), General Motors Research and Development Center, Warren, MI, USA and Natural Sciences and Engineering Research Council (NSERC) of Canada for their financial support. My sincere thanks also go to Mr. Robert Kubic from General Motors, Ron Lodewyks, Doug Kelly, Michael Lee, Jim McLaren, Jim Cleaver, Martin Wensveen, Victoria Jarvis, Drs. Anantheshwara Kommunje, Grzegorz Mitukiewicz, and Moisei Bruhis for their technical support and advice during different phases of my research. I would also like to acknowledge Vania Loyzer and all other administrative staff of Department of Mechanical Engineering for their support.

In my day-to-day activities, I have been blessed with the company of many friendly and cheerful fellow students, Dr. Michael Nemcko, Dr. Ania Kula, Dr. Fumiaki Huira, Mr. Ali Mazahery, Dr. MD Kashif Rehman, Mr. Shenglong Liang, Dr. Ganesh Govindasami, Mr. Mahmud Marzuk, and Dr. Morteza Yousef Sanaati. All have generously helped with suggestions throughout my research.

Last but not least, I would like to thank my family and express my love and gratitude to my parents Mrs. Mahnaz Habibnejad-korayem, Mr. Akbar Habibnejad-korayem and my sister Aazam Habibnejad-Korayem for their endless love and spiritual support. Finally, I would like to thank God for giving me the opportunity and the ability to proceed with my doctoral research work.

Table of Contents

List of Acronyms

AB	Alternate bending
ARB	Accumulative roll bonding
ASTM	American Society for Testing and Materials
CBU	Cyclic bending-unbending
CBUA	Cyclic bending-unbending and annealing
CI	Confidence index
CRSS	Critical resolved shear stress
CTC	Compression-Tension-Compression
DBS	Draw bead simulator
EBSD	Electron backscatter diffraction
ECAE	Equal channel angular extrusion
ECAP	Equal channel angular pressing
ECAR	Equal channel angular rolling
FESEM	Field emission scanning electron microscope
FIB	Focused ion beam
FLD	Forming limit diagram
FSW	Friction stir welding
HAGB	High angle grain boundary
HCB	Hot cyclic bending
HCP	Hexagonal close packed
IPF	Inverse pole figure
IQ	Image quality
JMAK	Johnson-Mehl-Avrami-Kolmogorov
LDR	Limit drawing ratio
LT	Longitudinal transverse
MBA	Multi-step bending and annealing
MFA	Multi-step forming and annealing
MTS	Mechanical test system
MUSA	Multi-step uniaxial stretching and annealing
ND	Normal direction
OIM	Orientation image microscopy
PF	pole figure
PFSA	Pre-forming and subsequent annealing
PSA	Pre-strain annealing
RD	Rolling direction
RPM	Revolution per minute
RUB	Repeated unidirectional bending
SFE	Stacking fault energy

SEM	Scanning electron microscopy
SIBM	Strain induced boundary migration
SMAT	Surface mechanical attrition treatment
SPD	Severe plastic deformation
SP	Shot Peening
TCT	Tension-Compression-Tension
TD	Transverse direction
TEM	Tunneling electron microscopy
UTS	Ultimate tensile strength
WB	Wire brushing
WBA	Wire brushing and annealing
WHR	Work hardening rate
XRD	X-ray diffraction

Chapter 1
Introduction

[1]. Introduction

Attention has been focused globally in the recent years in the use of Mg sheet for automotive applications due to its lower density (1.74 g/cm^3) compared to the other commonly used automotive sheet materials such as steel and aluminum (Mg has a density of about a quarter of steel and two thirds of aluminum). Lower density and therefore reduced vehicle weight can translate into increased fuel economy and lesser environmental footprint. Magnesium alloys also possess reasonably high specific modulus and strength, good castability (suitable for high pressure die casting), good machinability and good weldability under a controlled atmosphere [1]. Despite these advantages and due to their hexagonal close-packed (hcp) structure and limited slip systems, they have poor formability at room temperature which slows down their adaptation in automotive body applications. A number of experimental studies exist for forming magnesium and its commercial alloys at temperatures above 300˚C. At these temperatures, thermally activated slip enables the activation of additional slip systems and a reduction in critical resolved shear stress (CRSS) for plastic flow. Enhanced slip activity gives rise to good formability in magnesium alloys. However, due to higher process costs and lower part quality at high temperature there is considerable interest in pursuing lower temperature forming methods for Mg sheet. Various solutions such as grain structure and forming process optimization through well controlled and novel experiments hold the promise of expanding the forming capability of Mg to lower temperatures. In view of the fact that refining the grain size and randomizing the texture could result in enhancement of Magnesium alloys' poor formability at room temperature, a number of thermo-mechanical processing techniques mostly based on severe plastic deformation have been explored over the years [2-7]. These processing methods, however, are costly and rather difficult to put into practice on a plant-scale. Among these, newly patented process of room temperature pre-forming, annealing, and subsequent forming has been utilized as a promising method for further investigation in this thesis to enhance the room temperature formability of Mg alloys. The primary governing mechanisms in this process result in grain size and texture changes. However, these mechanisms have not been studied sufficiently in the literature for AZ31 sheet. Specifically, this process has been largely employed as a single-step process in the literature where formability improvement is rather limited. The methodology essentially consists of introduction of an annealing step between preforming and forming operations to soften the pre-strained material. The literature review indicates that exploring several types of two-stage strain path experiments to improve the formability of Al and Mg alloys has been mostly a subject of the researchers in this process. Uniaxial tension and equi-biaxial strain path experiments, with deformation in the plane and out-of-plane, of the deforming sheet materials have been mostly utilized in the studies [8-14]. The process, for example, has been demonstrated feasible to produce Aluminum made inner door panel with complex shape that could not be formed in a single continuous operation at room temperature [8]. The effects of uniaxial tensile pre-strain values, annealing times, and annealing temperatures have been experimentally investigated on the elongation, yield stress and strain-hardening exponent of aluminum alloy AA5182-O by Li et. al [9]. They also developed a model to show the strength softening that occurs during the annealing stage of this process. In another study by the same authors, the Aluminum alloy was pre-strained in uniaxial tension, plane strain and equibiaxial tension to several equivalent strain levels and different annealing conditions to study the dependence of post-annealing mechanical properties and anisotropy to pre-strain and annealing history [10]. In another study by Li et al. [11], the effect of pre-strain annealing (PSA) process parameters on prediction of forming limit diagrams (or FLDs) was studied. In this work, a two-stage stress-based forming diagram (σ-FLDs) was obtained. Such a diagram was found to be sensitive to pre-strain levels, strain paths and annealing. Based on the strain energy principle, Min et al [12] employed an equivalent strain to evaluate the effects of the pre-strain and annealing process on the total limit equivalent strain of the PSA processed material. They also managed to improve uniaxial ductility of ZEK100 magnesium alloy by this process [13]. In a separate study, the stretch formability of AZ31 magnesium alloy has been reported to improve by this process [14]. The literature review indicates that the potential of pre-forming and annealing process as a multi-step forming process will require assessment of its overall potential in terms of cumulative formability and commercial viability.

In addition, pre-processing Mg sheet materials via processes based on local severe plastic deformation such as cyclic bending-unbending have been given due consideration in this thesis to improve room temperature formability of Mg sheet. This process is more practical method that is easy to implement in sheet production units. In fact, it already exists in the form of roller leveling in many rolling facilities. Different processes such as repeated unidirectional bending (RUB) [15,16], hot cyclic bending (HCB) [17,18], wire brushing (WB) [19-21], shot peening (SP) [22] and surface mechanical attrition treatment (SMAT) [23] have been employed in various studies to improve forming of sheet materials. However, in these studies the focus has been to improve monotonic uniaxial ductility or dome stretchability of processed sheet, and relatively little attention has been given to improve performance of Mg sheet materials in other important forming modes such as plane strain bending or cumulative uniaxial tensile ductility during multi-step forming. Also, these processes have not been followed by an annealing step to further modify the resulting microstructure and to improve the subsequent properties.

This thesis therefore attempts to fill these gaps by further studies of cyclic bending-unbending and annealing and wire brushing and annealing processes which are based on room temperature deformation and annealing at higher temperatures to improve monotonic and cumulative ductility and bendability of AZ31 sheet materials. Also, pre-straining and annealing method has been extended to a multi-step uniaxial tension and plane strain bending deformation modes. The physical and mechanical responses of AZ31 during single step PSA process are also analyzed by developing a comprehensive microstructure based model. This model provides some useful insight into the effect of pre-strain and annealing parameters on modifying the grain recrystallization and growth kinetics and consequently the mechanical properties that has not been available in the literature.

[1.1]. Research Objectives

The general objective of the thesis was to improve the room temperature sheet formability of automotive AZ31 sheet for stamping applications. The research objectives thus consisted of the following specific objectives:

(i) Re-processing of the as-received H-24 temper sheet by novel and practical (i.e., more efficient and economical) methods and evaluation of microstructural and textural changes and consequent effect on uniaxial tensile and plane strain bending behavior,

(ii) Forming the as-received H-24 temper sheet by full annealing followed by one or more steps of pre-strain and intermediate annealing and evaluation of microstructural and textural changes and consequent effect on uniaxial tensile and bending behavior, and

(iii) Development of a microstructure based material constitutive models to capture and predict the observed microstructural and mechanical response from single-step uniaxial pre-straining and annealing history.

The above objectives were addressed by conducting a broad set of processing and forming experiments at larger specimen-scale as well as at smaller microstructural-scale to establish the optimum conditions for maximum gain in formability as well as present the limitations of the various processes. The experimental results for single-step pre-strain annealing process were used to develop a microstructure-scale model to capture the room temperature mechanical and grain-level microstructural response of AZ31 sheet. Two methods of re-processing were considered for improving uniaxial tensile ductility and plane strain bendability, (a) cyclic bending-unbending and annealing (CBUA) utilizing a roller bending device, and (b) wire brushing followed by annealing (WBA). For direct forming of the as-received and fully annealed sheet, with no reprocessing in the laboratory, two different modes of pre-straining were employed, (a) multi-step uniaxial straining and subsequent annealing (MUSA) and (b) multi-step bending and annealing (MBA) processes.

[1.2]. Thesis Organization

Subsequent chapters of the thesis are organized as follows:

Chapter 2. This chapter presents results from a single step pre-straining and annealing (PSA) process to understand the uniaxial deformation behavior during pre-straining, subsequent annealing as well as post-PSA mechanical response of the material. Pre-straining and post-annealing mechanical responses, such as yield strength, UTS and ductility are analyzed and correlated with static recovery, grain recrystallization and growth characteristics from annealing. Experimental results are then utilized to develop and validate a microstructure-based material model to capture the room temperature mechanical and grain-level microstructural response of AZ31 sheet from the PSA process. The model incorporates the effect of recovery on the recrystallization kinetics, as well as non-constant nucleation and growth rates in order to predict the grain size at the end of recrystallization and within the grain growth stage. The mechanical response from the model is validated with additional experiments in terms of two critical PSA process parameters, pre-strain value and temperature of annealing. The content of this chapter is presented in the journal paper format that will be submitted for publication to a peer reviewed journal.

Chapter 3. This chapter deals with an investigation of room temperature multi-step uniaxial stretching and subsequent annealing (or MUSA) process. The microstructural (grain size) and texture changes and corresponding mechanical responses are studied for three different MUSA conditions. Details of this process as well as observed mechanisms and property improvements are described in this chapter. This study has been published as a paper in *Materials Science and Engineering A* [24].

Chapter 4. This chapter deals with re-processing of AZ31 sheet by wire brushing and annealing (WBA) process to modify the surface layer microstructure of AZ31. The wire brushing process was carried out using softer brass wire brushes to mitigate the effect of wire brushing on surface quality and damage. The influence of modified surface grain structure and crystallographic texture was studied by continuous uniaxial tension test as well as by the MUSA process of Chapter 3 to assess its cumulative uniaxial tensile ductility. Material flow stress behavior, grain microstructure and texture evolution of WBA processed material during subsequent MUSA process were analyzed to assess the role of wire brushing in enhancing the MUSA response of AZ31 sheet. Original fully annealed AZ31 sheet (in the non-WBA condition) was also subjected to identical MUSA process for comparison purposes. Parts of this work have been published as a short paper in archived journal of *Materials Forum* [25]. Additionally, a draft manuscript containing a more expanded set of results and a more extensive discussion section has been prepared for submission to a peer reviewed journal. Both of these papers are included in this Chapter.

Chapter 5. This chapter describes a study involving multi-step bending and annealing (MBA) process to assess room temperature cumulative bendability of AZ31 sheet. V-bending tests were conducted to assess cumulative bendability by conducting a large number of intermediate bends and anneals. The deformation mechanisms during the MBA process were studied by Scanning Electron Microscopy (SEM) and Electron Backscattered Diffraction study. Significant improvement in bendability was achieved from the MBA process. The results are also compared with the earlier MUSA of Chapter 3. This study has been published in *Materials Science and Engineering A* [26].

Chapter 6. This chapter describes another re-processing method for room temperature formability improvement of AZ31 sheet and is referred to as multi-step cyclic bending-unbending and annealing (CBUA) method. The re-processing resulted in a 5-layer microstructure through the sheet thickness with very fine grains at the two sheet surfaces and improved monotonic bendability. The grain structure, micro-texture, and micro-hardness of each of the layers were studied by optical microscopy, electron back-scattered diffraction (EBSD) and indentation measurements, respectively. The results were analyzed in terms of mechanics of cyclic bending-unbending (CBU) process, mechanisms of strain induced static recrystallization, texture evolution and its stability with long term annealing. Also, bending load-displacement response of the processed material was studied by conducting sharp monotonic V-bending tests. This study has been accepted for publication in *Materials Science and Engineering A*.

Chapter 7. This short chapter presents a final discussion which links elements of the previous chapters into a common theme.

Chapter 8.This chapter contains the main conclusions of this study as well as some suggestions for future research work.

References

The following references were utilized in sections 1.1 and 1.2 of this Chapter.

[1]. B. L. Mordike, T. Ebert, Mater. Sci. Eng. A 302 (2001) 37–45.
[2]. J. A. Del Valle, F. Carreno, O. A. Ruano, Acta Mater. 54 (2006) 4247-4259.
[3]. J. Koike, Metall. Mater. Trans. A, 36A (2005) 1689-1696.
[4]. J. H. Cho, H. W. Kim, S. B. Kang, T. S. Han, Acta Mater. 59 (2011) 5638-5651.
[5]. S. R. Agnew, J. A. Horton, T. M. Lillo, D. W. Brown, Scripta Mater., 50 (2004) 377-381.
[6]. X. Huang, K. Suzuki, A. Watazu, I. Shigematsu, N. Saito, Mater. Sci. Eng. A 488 (2008) 214-220.
[7]. W. Yuan, R. S. Mishra, Mater Sci Eng A 558 (2012) 716-724.
[8]. T. M. Lee, S. E. Hartfield-Wünsch, S. Xu, Demonstration of the preform anneal process to form a one-piece Aluminum door inner panel. SAE Paper No. 2006-01-0987.
[9]. J. J. Li, S. Kim, T. M. Lee, P. E. Krajewski, H. Wang, S. J. Hu, The effect of prestrain and subsequent annealing on the mechanical behavior of AA5182-O, Mater. Sci. Eng. A 582 (2011) 3905-3914.
[10]. J. J. Li, S. J. Hu, J. E. Carsley, T. M. Lee, L. G. Hector Jr., S. Mishra, Post Annealing Mechanical Properties of Formed AA5182-O Sheet, ASME 2011 International Manufacturing Science and Engineering Conference, Volume 1, Corvallis, Oregon, USA, June 13–17, 2011.
[11]. J. J. Li, J. E. Carsley, T. B. Stoughton, L. G. Hector Jr., S. J. Hu, Forming limit analysis for two-stage forming of 5182-O aluminum sheet with intermediate annealing, IJP, 45 (2013) 21–43.
[12]. J. Min, J. Lin, J. J. Li, Mater. Des. 53 (2014) 947–953.
[13]. J. Min, J, T. Carter, R. Verma, Magnesium Technology 2012, 443-448.
[14]. H. Zhang, G. Huang, L. Wang, J. Li, Scripta Mater., 67 (2012) 495-499.
[15]. G. Huang, H. Li, B. Song, L. Zhang, T. Nonferr, Metal. Soc., 20 (2010) 28-33.
[16]. L. Zhang, G. Huang, H. Li, and B. Song, J. Mater. Process. Tech., 211 (2011) 644-649.
[17]. Y. Jiang, X. Yang, L. Zhang, Mater. Sci. Forum, 667-669 (2011) 623-527.
[18]. Q. Huo, X. Yang, J. Ma, H. Sun, J. Qin, Y. Jiang, Mater. Charact. (2013) 43–51.
[19]. M. Sato, N. Tsuji, Y. Minamino, Y. Koizumi, Sci. Tech. Adv. Mater. 5 (2004) 145–152.
[20]. H. Kitahara, T. Yada, F. Hashiguchi, M. Tsushida, S. Ando, Surf. Coat. Technol. 243 (2014) 28-33.
[21]. K. Dehghani, M. Nasirizadeh, S. Bagherzadeh, Proc. IMechE, 224 (2010) 190-198.
[22]. Z. Jin, O. Xingbin, Y. Donghua, S. Zhifu, Journal of Wuhan University of Technology-Mater. Sci. Ed. (2009) 515-519.
[23]. H. Q. Sun, Y. N. Shi, M. X. Zhang, K. Lu, Acta Mater. 55 (2007) 975–982.
[24] M. Habibnejad-korayem, M. K. Jain, R. K. Mishra, Mater. Sci. Eng. A. 619 (2014) 370–377.
[25] M. Habibnejad-korayem, M. K. Jain, R. K. Mishra, Mater. Sci. Forum, 828-829 (2015) 340-344.
[26] M. Habibnejad-korayem, M. K. Jain, R. K. Mishra, Mater. Sci. Eng. A. 619 (2014) 378-383.

Chapter 2

Modeling of uniaxially pre-strained and annealed AZ31 Magnesium sheet based on microstructural considerations

The study reported in this chapter was mostly conducted by this doctoral candidate (Mahdi Habibnejad-korayem) with continuous supervision over a period of 4 .5 years by his supervisor, Dr. Jain, and occasional technical advice from Dr. Mishra of General Motors (GM), the industrial sponsor of the project. Dr. Zurob, Associate Professor, in the Department of Materials Science and Engineering at McMaster, suggested the infrastructure for the modeling work and helped with formulation of some of the components the model. The chapter was prepared by this candidate with many discussions of its structure, focus, content, conclusions, language, and writing style with Dr. Jain.

Modeling of Uniaxially Pre-strained and Annealed AZ31 Magnesium Sheet based on Microstructural Considerations

Mahdi Habibnejad-korayem [a,1], Mukesh K. Jain [a], Hatem S. Zurob [b], Raja. K. Mishra [c]

a McMaster University, Department of Mechanical Engineering, Hamilton, ON, Canada L8S4L8
b McMaster University, Department of Materials Science and Engineering, Hamilton, ON, Canada L8S4L8
b General Motors Research and Development Center, Warren, MI 48090, USA

Abstract

Material deformation at room temperature and subsequent thermal aspects are analyzed at the microstructural level to understand the uniaxial deformation behavior of AZ31 magnesium sheet from pre-straining and annealing (PSA) process. The sheet is pre-strained to various strains by conducting interrupted tests and its uniaxial stress-strain responses are obtained. The pre-strained specimens are then annealed at different temperatures and times and then reloaded in uniaxial tension to obtain their post-anneal stress-strain response up to large strains. Pre and post-annealing mechanical responses are analyzed and correlated with static recovery, grain recrystallization and growth kinetics from annealing. Experimental results are utilized to develop and validate a microstructure-based model to capture the room temperature mechanical and grain-level responses of AZ31 sheet from the PSA process. The model incorporates the effect of recovery on the recrystallization kinetics, as well as non-constant nucleation and growth behavior in order to predict the grain size at the end of recrystallization and within the grain growth stage. In addition, the mechanical properties of PSA materials are predicted by considering the resulting microstructure as a composite of un-recrystallized, recrystallized and coarsened grain regions and by employing the rule of mixture. Nomenclatures in this paper are presented in Table 2.1.

Keywords: magnesium sheet; pre-strain; annealing; recrystallization; modeling

---

[1] Corresponding author. Tel.: +1-905-906-7770; fax: +1 905-525-9140. E-mail address: habibnm@mcmaster.ca.

Table 2.1. Nomenclatures

Symbols	Names of parameters and quantities
b	Magnitude of the Burgers vector
β	Constant
C_{Zn}	Concentration of Zn in solution
C_{Al}	Concentration of Al in solution
D_0	Initial grain size of material
D_{bulk}	Bulk self-diffusion coefficient
D_e	Effective grain size
Dgb	Grain boundary self-diffusion coefficient of Mg
D_{rex}	Grain size in recrystallized region
D_x	Cross-boundary diffusion coefficient
D	Average grain size in coarsening stage
$dV_{rex-growth}$	Increase in recrystallized volume
E	Young’s modulus
E_b	Binding energy of Al and Zn to grain boundaries
F	Driving force for grain growth
F(t)	Fraction of sub-grains reached to the critical size
$F_n(t)$	Un-recrystallized fraction of grain boundaries available for nucleation
$\frac{\partial f}{\partial t}$	Change in fraction of sub-grains with time
G(t)	Stored energy
k	Boltzman’s constant
k_{ad}	Sub-grains factor
K_{HP}	Hall-Petch coefficient
K_H	Hollomon strength coefficient
L	Spacing of pinning centers
M_T	Taylor factor
M(t)	Mobility of high-angle grain boundaries
M_{pure}	Intrinsic grain boundary mobility
M_{sg}	Average mobility of the sub-grain boundary
$\frac{\partial N}{\partial t}$	Nucleation rate
N_{rex}	Maximum number of recrystallization nuclei
N(t)	Number of nuclei as a function of time
$N_{sg}(t)$	Number of sub-grains touching the grain boundary per unit volume
n_t	Number of twins
n	Strain hardening exponent
N_v	Number of atoms per unit volume
Rg	Gas constant
S_v	Deformed grain boundary area per unit volume
T	Temperature
t	Time
U_a	Activation enthalpy of the operating recovery process
V_a	Activation volume of the operating recovery process

symbols	Names of parameters and quantities
V_d	Debye frequency
X	Recrystallized volume fraction
$\mathrm{r_c(t)}$	Critical size of the recrystallization nucleus
$\mathrm{r(t)}$	Average sub-grain radius with time
$r_{c,t}$	Critical radius of nuclei at time t
$< r_t >$	Average sub-grain radius at time t
$\mathrm{r_0}$	Average initial sub-grain radius
$< r >$	Average size of sub-grain structure
$\mathrm{R_i}$	Initial radius of the deformed grains
$\mathrm{R(t)}$	Instantaneous radius of gun-recrystallized region
$\mathrm{R_0}$	Initial radius of grains
$\mathrm{V_0}$	Volume of the deformed grains
$\mathrm{V_{shell}}$	Volume of outer shell of the deformed grains
$\mathrm{V_{rex}}$	Total volume of recrystallized grains within the volume of outer shell of the deformed grains
V_{un-rex}	Un-recrystallized volume per grain
α_m	Cahn's solute drag factor
α_{gr}	Geometric constant
$\mathrm{\alpha_m}$	Interaction parameter in Cahn's solute-drag model
α	Taylor constant
$\Delta\mathrm{t}$	Elapsed time from completion of recrystallization
σ_{rex}	Flow stress in recrystallized region
σ_{un-rex}	Flow stress in un-recrystallized region
ε_R	Residual pre-strain in the un-recrystallized region
Ω	Fraction of yield stress in un-recrystallized region before and after annealing
γ_{gb}	Grain-boundary energy
δ	Thickness of the grain boundary
μ, μ_T, μ_{RT}	Shear moduli
$\rho, \rho(t)$	Dislocation density
σ_{un-rex}	Flow stress of the un-recrystallized material
${\sigma_y}_{rex}$	Yield stress of fully recrystallized material
${\sigma_y}_{un-rex}$	Yield stress of recovered material
$\mathrm{\sigma_D}$	Stress change due to dislocations

[2.1]. Introduction

Pre-strain annealing has been proposed as a viable method of forming difficult to form materials at room temperature into useful components [1]. In this process, as illustrated in Fig. 2.1, the sheet material is first pre-strained at room temperature close to its uniaxial tensile uniform strain limit and subsequently annealed to remove the cold work. It is then reloaded in the same deformation mode to the final desired strain.

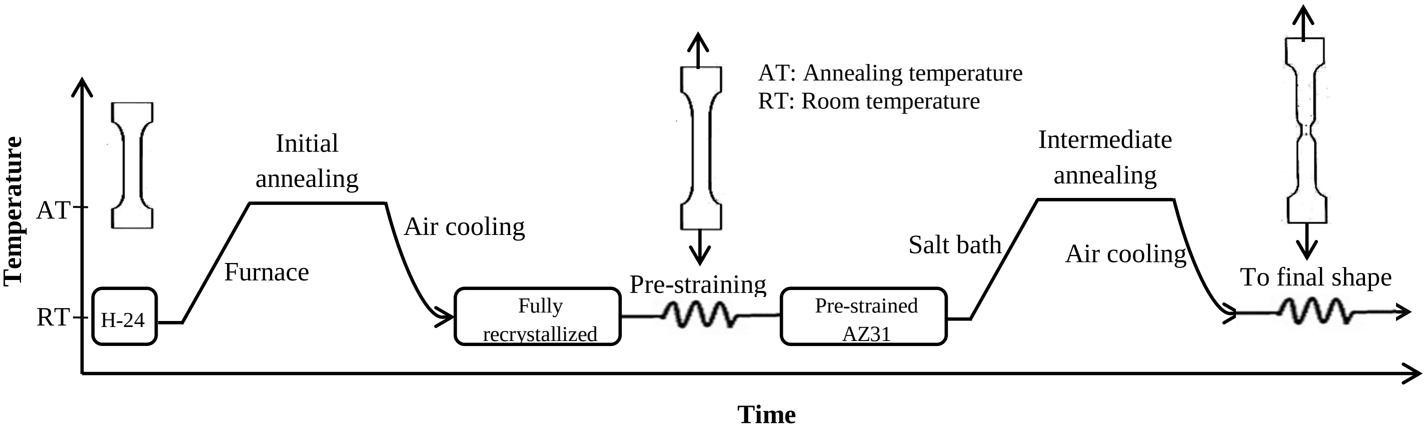

Fig. 2.1. A schematic illustration of pre-straining and subsequent annealing process.

Depending on the amount of desired strain, the process could be performed in a single step or extended to a multi-step pre-strain and annealing (MPSA) process. This process has been successfully utilized to improve sheet formability of different materials including Al and Mg alloys at room temperature [2-6]. Such a process exploits the potential of a specific alloy system to enhance its cumulative ductility by pre-straining and annealing processes while avoiding the effect of damage at large strains. More specifically, the capacity of the material to transform the stored plastic strain energy within its microstructure from pre-straining drives the annealing induced recovery, recrystallization and grain growth (RRG) and determines the extent to which it can be deformed in each PSA step. Also, the choice of pre-strain and annealing parameters (temperature and time) have been shown to be critically related to microstructure and formability parameters such as uniaxial tensile ductility and limit strain under monotonic loading. A range of pre-strains with a minima and maxima is recommended based on the kinetics of RRG processes and development of damage in the material at large strains at each of the PSA steps [4-6]. In the present work, a physically based model of single step PSA process is proposed by analyzing the kinetics of RRG processes at the microstructural level. The model is then extended to predict the room temperature uniaxial tensile stress-strain behaviour of post-PSA AZ31 sheet. In development of this ‘unified’ model of annealing behavior and post-annealing response, extensive use is made of well-accepted microstructure-based models in the literature that describe the RRG process kinetics in metallic alloy systems. For example, the model utilizes the approach that is developed by Verdier et al. [7] to account for the drop in stored energy as an instantaneous driving force for recovery and recrystallization. Also the recrystallization models that have been developed by Zurob and coworkers [8-10] are adopted to predict different features of recovery and recrystallization. These models capture experimentally observed competition between recovery and recrystallization and a variable grain nucleation and growth rate. It is to be noted that the aforementioned models have been successfully employed to predict recrystallization kinetics of oxygen free Cu and Al-1 % Mg [8], Zr-alloys [9], and a micro-alloyed steel [10]. In the present work, they are utilized to predict the static recrystallization of uniaxially pre-strained and annealed AZ31 sheet, where the effect of initial grain size is modified by considering twin formation in AZ31 sheet. The model is also extended to predict grain size in partially and fully recrystallized materials and to estimate the grain growth after complete recrystallization. Further, the model is extended to predict the yield stress and plastic flow stress of reloaded material after pre-straining and annealing. Before proceeding with the details of the model, a brief description of the experimental PSA procedure and some experimental results and observations are in order.

[2.2]. Experimental procedure, results and observations

[2.2.1] Experimental procedure

For PSA experiments, a rather large set of AZ31 sheet samples were pre-strained in rolling direction in uniaxial tension to strains of 0.05, 0.01, 0.15 and 0.17 at room temperature. For each pre-strained set of samples, annealing was carried out at 200˚C, 300˚C and 400˚C for 1 min, 15 min and 60 min in a salt bath followed by cooling in air at room temperature. All 36 sets of PSA samples (4 pre-strains, 3 annealing temperatures and 3 times) were then pulled to fracture at room temperature while recording the load versus displacement data. Details of mechanical testing and microstructural characterization procedure could be found in recent publications by the authors [2, 3].

[2.2.2]. Mechanical response from PSA process

True stress-strain curves from unloaded and reloaded uniaxial tension tests, with no intermediate annealing, are shown in Fig. 2.2(a). The flow curves of the samples from this process followed rather closely the original flow stress curve at zero pre-strain. However, a slight over-shoot can be noted in the elastic-plastic transition region on reloading as well as a progressive increase in the yield strength of reloaded samples with pre-strain. Similar two-stage flow curves were obtained for PSA samples in an effort to isolate the effect of annealing parameters on subsequent flow behavior on reloading. Selected uniaxial stress-strain curves from PSA samples are shown in Figure 2.2(b) where the extent of uniform flow region on reloading is shown to depend on the amount of pre-strain and annealing conditions. The stresses in general rapidly approach the end of the previous deformation step on re-loading at the annealing temperature of 200˚C. On annealing at higher temperatures, however, not only the stress in the reloading stage increases even more slowly but also the maximum stress is reduced. The reloading curves are generally dispersed into 2 separate narrow bands of characteristic hardening responses (see Fig. 2.2(c)) which depend on the resulting grain structure from the underlying recrystallization and grain growth processes (as discussed in the subsequent section). In terms of post-annealing elongation on reloading, the results are indicative of lower values for PSA processed samples compared to the monotonic loading of fully annealed material. Among these, elongations on reloading after annealing at 200˚C, and at lower pre-strain values, seem larger than the other annealing conditions. Although longer time annealing slightly improved the post-annealing elongations, higher annealing temperatures (300˚C and 400˚C) significantly dropped the post annealing elongations for the 0.05 and 0.10 pre-strained material. Therefore, improvement in cumulative strain could only be achieved under certain PSA conditions. At a given temperature of annealing, the improvement in cumulative elongation becomes more evident with increasing pre-strains.

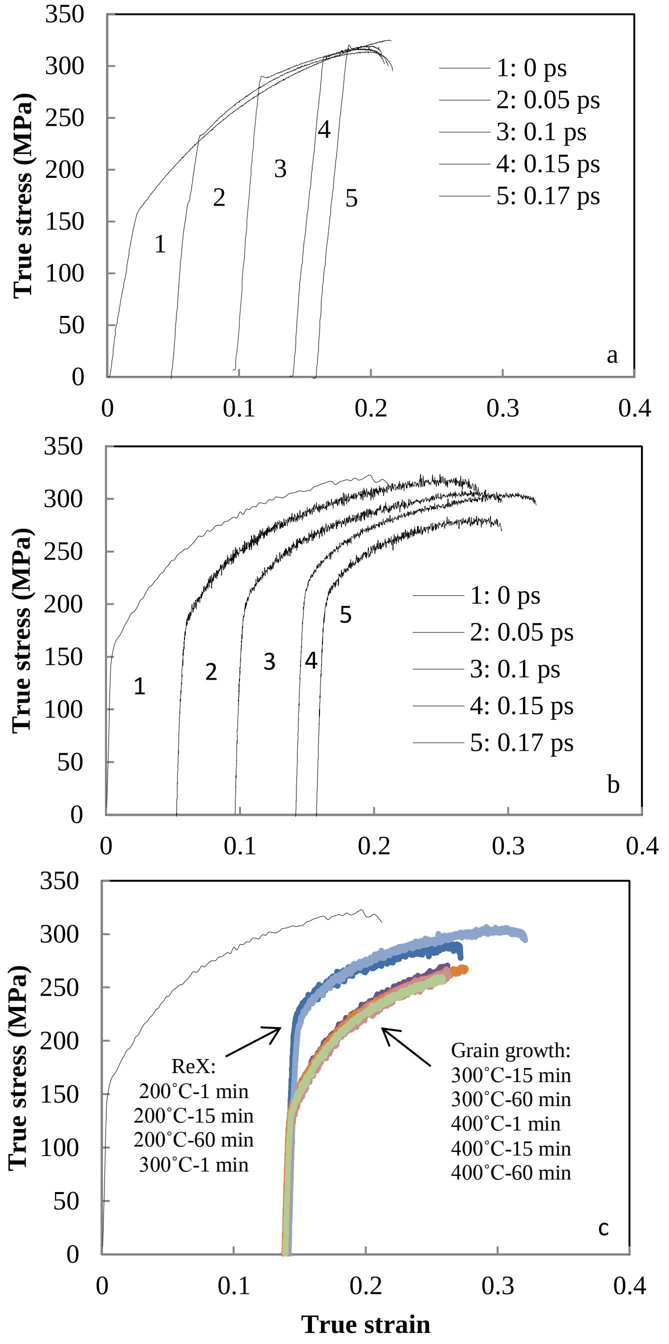

Fig. 2.2. Flow behavior of AZ31, under (a) pre-straining at different strains, unloading and reloading to fracture, (b) pre-straining at different strains followed by annealing and reloading to fracture (200˚C-60 min), (c) subset data of PSA process at pre-strain of 0.15 for various annealing temperature and times. In figure 2.2(c), the temperatures and times for recrystallization and growth are identified.

[2.2.3]. Microstructural observations from long term annealing

Fig. 2.3 shows a set of micrographs from the ST plane from long term annealing experiments at selected pre-strains, annealing temperatures and times. The following characteristics of grain structure can be noted in these micrographs: (i) abnormal grain growth (Fig. 2.3(a)), (ii) grain refinement (Fig. 2.3(b)), (iii) partial grain growth (Fig. 2.3(c)), and (iv) normal (or uniform) grain growth (Fig. 2.3(d)) depending upon the PSA parameters. Material with a pre-strain of 0.05 exhibited no evidence of recrystallization and grain shape change in short term annealing at 200˚C. However, as the annealing continued, a small amount of recrystallization occurred first and some abnormal grain growth also occurred at longer times. The abnormal growth was more noticeable at 300˚C and 400˚C (see Fig. 2.3(a)). Conversely, pre-strains larger than 0.05 could activate recrystallization at smaller annealing times (see Fig. 2.3(b-d)). At higher temperatures of annealing, grains started to grow earlier resulting in a larger average grain size.

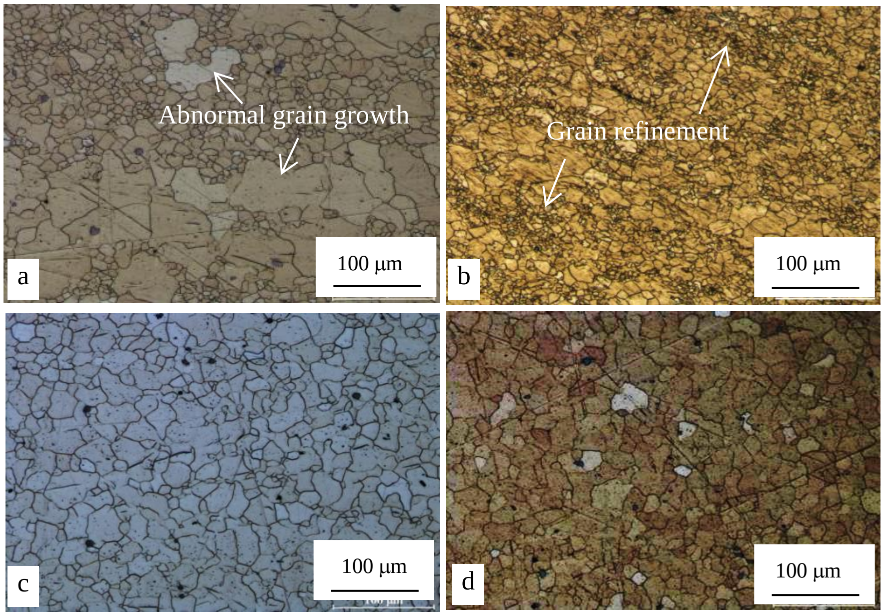

Fig. 2.3. Selected optical micrographs showing the grain structure of PSA processed materials at various pre-strains, temperature and times, (a) 0.05-400˚C-480s, (b) 0.15-300˚C-20s, (i) 0.10-300˚C-180s, (d) 0.17-400˚C-60s.

[2.3]. Model Development

[2.3.1]. Model background

During isothermal annealing of pre-strained materials, the stored energy is released by recovery and further reduction in stored energy is caused by recrystallization and grain growth processes. For high stacking fault energy materials, such as Mg alloys, recovery typically involves annihilation and rearrangement of dislocations into sub-grains and growth of sub-grains over time [11]. One of the most commonly used models in literature for prediction of recovery is the dislocation based model proposed by Verdier et al. [7]. This model is employed in the present study to estimate the drop in driving force and quantify the dislocation density during annealing. Although this model presents evolution of yield stress related to the variation in the total dislocation density, it can be used for Mg alloys because the twin contribution in uniaxial tensile yielding is limited due to the presence of a strong basal texture from rolling.

In addition to recovery, a large portion of stored energy is released due to recrystallization during annealing. Grain recrystallization during annealing has been typically modeled by classical JMAK equation [11]. This equation is rather simple and easy to use but embodies idealised assumptions such as a constant grain nucleation and growth rate. Experimental observations on different metals provides clear evidence that nucleation rate is typically not constant and the recovery takes place concurrently with recrystallization leading to a non-constant driving force, and therefore to a non-constant growth rate [11–14]. Particularly noteworthy is the attempt by Cahn [15] towards modification of JMAK equation to include a heterogeneous nucleation model. Also, other efforts have been made to include recovery effect on the recrystallization kinetics in the JMAK model [16, 17]. However, the influence of recovery on concurrent recrystallization has not been subjected to an in-depth analysis. It is to be noted that attempts have been made to develop alternative models to incorporate the competition between recovery and recrystallization and non-constant nucleation and growth rates during isothermal annealing of single phase alloys. One of these models [8, 9] has been used in the present work for the recrystallization kinetics of AZ31. Also, in the present work, a detailed description of the nucleation process and the effect of solute drag on the growth of the recrystallized grains are considered based on the recent work of Kashif Rehman [10].

Subsequent to recrystallization, grain growth occurs to further release the stored energy of pre-strained material. The normal grain growth theory by Hillert [18] which is suggested for the grain growth of single-phase materials is employed in this study to predict the grain size of AZ31 after complete recrystallization. Lastly, in the present PSA model, post-anneal mechanical properties are predicted by utilizing a 'rule of mixture' analysis between recrystallized and un-recrystallized regions [19].

[2.3.2]. Model framework

A general flow chart of the proposed PSA model is presented in Fig. 2.4 where the main calculation modules and the interrelationships amongst them can be noted.

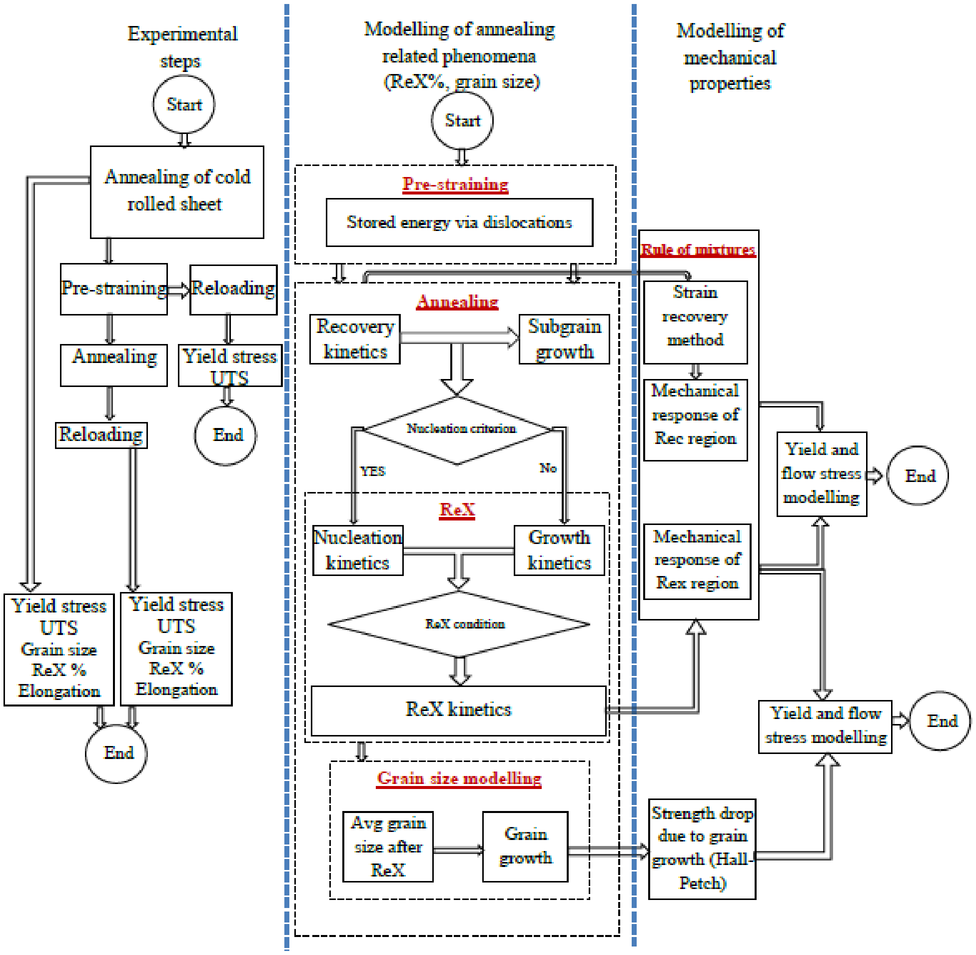

Fig. 2.4. Flowchart of model framework. The left column represents the experimental components of the model.

The model formulation starts with a quantification of stored energy from pre-straining and its dissipation during recovery and recrystallization processes. This is considered in terms of yield strength increase due to dislocation storage during pre-straining and its decrease during annealing. Also, the sub-grain growth is tracked in the model and a nucleation criterion is applied to identify the start of nucleation [28]. Calculation proceeds with the prediction of growth rate of nuclei and the fraction of recrystallization based on the original deformed volume of grains and recrystallized volumes in nucleation and growth stages. Subsequently, grain size is estimated at the end of recrystallization and during the grain growth stage. Finally, by considering the resulting microstructure as a composite of recrystallized and un-recrystallized regions, and also by taking Hall-Petch effect into account, the resulted mechanical properties are predicted. Further details related to the various sub-modules and the associated equations are presented in the following sub-sections.

[2.3.3]. Model assumptions

The basic model assumptions are itemized as follows:

[1]. AZ31 sheet is precipitate-free before and after annealing.

[2]. Stored energy in PSA is in the form of stored dislocations that are distributed uniformly throughout the microstructure. Stored energy from twinning is neglected due to basal texture of as-received material which tends to supress twin formation in uniaxial deformation [2, 3, 20].

[3]. Deformed microstructure consists of spherical grains and the effect of twining is included in the ‘effective’ grain size. Twin’s type and thickness effect are neglected in the calculation.

[4]. Progress of recovery during annealing is assumed to reduce the available driving force for recrystallization and thus slow down the rate of recrystallization.

[5]. A reduction in stored energy during the recovery process is measured by yield drop which is related to the dislocation density [7].

[6]. Recrystallization occurs by strain induced boundary migration (SIBM) [21] which is applicable to Mg alloys at pre-strains in the range of 0.05 – 0.17 [22].

[7]. Recrystallized nuclei only form on sub-grains near the grain boundaries [11, 21, 22].

[8]. Grain nucleation and growth occur at non-constant rate [23, 24].

[9]. A competition between recrystallization and recovery processes is considered in the model development based on experimental results reported in the literature [23,24].

[10]. In partially recrystallized material, the microstructure is considered as a composite of recrystallized and un-recrystallized regions, and in completely recrystallized material, the microstructure is taken as a composite of recrystallized and grown grains.

[11]. Textural changes and damage developments are neglected in the present single step PSA process based on experimental results [2, 3].

[2.3.4] Model Formulation

[2.3.4.1]. Recovery Kinetics

The driving force for recovery and recrystallization in the model stems from disparity in stored energy, G(t), in the recrystallized and un-recrystallized regions of the microstructure. The relationship between stored energy and dislocation density, ρ is expressed as [8-10]:

$$\mathrm{G(t)} = \frac{1}{2}\rho(\mathrm{t}).\mu.\mathrm{b}^2 \tag{2.1}$$

where $\rho(\mathrm{t}), \mu,$ and b are total dislocation density in the material as a function of time t, shear modulus and Burgers vector respectively. It is to be noted that dislocation density in the un-recrystallized region, and consequently, the stored energy for recrystallization, decreases during recovery due to lower dislocation content in the material. Therefore, time-dependent static recovery and dislocation density in the un-recrystallized material is expected to be related to the driving force for recrystallization. For simplicity, and to avoid laborious dislocation density measurements, the dislocation density can be estimated from the following relationship between flow stress during annealing, $\sigma_\mathrm{D}(\mathrm{t})$, and the yield stress of material in its fully recrystallized state, $\sigma_{\mathrm{y}_\mathrm{rex}}$ [7]:

$$\sigma_\mathrm{D}(\mathrm{t}) = \sigma_{\mathrm{y}_\mathrm{rex}} + \mathrm{M_T}.\alpha.\mu.\mathrm{b}.\sqrt{\rho(\mathrm{t})} \tag{2.2}$$

where the constant α is a dimensionless number and $\mathrm{M_T}$ is the Taylor Factor for Mg alloys. The recovery kinetics of $\sigma_D(t)$ based on relaxation of the internal stresses from annihilation of dislocations generated during pre-straining can be expressed as [7, 25]:

$$\frac{\mathrm{d}\sigma_\mathrm{D}}{\mathrm{dt}} = \frac{-64.\sigma_\mathrm{D}{}^2\mathrm{v_d}}{9\mathrm{M}^3\alpha\mathrm{E}}.\exp\left(\frac{-\mathrm{U_a}}{\mathrm{R_g.T}}\right)\mathrm{Sinh}\left(\frac{\sigma_\mathrm{D}\mathrm{V_a}}{\mathrm{KT}}\right) \tag{2.3}$$

where $\mathrm{R_g}$ is the gas constant, $\mathrm{U_a}$ is the activation energy which can be approximated to that of self-diffusion in Mg [26], $\mathrm{v_d}$ and E are the Debye frequency and Young's modulus, T is temperature in Kelvin, $\mathrm{V_a}$ is the activation volume for the recovery process and K is Boltzman's constant. Once the above ordinary differential equation of recovery kinetics is solved for $\sigma_D(t)$, Eq. (2.2) can be rearranged to obtain $\rho(t)$. The instantaneous dislocation density is utilized later in the nucleation criterion for recrystallization in sub-section 2.3.4.3.

[2.3.4.2]. Sub-grain growth

As the recovery occurs and stored energy decreases, sub-grains with lower energy start to grow in size in radial direction from the center to provide a condition for nucleation (as discussed later in sub-section 2.3.4.3). The instantaneous average sub-grain size <r(t)> during annealing can be described by considering the initial average sub-grain size r_0 and a growth rate of sub-grains in the following intergral form [8-10]:

$$< r(t) > = < r_0 > + \int_0^t M_{sg}.V_{sg}.dt \tag{2.4}$$

where M_{sg} is the average mobility of sub-grain boundary (a low angle boundary) and V_{sg} is the velocity of sub-grain growth. The function inside the integral could be referred to as the growth rate of a given sub-grain and is derived in reference [10] based on migration of dislocations. This term is expressed as

$$M_{sg}.V_{sg} = 2\frac{D_{bulk}}{L}\sinh(\frac{k_{ad}\sigma_D b^2 L}{KT}) \tag{2.5}$$

where D_{bulk} is the bulk self-diffusion coefficient, L is the spacing of pinning centers and k_{ad} is sub-grain factor.

[2.3.4.3]. Nucleation criterion

As with most of nucleation models, it is considered that a region of a crystal becomes a nucleus and grows only if its size exceeds some minimum value [27]. Also, SIBM, a common nucleation mechanism in many polycrystalline metallic materials [28], is assumed to occur during PSA. Based on studies in the literature on AZ31 sheet, a well-defined sub-strain structure after deformation has been shown to be present, and SIBM has been suggested as a mechanism for grain nucleation during annealing [22,24]. As annealing continues, nucleation sites become available for sub-grains touching the grain boundaries and having a lower dislocation density than their surroundings (Figure 2.5(a)). Once the sub-grain grows, the migrating boundary sweeps up the dislocation and create strain free grains (see Fig. 2.5(b)). Grain boundary bulging occurs when the boundary curvature term ($\frac{2.\gamma}{r(t)}$ where γ is the boundary energy) decreases due to growth of sub-grains (i.e., increasing r(t)) until it drops below the instantaneous value of the stored energy as shown in (Fig. 2.5(c)). This gives the following criterion for nucleation stage of recrystallization [28]:

$$\frac{1}{2}.\rho(t).\mu.b^2 > \frac{2.\gamma}{r(t)} \tag{2.6}$$

The sub-grain size (r(t)) that first meets this condition is considered as the critical size of the recrystallization nucleus (r_c) above which bulging occurs into the neighboring grain to provide viable nuclei for recrystallization.

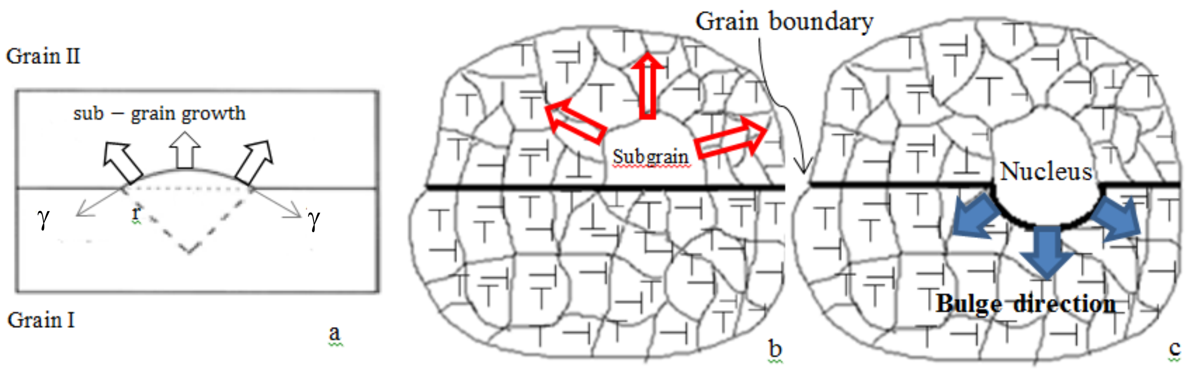

Fig. 2.5. Schematic illustration of nucleation mechanism by strain induced boundary migration (SIBM) showing, (a) bowing of single sub-grain boundary, (b) sub-grain growth within the deformed microstructure, and (c) nucleation of new grain (adapted from reference [8]).

[2.3.4.4]. Nucleation kinetics

Once the nucleation criterion is met, a number of nuclei form within the microstructure and recrystallization begins. The instantaneous number of nuclei can be readily calculated by considering the fraction of sub-grains that form viable nuclei (f(t)), the number of sub-grains touching the grain boundary per unit volume, ($N_{sg}(t)$), and a function $F_n(t)$ to make up for the progressive depletion of nucleation sites [10]. The above quantities can be linked together to yield the following expression for nucleation rate:

$$\frac{dN(t)}{dt} = \frac{df(t)}{dt}.N_{sg}(t).F_n(t) \tag{2.7}$$

Integration of this equation gives the instantaneous number of nuclei, N(t). The nature of associated terms, $f(t)$, $N_{sg}(t)$ and $F_n(t)$ that constitute N(t) are discussed separately in the next 3 sub-sections.

[2.3.4.4.1]. Fraction of sub-grains forming viable nuclei

The fraction of sub-grains which have the potential to grow to the point of becoming high angle grain boundary (HAGB) and form viable nuclei is given by [8-10, 24]:

$$f(t) = \exp\left(-\frac{\pi.\chi_c(t)^2}{4}\right) - \exp\left(-\frac{\pi.3^2}{4}\right) \qquad (2.8)$$

where $\chi_c(t)$ is the normalized critical sub-grain size and is given by $\frac{r_c(t)}{<r(t)>}$ where $r_c(t)$ is the critical radius of sub-grains and $< r(t) >$ is the average sub-grain size.

[2.3.4.4.2]. Number of sub-grains contacting the grain boundary

By considering the potential number of nucleation sites per unit surface area as $\frac{1}{\pi<r(t)>^2}$, the number of sub-grains, $N_{sg}(t)$, touching the grain boundary per unit volume can be estimated as[10]:

$$N_{sg}(t) = \frac{Sv}{\pi.<r(t)^2>} \qquad (2.9)$$

where *S*v is the deformed grain boundary area per unit volume for spherical grains and is equal to $\frac{3}{D_e}$ where D_e is the effective grain size [10]. D_e can be assumed to equal to $\frac{D_0}{1+n_t}$ due to twin formation where D_0 is the original grain size and n_t is the number of twins [29]. The grain structure of pre-strained AZ31 in tension is illustrated in Fig. 2.6 where the grain boundaries and twins are marked in blue and red respectively. For example, the twin boundaries (belonging to seven twins) are shown to split five grains (marked by black arrows in Fig. 2.6(a)) to eleven grains in Fig. 2.6(b)) resulting in 1/8th reduction in the original grain size.

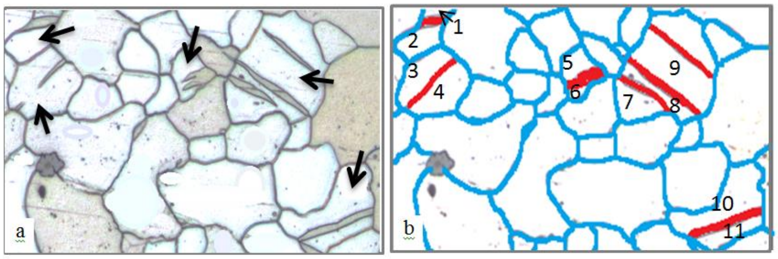

Fig. 2.6. Grain structure of pre-strained material showing, (a) twin formation within the grains, and (b) grains subdivision by twin formation (the colors blue and red indicate grain and twin boundaries respectively).

[2.3.4.4.3]. Non-recrystallized fraction of the surface shell

As mentioned earlier, only sub-grains touching the grain boundaries can act as potential nucleation sites, and therefore, nuclei would typically start to form on a shell near the grain boundary, as shown in Fig. 2.7(a). To mathematically consider progressive depletion of nucleation sites on this shell (see Fig. 2.7(b)), a new parameter can be defined as [10]:

$$\mathrm{F_n(t)} = 1 - \frac{\mathrm{V_{rex-nucleation}}}{\mathrm{V_{shell}}} \tag{2.10}$$

where $\mathrm{V_{rex-nucleation}}$ is the volume of recrystallized grains (explained later in section 2.3.4.5) within the volume of outer spherical shell of deformed grains, $\mathrm{V_{shell}}$. The latter can be taken to be equal to $4\pi\delta R_i^2$ where $\mathrm{R_i}$ is the initial radius of the deformed grains and δ is the thickness of the grain boundary region.

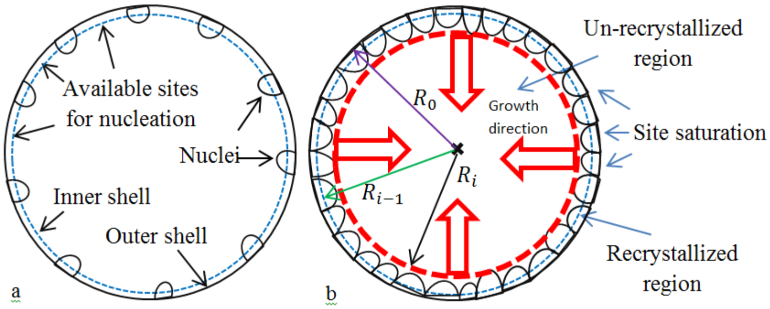

Fig. 2.7. Schematic illustration of nucleation by SIBM mechanism, at (a) an earlier stage of nucleation where sites are still available for nucleation, and at (b) a later stage of recrystallization showing the movement of recrystallization front (adapted from reference [10]).

[2.3.4.5]. Volume of recrystallized grains

The calculation of volume of recrystallized grains based on the stage of recrystallization (see Fig. 2.8) and availability of nucleation sites on the outer shell is discussed in the following subsections.

[2.3.4.5.1]. Recrystallized volume in nucleation stage of recrystallization

Before depletion of nucleation sites, the volume of recrystallized grains, $\mathrm{V_{rex-nucleation}}$, could be defined by Eq. (2.11) assuming that they bulge and grow to a semi-spherical shape as:

$$\mathrm{V_{rex-nucleation}} = \frac{1}{2}.\left[\frac{4}{3}.\pi. < r(t)^3 >\right] \tag{2.11}$$

where <r(t)> is the average radius of recrystallized grain. This quantity can be calculated by replacing the growth term in Eq. (2.4) for high angle grain boundaries (HAGB) with $\int_0^t \mathrm{M.G(t).dt}$ [8-10]. In the growth term here, M is HAGB mobility which is measured in terms of Cahn's solute drag expression [30]:

$$\mathrm{M} = \left(\frac{1}{\mathrm{M_{pure}}} + \alpha_m.\mathrm{C_{Al}} + \alpha_m.\mathrm{C_{Zn}}\right)^{-1} \tag{2.12}$$

where $\mathrm{C_{Al}}$ and $\mathrm{C_{Zn}}$ denote the concentrations of Al and Zn in AZ31 and $\mathrm{M_{pure}}$ was defined as the intrinsic mobility of grain boundaries for the pure matrix [30] and can be stated for Mg as follows [23, 26, 31]:

$$\mathrm{M_{pure}} = 5.286\times10^{-7}\ \exp\left(\frac{-69233}{\mathrm{R_g T}}\right) \tag{2.13}$$

and $\alpha_m$is interaction parameter in Cahn's solute drag model and is given by

$$\alpha_m = \frac{\beta.\mathrm{N_v}.(\mathrm{KT})^2}{\mathrm{E_b}.\mathrm{D_x}}\left(\mathrm{Sinh}\left(\frac{\mathrm{E_b}}{\mathrm{KT}}\right) - \frac{\mathrm{E_b}}{\mathrm{KT}}\right) \tag{2.14}$$

where β is constant, $\mathrm{N_v}$ is the number of atoms per unit volume, $\mathrm{E_b}$ is the solute-boundary binding energy and $\mathrm{D_x}$ is the cross-boundary diffusion coefficient.

[2.3.4.5.2]. Recrystallized volume in growth stage of recrystallization

In the case that the recrystallized volume exceeds the volume of the outer shell, nucleation sites deplete and recrystallized grains start to grow (shown earlier by red arrows in

Figure 2.7(b)). The growth of the recrystallized shell (with an inner radius equal to R(t)) continues towards the center of grain until the entire grain is consumed. The increase in recrystallized volume is then given by:

$$dV_{rex-growth} = 4\pi.R(t)^2.M.G(t).dt \tag{2.15}$$

where R(t) is the instantaneous radius of un-recrystallized region and is equal to the difference between the original radius of deformed grains and the radius of the recrystallized region:

$$R(t) = \sqrt[3]{\left[\left(\frac{4}{3}.\pi\left[\frac{D_e}{2}\right]^3\right) - V_{rex}\right] \times \frac{3}{4\pi}} \tag{2.16}$$

where V_{rex} is equal to the total volume of nucleated grains (i.e., $N(t)$ times $V_{rex-nucleation}$) in nucleation stage ($V_{rex-Nucleation} < V_{shell}$), and is equal to $V_{rex-growth}$ in the growth stage.

[2.3.4.6]. Fraction of recrystallization

Depending on the stage of recrystallization (see Fig. 2.8), the total volume of recrystallized region can be obtained by subtracting the volume of deformed grains from the volume of un-recrystallized core.

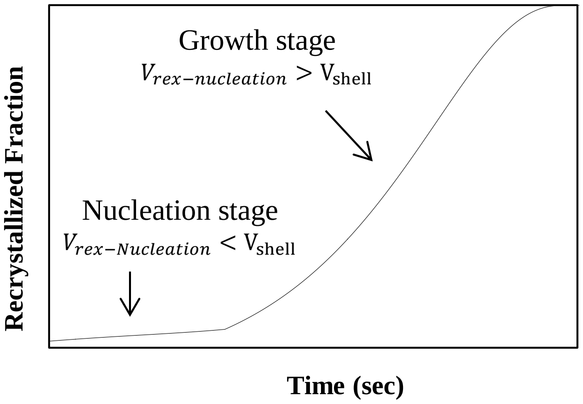

Fig. 2.8. Schematic illustration of nucleation and growth criteria during recrystallization process.

Dividing the total volume of recrystallized grains by the volume of deformed grains then gives the fraction of recrystallization. This fraction can be expressed as:

$$X = \left[\frac{\left(\frac{4}{3}.\pi\left[\frac{D_e}{2}\right]^3 - \frac{4}{3}.\pi\left[R(t)\right]^3\right)}{\frac{4}{3}.\pi\left[\frac{D_e}{2}\right]^3}\right] = 1 - \left[\frac{2.R(t)}{D_e}\right]^3 \tag{2.17}$$

[2.3.4.7]. Grain size

[2.3.4.7.1]. Partial recrystallization

An estimation of the number of nuclei and extent of recrystallization as shown above can be utilized for grain size modelling in partially and fully recrystallized materials. In partially recrystallized material, a weighted average, based on the fraction of recrystallized and un-recrystallized regions and the grain size in each region, gives the average grain size as:

$$\mathrm{D_{avg}} = 2\mathrm{R(t)}.(1-\mathrm{X}) + \mathrm{D_{rex}}.\mathrm{X} \tag{2.18}$$

where $\mathrm{D_{rex}}$ is the grain size in the recrystallized region. This term is estimated by considering that the total volume of recrystallized region per grain ($\mathrm{V_{total}}$) can be defined either as a difference between volumes of deformed grain and un-recrystallized region or the maximum number of nucleated grains times their volume ($\mathrm{N_{rex}}.\mathrm{V_{rex}}$). Equating the above two terms for $\mathrm{V_{total}}$ gives,

$$\mathrm{D_{rex}} = \sqrt[3]{2.\left[\frac{(\frac{4}{3}.\pi\,([\frac{\mathrm{De}}{2}]^3 - [\mathrm{R(t)}]^3))}{\frac{4}{3}.\pi.\mathrm{N_{rex}}}\right]} = \sqrt[3]{2.\left[\frac{([\frac{\mathrm{De}}{2}]^3 - [\mathrm{R(t)}]^3)}{\mathrm{N_{rex}}}\right]} \tag{2.19}$$

where the maximum number of nuclei in the nucleation stage, $\mathrm{N_{rex}}$, can be obtained from Eq. (2.7).

[2.3.4.7.2]. Grain growth after complete recrystallization

Once recrystallization is complete, the recrystallized grains coarsen to reduce their curvature and grain boundary surface energy. The grain size in this stage can be readily calculated from the following expression based on normal grain growth theory of Hillert [18]:

$$\mathrm{D}^2 = \mathrm{D_{avg}}^2 + 2.\alpha_{\mathrm{gr}}.\mathrm{M}.\gamma.(\Delta \mathrm{t}) \tag{2.20}$$

where D is the average grain size after complete recrystallization, $\mathrm{D_{avg}}$ is average grain size of fully recrystallized material from Eq. (2.18), α_{gr} is a constant, and $\Delta\mathrm{t}$ is the elapsed time from the start of recrystallization.

[2.3.4.8]. Stress-strain response

Based on recrystallization fraction and grain size in the growth stage, as noted above, the mechanical properties such as yield stress and plastic flow stress of PSA processed material could be predicted in the reloading stage. In the partially recrystallized material, the resulting microstructure is a mixture of recrystallized and un-recrystallized regions. Since these two regions are perfectly bonded, the following rule of mixture expression could be utilized to predict the overall mechanical properties as

$$\sigma = \mathrm{X}.\sigma_{\mathrm{rex}} + (1-\mathrm{X}).\sigma_{\mathrm{un-rex}} \tag{2.21}$$

where σ_{rex} and $\sigma_{\mathrm{un-rex}}$ are the flow stresses in the recrystallized and unrecrystallized regions.

Since a fully recrystallized material typically advances well into grain growth stage with continued annealing, the following Hall-Petch relationship can be used to model the post-annealed strength,

$$\sigma = \sigma_{\mathrm{rex}} - \mathrm{K}_{\mathrm{HP}}.\mathrm{D}^{\frac{-1}{2}} \tag{2.22}$$

where K_{HP} is the Hall-Petch coefficient and D is the average grain size (from Eq. 2.20).

[2.3.4.8.1]. Yield strength

In order to model the overall yield strength of partially recrystallized material, the flow stress of each region in Eq. 2.21 (i.e., σ_{rex} and $\sigma_{\mathrm{un-rex}}$) must be replaced by the corresponding yield strengths of each region. The yield stress of fully recrystallized region ($\sigma_{\mathrm{y\ rex}}$) is similar to that of original material during monotonic testing (without pre-straining). The yield strength of un-recrystallized region ($\sigma_{\mathrm{y}_{\mathrm{un-rex}}}$), however, is related to that of fully recrystallized material and a portion of remaining internal stress once annealing is completed. As noted earlier in Eq. 2.2, the only factor that changes during cooling process (amongst the parameters α, ρ, μ) is the shear modulus. Dividing the given value of μ at the temperature of annealing by the value at room temperature gives the portion of internal stress that contributes towards the yield stress of the annealed material. The yield strength in the un-recrystallized region could be approximated as:

$$\sigma_{\mathrm{y}_{\mathrm{un-rex}}} = \sigma_{\mathrm{y\ rex}} + \sigma_{\mathrm{D}}.\frac{\mu_{\mathrm{T}}}{\mu_{\mathrm{RT}}} \tag{2.23}$$

where μ_{T} and μ_{RT} are the shear moduli at annealing and room temperatures respectively. The temperature dependency of shear modulus for Mg alloys is given by [32]:

$$\mu_{\mathrm{T}} = 16.6\left[1 - 0.49\,\frac{(\mathrm{T}-300)}{924}\right] \tag{2.24}$$

Note that the yield strength in the growth stage could be obtained by replacing the yield strength of fully recrystallized materials in Eq. 2.22.

[2.3.4.8.2]. Flow stress in plastic region

Similar approach is employed to model the plastic flow behavior in the post-PSA reloading step by substituting the plastic flow stress of recrystallized region ($\sigma_{p_{rex}}$) and un-recrystallized region ($\sigma_{p_{un-rex}}$) in Eq. 2.21. A schematic illustration of yield drop and work hardening responses in recrystallized and un-recrystallized regions is presented in Fig. 2.9.

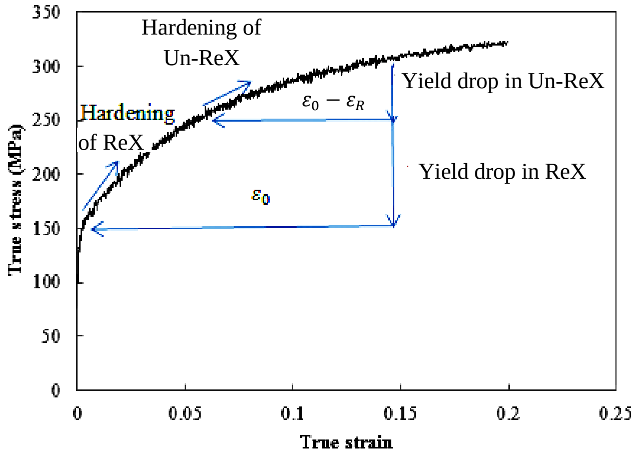

Fig. 2.9. The flow stress curve of annealed material showing the modelling approach to determine hardening and yield drop associated with recrystallized and un-recrystallized regions.

The response of the recrystallized region is similar to that of fully recrystallized material (annealed material without pre-straining) as expressed by the following power law equation:

$$\sigma_{p_{rex}} = K_H . \varepsilon^n \tag{2.25}$$

where K_H is strength coefficient, ε is the true strain and n is the hardening exponent. The stress-strain response in the un-recrystallized region, however, can be measured based on strain recovery method [33]. According to this theory, the plastic flow stress on reloading of un-recrystallized region could be considered as that of a fully recrystallized material which is pre-strained to a residual pre-strain of ε_R. The stress-strain relationship in this region can be then expressed by:

$$\sigma_{\mathrm{un-rex}} = K_H(\varepsilon_R + \varepsilon)^n \tag{2.26}$$

The residual pre-strain value is proportional to the applied pre-strain, ε_0, and can be expressed as:

$$\varepsilon_R = (1 - \Omega).\,\varepsilon_0 \tag{2.27}$$

where Ω is the fraction of yield stress in un-recrystallized region before annealing (or that of pre-strained material in Fig. 2.2(a)) and after annealing (as calculated from Eq. 2.23).

The plastic flow stress of coarsened material can be obtained by substituting values for $\sigma_{p_{rex}}$ in Eq. 2.22.

[2.3.5]. Calculation scheme

The model was implemented in Microsoft Excel (version 2010). The values of annealing temperature (T), applied pre-strain (ε_0) and the corresponding stress value, initial grain size of fully annealed material (D_0) and average number of twins per grain (n_t) from pre-straining were provided at the start of the calculation. The model utilized very small time steps at first, of the order of 1×10^{-10} s, to suitably capture the early stages of annealing. The time step was rapidly increased in size to complete the calculations over a period of a few seconds. At each step of calculation as shown in the annealing box of flowchart in Fig. 2.4, the instantaneous σ_D was first predicted from Eq. 2.3. The yield strengths from two-stage flow curves (Fig. 2.2(a)) were employed as the initial conditions for the ODE in Eq. 2.3. The corresponding values for R_g, U_a, v_d, E, V_a and K in this equation were assigned from Table 2.2 (see section 2.3.6 below). The resulting value of σ_D was then used as an input for Eq. 2.2 to calculate the instantaneous dislocation density ($\rho(t)$) during annealing. The constants in this equation (α, M_T, μ, and b) were taken from literature as given in Table 2.2. The dislocation density value was then utilized in Eq. 2.1 to calculate the drop in instantaneous stored energy (G(t)). Also, the calculated σ_D was utilized in Eqs. 2.4 and 2.5 to predict the instantaneous radius of sub-grains (r(t)). The initial size of sub-grains to solve Eq. 2.4 was set to zero. By having r(t) and $\rho(t)$, the nucleation condition (Eq. 2.6) was checked and the instantaneous and critical radius of sub-grains ($r_c(t)$) above which grains nucleate was calculated. The calculated r(t) and $r_c(t)$ were employed along with initial grain size (D_0) and twin numbers (n_t) to calculate f(t), $N_{sg}(t)$ and $F_n(t)$ through equations 2.8-

2.10. In this connection, first r(t) and r_c(t) were used to calculate $\chi_c(t)$ for f(t) and then D_0 and n_t were employed to solve for S_v. The calculation of $F_n(t)$, at this step, depended on V_{shell} which took R_i as the initial radius of the original grains and δ (thickness of the grain boundary) from Table 2.2. It also depended on $V_{rex-nucleation}$, as explained later. For the calculation of instantaneous nuclei number (N(t)), the resulting f(t), $N_{sg}(t)$ and $F_n(t)$ were put into equation 2.7. In order to solve this ODE, the initial values for f(t) and N(t) were set to zero as the boundary condition. By considering M from equation 2.12 and taking r_c(t) as the initial grain size, r(t) was re-calculated for recrystallized grains from equation 2.4. At this step, C_{Al} and C_{Zn} were set as constants for AZ31, M_{pure} and $\alpha_m$were calculated form Eqs. 2.13 and 2.14 and input parameters β, N_v, E_b and D_x were utilized from literature (see Table 2.2). The calculated r(t) then entered into Eq. 2.11 for computation of volume of recrystallized grains in the nucleation stage ($V_{rex-nucleation}$). The volume of recrystallized grains was calculated once the growth condition was fulfilled ($V_{rex-Nucleation} > V_{shell}$). For the calculation of $V_{rex-growth}$, equation 2.15 was employed in which G(t) and M were evoked from equations 2.1 and 2.12 and R(t) was calculated from equation 2.16. It is worth mentioning here that the initial value for R(t) was set equal to V_{shell}. Once the volume of recrystallization in nucleation ($V_{rex-nucleation}$) and growth ($V_{rex-growth}$) stages were computed, fraction of recrystallization (X) was obtained by means of Eq. 2.17. The selected value for volume of recrystallization was utilized at this step by comparing $V_{rex-Nucleation}$ and V_{shell}, as explained in section 2.3.4.5. At this point, one proceeded to the next box of flowchart in Fig. 2.4 for grain size calculation. The calculated X and R(t) were then used as entries in Eq. 2.18 to calculate the average grain size after partial recrystallization (D_{avg}). At this step, the grain size in recrystallized region (D_{rex}) was calculated by recalling the maximum number of nuclei (N_{rex}) from Eq. 2.7 and the radius of un-recrystallized core (R(t)) from Eq. 2.16. The final grain size (D) was calculated at this stage using equation 2.20 in which M and D_{avg}were taken from equations 2.12 and 2.18. The constants α_{gr} and γ were entered from Table 2.2 and Δt was considered as the elapsed time from the moment X became equal to unity. Once the values of X and D were obtained, the calculations on the right side of flowchart in Fig. 2.4 were carried out. Equations 2.21 and 2.22 were used to calculate the yield strength during reloading stage of PSA process. At this step of calculation, D was recalled from equation 2.20, $\sigma_{y\ rex}$was extracted from Fig. 2.2(a), K_{HP} was obtained from data fitting to experimental data of fully recrystallized material (Fig. 2.2(a)), and $\sigma_{y\ \mathrm{un-rex}}$ was calculated via equation 2.23. For calculation of $\sigma_{y\ \mathrm{un-rex}}$, equation 2.2 and 2.24 were respectively employed for σ_D and μ_T. To predict the plastic flow stress of PSA material, equations 2.21 and 2.22 along with stress-strain curve of fully recrystallized material ($\sigma_{p\ \mathrm{rex}}$) from Fig. 2.2(a) were utilized. The plastic flow stress in un-recrystallized region ($\sigma_{p\ \mathrm{un-rex}}$) was also adopted from that of fully recrystallized material but from the starting point of ε_R as calculated in equation 2.27. A small strain increment step size of 0.01 was selected in equations 2.21 and 2.22.

[2.3.6]. Model input parameters

Most of the physical quantities as input parameters in the present model were collected from previously published results on AZ31. These parameters were known with a reasonable degree of accuracy, as summarized in Table 2.2. However, some of these require explanation. Considering that PSA involves isothermal annealing, the grain-boundary energy, γ, is taken to be independent of temperature with a typical value of 0.5 J/m^2 for metals [34]. The values for activation volume (V_a) for this study were obtained by extrapolation of published data in pre-strain range of 0.1-0.3 on AZ31 in references [23, 26]. This value was then set to $24b^3$for 0.17 pre-strained material, $24.5b^3$for 0.15 pre-strained material, $26b^3$for 0.1 and $28b^3$for 0.05 pre-strained material [23]. As for the cross-diffusion coefficient, a value of 10 times the bulk diffusion coefficients of Mg was found to produce the best fit for the experimental data [26,35]. A value of 15 $\frac{\mathrm{KJ}}{\mathrm{mole}}$ (in the absence of reliable data) was used for both Al and Zn solutes in AZ31 to calculate α_m [26]. The average number of twins per grain (n_t) for pre-strained AZ31 materials was taken from a previously published work by the present authors [2]. The specific utilized values of (n_t) were 0.04, 0.18, 0.29 and 0.33 corresponding to pre-strain values of 0.05, 0.1, 0.15 and 0.17 respectively. Hollomon parameters (Eq. 2.25) were found by curve fitting true stress-strain data that are presented in Fig. 2.2(a) for fully annealed AZ31 without pre-straining.

Table. 2.2. List of constants used in modelling

Definition	Symbols and units	Value	Reference
Activation enthalpy for recovery	U_a (kJ/mole)	180	[23]
Binding energy Al	E_b (kJ/mole)	15	[35]
Binding energy Zn	E_b (kJ/mole)	15	[35]
Gas constant	R_g (J/mole.K)	8.314	constant
Bulk diffusivity	D_{bulk} Al & Zn (m^2/s)	6.1×10^{-20}	[32]
Cross-Boundary diffusion coefficient	$D_{\text{cross-boundary}}$ ($\times D_v$)	10	[35]
Grain boundary surface energy	γ (J/m^2)	0.5	[34]
Shear modulus (at room temperature)	μ (GPa)	16.6	[32]
Young modulus	E (GPa)	40.2	From this work
Boltzmann's constant	k (J/atom)	1.38×10^{-23}	Constant
Taylor factor	M_{Taylor}	4.1	[32]
Taylor constant	α	0.23	[32]
Constant	α_{gr}	0.4	[18]
Burgers vector	b (nm)	32.1	[36]
Debye frequency	$v_d(s^{-1})$	8.00×10^{12}	[36]
Sub-grain factor	$\mathrm{k_{ad}}$	2.27	[23]
Boundary shell thickness	δ (nm)	300	[23,24]
Yield stress of fully annealed	σ_{annealed} (MPa)	140	From this work
Initial value for σ_D	σ_{D0} (MPa)	145	From this work
Hall-Petch constant	K_{HP}	230	[37]
Hollomon strength index	K_H	481	From this work
Strain hardening exponent	n	0.173	From this work
Number of atoms per unit volume	N_v (m^{-3})	4.27×10^{28}	constant
Constant	β	10×10^{-9}	[23]

[2.4]. Model predictions versus experimental results

[2.4.1]. Prediction of recrystallization fraction and grain size

The predicted recrystallization fractions versus annealing time curves at annealing temperatures of 200˚C, 300˚C, 400˚C and various experimental pre-strain values are shown by solid lines in Fig. 2.10 along with the corresponding experimental values with symbols. The predictions are generally in good agreement with the experimental values. The results reveal an increase in the recrystallized fraction with increased pre-strain and annealing temperature in a manner similar to the experiments.

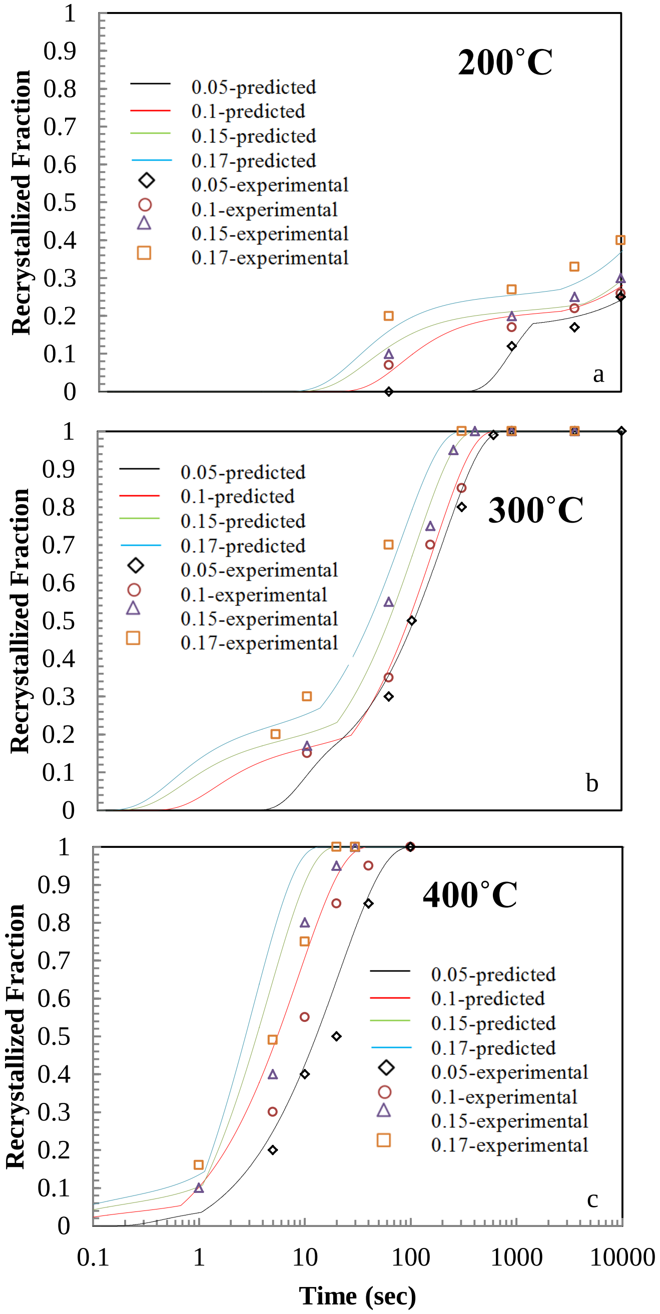

Fig. 2.10. Predicted versus experimental recrystallization fraction for PSA processed annealed at (a) 200˚C, (b) 300˚C, and (c) 400˚C.

As with the recrystallization rate, the initiation of recrystallization occurs at smaller times as the temperature or pre-strain increases. The ultimate fraction of recrystallization is also highly affected by temperature of annealing so that 200˚C results in partial recrystallization whereas 300˚C and 400˚C lead to complete recrystallization for the same amount of pre-strain. Results indicate that the partial and complete fractions of recrystallization are successfully predicted by the model. Also, the incubation and completion time of recrystallization for the samples are captured rather closely (with maximum deviation of 5%) at 200˚C and 300˚C by the model. A small disagreement can be noted for the samples at 400˚C where most of the recrystallization phenomena occur rapidly at small times of annealing. The experimental measurements, however, show longer times for these phenomena, i.e., completion of the recrystallization is attributed to the fact that model specimens take shorter times compared to the experiments to reach to the given temperatures of annealing. Some inaccuracy in experimentally determining the recrystallized fraction could perhaps arise from counting of the non-recrystallized grains in the microstructure. The predicted values of grain size by PSA process are shown in Fig. 2.11.

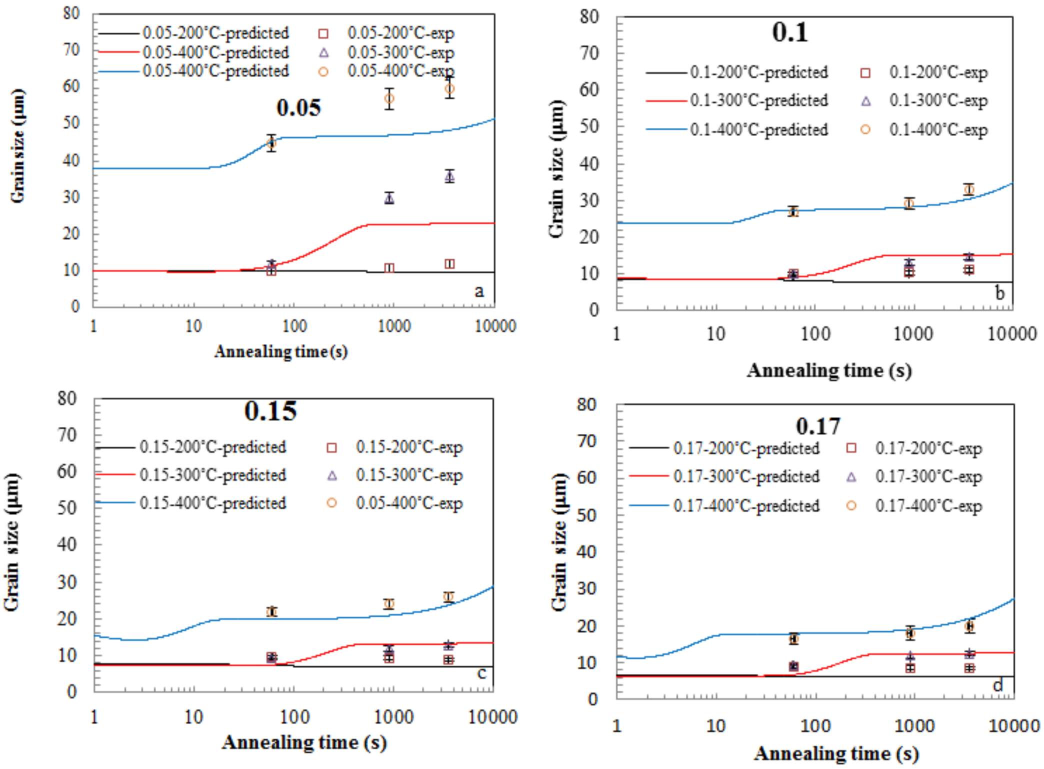

Fig. 2.11. Predicted versus experimental grain size as a function of time for PSA processed materials corresponding to the pre-strain values of (a) 0.05, (b) 0.1, (c) 0.15 and (d) 0.17.

The modeled grain size curves largely capture the trend with respect to the experimental average grain size changes versus annealing time, temperature and pre-strains. As expected, a larger final grain size could be seen at smaller pre-strains and higher temperatures. Model curves, however, exhibit somewhat poor predictions at a low pre-strain of 0.05 and at high annealing temperatures (see Figure 2.11(a)). For the rest of cases where experimental results show slight grain refinement (for example, all pre-strains at annealing temperature of 200˚C) and normal grain growth (pre-strains greater than 0.1 and annealing temperatures greater than 200˚C), the grain size is predicted with an accepted range of error.

[2.4.2]. Post-PSA yield strength and flow stress prediction

The yield strength versus annealing times curves of post-PSA materials in the reloading stage are shown in Fig. 2.12 along with the corresponding experimental data, for a range of annealing temperatures and pre-strains.

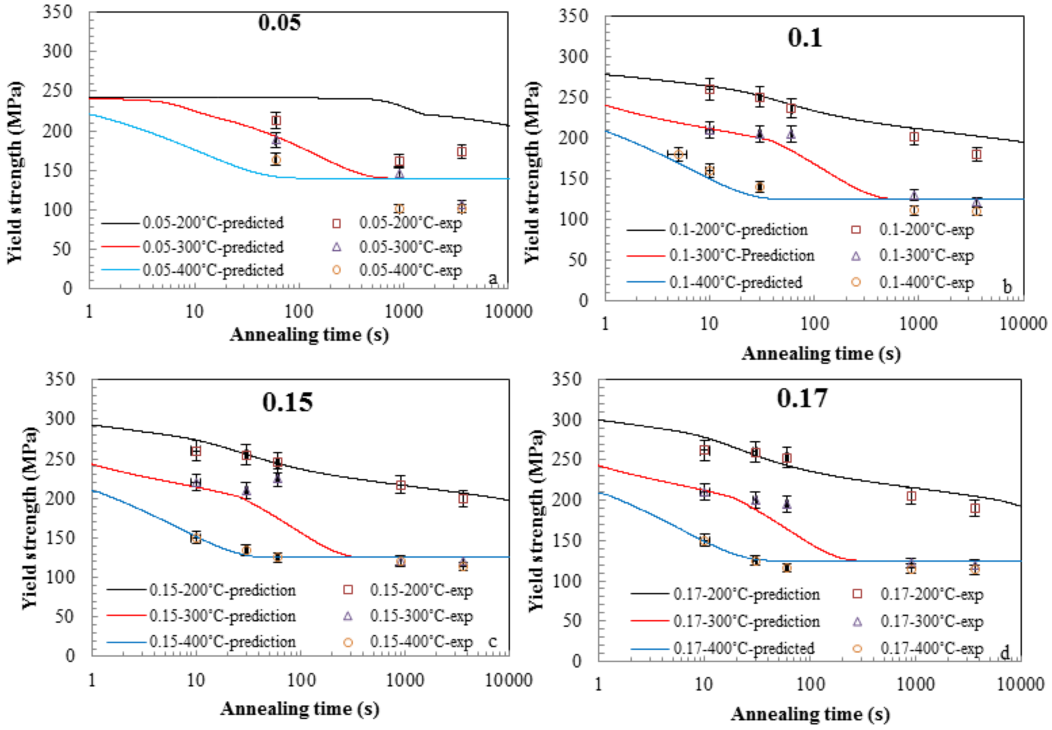

Fig. 2.12. Plots showing predicted and experimental yield strength versus time for PSA processed materials corresponding to pre-strain values of (a) 0.05, (b) 0.1, (c) 0.15 and (d) 0.17.

Model predictions are generally in good agreement with the experimental values. The magnitude of yield drop also is realistically predicted for many of the PSA conditions where both the experimental and predicted values show a rapid drop in yield stress at higher annealing temperatures. However, a significant deviation between model curve and experimental data can be noted for a pre-strain of 0.05 where the model predicts softening until the yield stress attains values similar to that of the fully annealed material whereas the experimental measurements show lower values. This will be discussed later in Section 2.5.2.

Figure 2.13 shows predictions of stress-strain curves of post-PSA material (reloading stage) and corresponding experimental plots for a small set of PSA conditions.

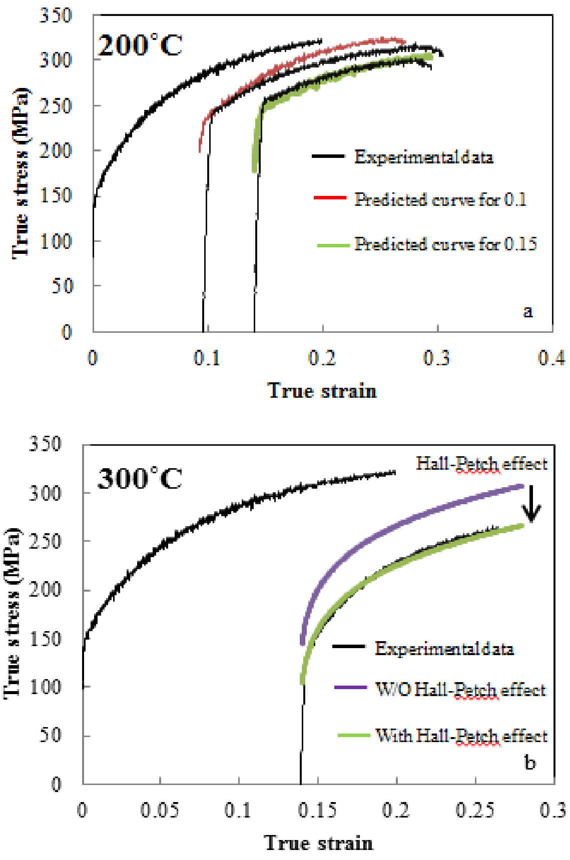

Fig. 2.13. Plots showing predicted and experimental stress-strain curve of PSA processed materials for, (a) 0.1 and 0.15 pre-strained materials and annealed at 200˚C-60s and (b) 0.15 pre-strained material and annealed at 300˚C-60s.

The predicted curves are generally quite close to the experimental ones suggesting that both the hardening rate and UTS values are well predicted for the chosen PSA conditions. Some deviations were observed near yield point for the un-recrystallized material (for example, 0.1-200˚C-60s case). Also, the predicted curves for the partially recrystallized microstructure deviate slightly from experimental values at higher strains (0.15-200˚C-60s). For the coarse-grained material (0.15-300˚C-60s), however, model accurately estimates the experimental curves after considering the Hall-Petch effect. This figure also shows that the elongations are predicted with higher accuracy for un-recrystallized and partially recrystallized microstructures than for grains subjected to grain growth. Further study is required to redefine the Hall-Petch constants based on strain and grain size relationship to improve the predictions.

[2.5]. Discussion

[2.5.1]. Annealing related microstructure changes

All the pre-strain values in this study were large enough to activate recrystallization at the chosen annealing temperatures. The pre-strain value of 0.05 resulted in only a small fraction of recrystallization at 200˚C, but resulted in complete recrystallization at 300˚C and 400˚C due to the thermally activated nature of recrystallization process. This led to both normal and abnormal grain coarsening after complete recrystallization. The abnormal grain structure (seen at lower pre-strains and high annealing temperatures as shown in Fig. 2.3) can arise from surface-energy considerations [38] and normal grain coarsening (observed at other pre-strain values) could be due to diffusion controlled mechanisms across the grain boundaries [11]. Since larger grains possess lesser grain boundary surface area per unit of volume, they lose fewer atoms and grow at the expense of smaller grains. The abnormal grain growth and dependency of recrystallized grain size on the amount of pre-strain values could be attributed to higher sensitivity of the nucleation rate (than growth rate) to the pre-strain values [11]. Therefore, a higher pre-strain value would provide more nuclei per unit volume leading to a smaller final grain size. Comparison of modelling predictions and experimental results does indicate failure of the model in predicting accurate grain size in the case of abnormal grain growth. This could be attributed to the current modeling approach which assumes a uniform distribution of stored energy throughout the microstructure and ties it with normal grain growth theory. Hence, this assumption results in accurate predictions for highly pre-strained materials (above 0.1 in Figures 2.11 and 2.12) and leads to inaccurate predictions for 0.05 pre-strained materials where abnormal grain growth occurs due to heterogeneity of deformation (see Figures 2.11 and 2.3). To account for this, one should develop a two-site model which assumes highly deformed region having high stored energy with smaller effective grain size in one site and less deformed region possessing low stored energy with larger effective grain size in other site. This would result in local nucleation rate at different spots and better prediction of grain size for abnormally grown grains materials.

A plateau in the time evolution of the recrystallization fraction, shown in Fig. 2.11, is indicative of incomplete recrystallization at 200˚C in agreement with observed experimental results. This could be explained by the competition between recovery and recrystallization that is captured by the model. According to the presented results in Fig. 2.11, a combination of low annealing temperature and small pre-strain values would result in a slower recrystallization so that recovery, requiring lower activation energy, could proceed to reduce the driving force (G(t)). On the other hand, the stored energy per unit volume of un-recrystallized material is steadily reduced due to competition which further retards recrystallization [11, 39]. The retardation in recrystallization appears to be influenced more by the annealing temperature and less by pre-strain as the recrystallization remains incomplete at 200˚C whereas it is completed at higher temperatures even when the pre-strain is low (see Figure 2.11). It is worth mentioning that the observed incomplete recrystallization in AZ31 is in agreement with the existing published results on the rolled and annealed material in literature [23,26].

The current modelling assumption regarding modification of grain size effect for AZ31 due to small twin formation in uniaxial tensile pre-straining appears to be reasonable. However, it should be noted that twin formation may occur at different levels through other modes of deformation such as plane strain bending or uniaxial compression. This then becomes challenging assumption noting that only certain types of twins such as double twins could effectively provide potential recrystallization sites [40]. Hence, the twin number should probably be counted by considering the twin type and thickness in the calculation.

[2.5.2]. Post-PSA mechanical response

Model predictions shown earlier in Figs. 2.12 and 2.13 indicate a drop in reloaded yield strength and plastic flow curves. This could be interpreted in terms of different softening contributions from recovery, recrystallization and grain growth that occur during annealing. The shape of the reloaded flow curve and the flow stress, in other words, is a consequence of evolving microstructure from the above softening mechanisms. A large drop in flow stress (for example, in Fig. 2.12 for specimens annealed at 200˚C and 300˚C), could be attributed to the different strains for onset of each mechanism and likely overlaps in these mechanisms. In the case of large fraction of recovery and a smaller fraction of recrystallization which is expected to occur during PSA at 200˚C, for example, reloading results in a larger yield drop but a lesser drop in UTS (compare curve 1 with other curves in Fig. 2.2(b)). On the other hand, at longer annealing times and at higher annealing temperatures, the fraction of recrystallization increases in the PSA microstructure which leads to a larger drop in UTS and increased ductility improvement by providing strain free grains (as shown in Fig. 2.2(c)). The recrystallized grains are typically smaller in size than the original grains providing uniformity of deformation and delay in the onset of localized necking [41]. In contrast, grain growth which happens after complete recrystallization (and mostly at 300˚C and 400˚C) results in increased grain size distribution (even abnormal grain growth), deformation inhomogeneity in the microstructure, and earlier onset of localized necking and fracture. The latter leads to less of an improvement in tensile ductility as well as reduction in UTS (see Figure 2.14 where microstructure exhibits fracture from abnormal grain growth). Since the abnormal grain growth and its effect on strain localization are not captured by the model, the predictions of strength and ductility not as inaccurate for PSA conditions which give rise to significant grain growth such as low pre-strains and large annealing temperatures and times.

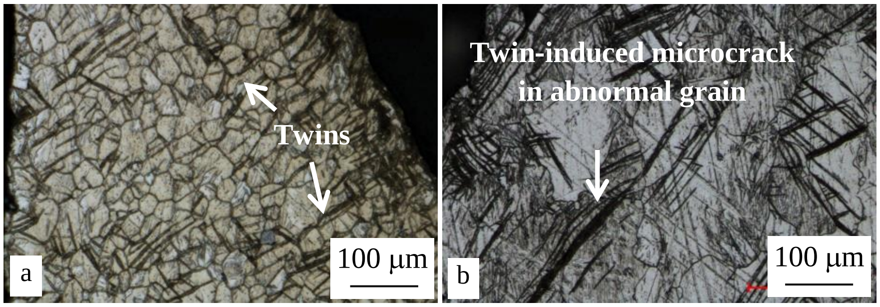

Fig. 2.14. Deformed microstructure of tensile test specimens from LT plane in the vicinity of fracture, (a) fully annealed material under monotonic loading to fracture, and (b) PSA material pre-strained to strain of 0.05 and annealed at 400°C-60 min.

[2.6]. Conclusions

PSA process was shown as an effective process to enhance the cumulative uniaxial tensile ductility of AZ31 at room temperature. By employing different pre-strain value and annealing degree, most of the stress-strain responses on reloading stage of PSA process were shown to be dependent on the post-PSA microstructure state. Therefore, a simple microstructure-based model was developed to predict the recrystallization behavior in pre-forming (in uniaxial tension) and isothermal annealing and to estimate the post-PSA deformation behavior of AZ31 sheet. The model utilizes easily quantifiable parameters of the PSA process including applied pre-strain, annealing temperature, initial grain size and twin number. An effective grain size based on number of twins is utilized in the model to capture the deformation behavior of single phase HCP AZ31 Mg alloy. In spite of its simplicity, the strength of the model is in capturing the concurrent effect of recovery on both nucleation and growth of recrystallization and to account for non-constant rates. Unlike the common JMAK model, therefore, the values of nucleation number and growth rate would be calculated by the model and there would be no need to measure them experimentally and enter them separately. Based on model predictions, it was shown that the PSA microstructure could be reasonably assumed as a composite of un-recrystallized and recrystallized microstructures. Also, the rule of mixture is shown to successfully predict yield strength and plastic flow stress during post-PSA reloading. Furthermore, Hall-Petch effect is shown to account for the strength softening from grain coarsening that occurs during the PSA process. Comparisons between experiment and model predictions show good agreement with a maximum deviation of 5% over a wide range of pre-strain values, annealing temperature and initial effective grain size. In summary, the model has been able to successfully predict, (i) complete and incomplete fraction of recrystallization and recovery for PSA material, (ii) average grain size after partial recrystallization and grain coarsening of AZ31, (iii) yield drop after recovery, partial recrystallization and grain coarsening, and (iv) plastic flow stress during re-loading of PSA material.

The current model also has some shortcomings. It was unable to predict experimentally observed significant grain growth and strength softening at low pre-strains and high annealing temperatures. This likely stems from the assumption of uniform strain distribution in the microstructure during pre-straining. This limitation could be overcome in the future by coupling the present model framework to an abnormal grain growth model [18].

References

1. P. E. Krajewski, Method for production of stamped sheet metal panels, US Patent: 7260972B2 (2007).
2. M. Habibnejad-korayem, M. K. Jain, R. K. Mishra, Mater. Sci. Eng. A. 619 (2014) 370–377.
3. M. Habibnejad-korayem, M. K. Jain, R. K. Mishra, Mater. Sci. Eng. A. 619 (2014) 378-383.
4. T. M. Lee, S. E. Hartfield-Wünsch, S. Xu, SAE Paper No. 2006-01-0987.
5. J. J. Li, S. Kim, T. M. Lee, P. E. Krajewski, H. Wang, S. J. Hu, Mater. Sci. Eng. A 582 (2011) 3905-3914.
6. H. Zhang, G. Huang, L. Wang, J. Li, Scripta Mater. 67(2012) 495–499.
7. M. Verdier, Y. J. M. Brechet, P. Guyot, Acta Mater., 47(1998) 127–134.
8. H.S. Zurob, Y. J. M. Brechet, J. Dunlop, Acta Mater., 54 (2006) 3983–3990.
9. J.W.C. Dunlop, Y. J. M. Brechet, L. Legras , H.S. Zurob, J. Nucl. Mater. 366 (2007) 178–186.
10. M. D. Kashif Rehman, H. S. Zurob, Met. Trans. 44A (2013) 1862-1871.
11. F. J. Humphreys, M. Hatherly, Recrystallization and Related Annealing Phenomena, 2nd ed., Pergamon Press, Oxford, 2004.
12. W.A. Anderson, R.F. Mehl, Trans. Am. Inst. Mining Met. Eng., Inst. Metals Div., Tech. Pub. 161 (1945) 140.
13. E. Lauridsen, H. Poulsen, S. Nielsen, D. Juul Jensen, Acta Mater. 51 (2003) 4423.
14. F. Humphreys, in: B. Bacroix, J. Driver, R. Le Gall, C. Maurice, R. Penelle, H. Re´gle´(Eds.), Recrystallisation and Grain Growth, vol. 1, Trans Tech., Annecy, 2004, p. 629.
15. J. W. Cahn, Acta Metall., 4 (1956) 449.
16. T. Furu, K. Marthinsen, E. Nes, Mater. Sci. Tech., 6 (1990) 1093.
17. R. Sandstrom, Z. Metallkd., 71(1980) 681.
18. M. Hillert, Acta Metall Mater, 13 (1965) 3, 227-238.
19. H.S. Zurob, C.R. Hutchinson, Y. Brechet, G. Purdy, Acta Mater., 50 (2002) 3075–3092.
20. L. Wu, A. Jain, D. Brown, G. Stoica, S. Agnew, B. Clausen, D. Fielden, P. Liaw, Acta Mater., 56 (2008) 688-695.
21. F. J. Humphreys, Acta. Mater., 45 (1997) 4231-4240.
22. A. Levinson, R. K. Mishra, R. D. Doherty, S. R. Kalidindi, Acta Mater., 61 (2013) 5966–5978.
23. P. Okrutny, Modelling of recovery and recrystallization in Mg alloys, Master thesis, McMaster University, 2010.
24. S. Liang, Deformation and its effect on recrystallization in Mg alloy AZ31, Master thesis, McMaster University, 2012.
25. J. Friedel, Dislocations, Pergamon, Oxford, 1964.
26. P. Okrutny, S. Liang, L. Meng, H.S. Zurob, in Magnesium Technology 2014 (eds M. Alderman, M. V. Manuel, N. Hort and N. R. Neelameggham), John Wiley & Sons, Inc., Hoboken, NJ, USA. doi: 10.1002/9781118888179.ch31
27. R. Abbaschian, L. Abbaschian, R. Reed-Hill, Physical Metallurgy Principles, fourth ed, Cengage Learning, Stamford, CT (2009).
28. J.E. Bailey, P.B. Hirsch, Proc. R. Soc. Lond. A 267 (1962) 11.
29. M.E. Ashby, Phil. Mag. 21 (1970) 399.

30. J.W. Cahn, Acta Metall., 10 (1962), 789–98
31. A. Lucke, K. Detert, Acta Metall. 5(1957) 628-637.
32. H. J. Frost, M. F. Ashby, Deformation-mechanism maps, Oxford, Pergamon Press, 1982.
33. A. Yanagida, J. Yanagimoto, Mater. Sci. Eng. A 487 (2008) 510–517.
34. J. W. Martin, R. D. Doherty, B. Cantor, Stability of microstructure in metallic systems, 2nd ed. Cambridge: Cambridge University Press, 1997.
35. S. K. Das, Y. M. Kim, T. K. Ha, R. Gauvin, I. H. Jung, Mater. Sci. Forum, 765 (2013) 516-250.
36. M. M. Avedesian, Hugh Baker, ASM Specialty Handbook: Magnesium and Magnesium Alloys, ASM International, 1999.
37. J.A. del Valle, F. Carreno, O.A. Ruano, Acta Mater. 54 (2006) 4247–4259.
38. D. Askeland, P. Fulay, The Science & Engineering of Materials, fifth ed, Cengage Learning, 2005, 854 pp.
39. J. Friedel, Dislocations, International Series of Monographs on Solid State Physics, 1st English ed, Pergamon Press, Oxford, distributed by Addison-Wesley Pub. Co., Reading, 1964, xxi, 491 pp.
40. É. Martin , R. K. Mishra, J. J. Jonas, Phil. Mag. 91 (2011) 3613–3626.
41. G. Dieter, Mechanical Metallurgy, McGraw-Hill, New York, 1967.

Chapter 3

Large deformation of Magnesium sheet at room temperature by preform annealing part I: "uniaxial tension"

The study reported in this chapter was mostly conducted by this doctoral candidate (Mahdi Habibnejad-korayem) with continuous supervision, over a period of 4 .5 years, by his supervisor, Dr. Jain, and occasional technical advice from Dr. Mishra of General Motors (GM), the industrial sponsor of the project. Some experiments related to texture measurements were assisted by Mr. Kubric of GM as well. The chapter was prepared by this candidate with many discussions of its structure, focus, content, conclusions, language, and writing style with Dr. Jain. This paper is published in Materials Science & Engineering A619 (2014) 370–377.

Large deformation of Magnesium Sheet at Room Temperature by Preform Annealing

Part I: "Uniaxial tension"

Mahdi Habibnejad-korayem [a], **Mukesh K. Jain** [a,1], **Raja. K. Mishra** [b]

a McMaster University, Department of Mechanical Engineering, Hamilton, ON, Canada L8S4L8
b General Motors Research and Development Center, Warren, MI 48090, USA

Abstract

Magnesium alloys do not generally show large formability at room temperature. This paper is part I of a study to utilize multi-step uniaxial stretching and annealing (MUSA) method to deform AZ31 magnesium alloy to large strains at room temperature. Mechanical properties of MUSA materials have been correlated to microstructural observations. Microstructure parameters such as grain size, twin fraction and textural changes arising from the different variants of MUSA process and their effect on work hardening behavior and cumulated room temperature elongation of AZ31 sheet are studied. Depending on the annealing conditions and pre-strains in different steps of the MUSA process, grain refinement or grain coarsening as well texture spreading was observed. The results indicate that a MUSA process can yield equivalent elongations in AZ31 sheet at room temperature to those attained at higher temperatures.

Keywords: magnesium sheet; uniaxial tension; annealing; texture; twining, pre-strain

[3.1]. Introduction

There has been considerable interest in the use of Mg sheet for automotive applications due to its lighter weight resulting in increased fuel economy and lesser environmental footprint. The adaptation of Mg alloys in automotive body applications, however, have been limited by

---

[1] Corresponding author

their poor formability at room temperature due to its hexagonal close-packed (hcp) structure and limited slip systems. There is evidence that weakening and spreading the texture could improve the ductility of AZ31 at room temperature [1]. Refining the grain size also enhances the ductility by easing dislocation glide and transition in fracture mode [2]. Grain coarsening has been also reported effective in ductility improvement by facilitating the formation of tension twins [3]. The microstructural and textural modification may improve Mg performance during crash, but not enough for attaining room temperature formability levels similar to other conventional automotive aluminum alloys and steel. Therefore, Mg parts continue to be formed at elevated temperature where non-basal slip systems are activated. However, the process costs and part quality still remain issues at high temperature. Therefore, for improving the formability of magnesium sheet, a promising alternative option could be multi-step forming at room temperature by pre-forming the material at room temperature and intermediate annealing it to remove the cold work. Repeating this for several times during the process could yield the desired forming level and the process can be finished by forming to the final shape. This has been demonstrated as a feasible process for AA5182 aluminum alloy under different strain paths, pre-strain levels and annealing conditions [4]. It has also been used to modify the microstructure of AZ31 and enhance its stretch formability [5]. However, no effort to the author's knowledge has been made to deform Mg sheet to large strains by a multi-step forming process. The present paper aims to fill this gap by focusing on formability improvement by multi-step uniaxial stretching and annealing (MUSA). The topic is further explored in a companion paper by studying the feasibility of multi-step bending and annealing (MBA) to improve the cumulative bendability of AZ31 magnesium sheet. These two papers also try to build an understanding of the governing mechanisms and limitations of the more general process of multi-step forming and annealing (MFA).

[3.2]. Experimental procedure

AZ31 magnesium sheet of 1.5 mm thickness in the H24 temper condition was annealed at 400°C for 2 hours and machined along the rolling direction (RD) to 10 mm wide and 100 mm long tensile specimens to obtain true stress-true strain curves at an initial strain rate of $0.01\,s^{-1}$. The samples were deformed by MUSA, as schematically illustrated in Fig. 3.1.

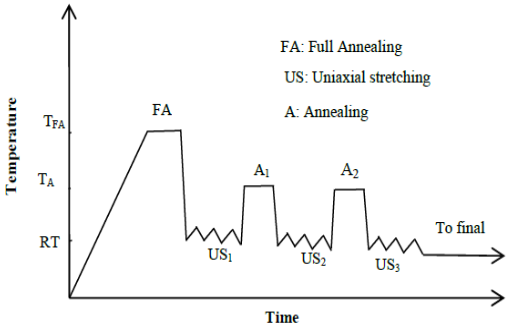

Fig. 3.1. A Schematic illustration of MUSA process.

The first sample was pulled to fracture. The second sample was pulled to 85-90% of the first elongation to fracture and followed by 3 different annealing conditions; (i) 200˚C for 1 min (MUSA-I), (ii) 200˚C for 60 min (MUSA-II) and (iii) 400˚C for 1 min (MUSA-III). The samples were then pulled to fracture at room temperature. The pre-straining and annealing steps for each of the above pre-straining and annealing conditions were repeated several times while subjecting the sample to 85-90% of the previous elongation to fracture to assess the cumulated strain (formability). High temperature tensile tests were also conducted at the above temperatures of annealing, 200˚C and 400˚C as well as at room temperature. The MUSA parameters, pre-straining and annealing conditions, were chosen from a broader study which was reported separately in chapter 2. The sequence of events during deformation was also studied by uniaxial test using a manual miniature test jig and an optical microscope. Specimens for the optical microscopy study were prepared by sectioning, polishing and etching. The polishing was done progressively by 9 μm, 3 μm, and 1 μm diamond solutions, followed by 50 nm colloidal silica slurry. The polished samples were etched with picric-acetic acid solution (1 ml acetic acid, 1ml water, 420 mg picric acid and 7 ml ethanol) for 3 seconds to reveal the grain structure. The macro- and micro-texture were studied by X-ray diffraction (XRD) and electron backscatter diffraction (EBSD) respectively. The samples for the EBSB-based texture studies were prepared by polishing as noted earlier and a quick final etching step (5–10 s) with a solution of 60% ethanol, 20% water, 15% acetic acid and 5% nitric acid. These experiments were conducted using a LEO VP SEM equipped with TSL data acquisition software at an acceleration voltage of 20 keV, with a working distance of 18 mm and a tilt angle of 70˚.

The true stress-true strain data from the various steps of pre-stretching for each of the three MUSA processes were fitted to Hollomon equation ($\sigma = K\varepsilon^n$) and the n-value at each step was obtained as a measure of changes in the work hardening behavior from step to step. The twin fraction was also quantified in a similar manner from the optical micrographs at different steps, as a function of engineering strain, where optical micrographs at a magnification of 100X and a point counting technique based on ASTM E562-02 standard was used [6]. The error in these optical measurements was estimated to be ±10 % error primarily arising from uncertainty in the recognition of matrix and twin boundaries in some cases. The compressive twins were also rather difficult to detect due to their narrow widths.

Fractured tensile specimens were also mounted along the LT plane for the three MUSA processes to observe with an optical microscope their necking and fracture profiles to investigate the nature of the final failure.

Vickers micro-hardness on 0.17 pre-strained materials was measured using 100 gf indenting load for a 15 second dwell time after annealing. The annealing was done at 200˚C and 400˚C for the annealing times of 5s, 15s, 30s, 60s, 90s, 300s, 600s, 900s, and 1200s. The tests were repeated three times and the average values were calculated.

[3.3]. Results

The uniaxial tensile properties of AZ31 from MUSA process and constant temperature continuous tensile tests are given in Fig. 3.2(a-d). In Fig. 3.2(a-c), the first deformation step consisted of a uniform region of work hardening. The uniformity of flow behavior during the subsequent steps, however, was observed to vary with the amount of pre-strain and degree of subsequent annealing. For MUSA-I process (Fig. 3.2(a)), the stress level upon reloading of the specimen rapidly reached that of the specimen at the end of the previous deformation step. For MUSA-II process (Fig. 3.2(b)), however, the stress in the pre-strained steps increased more slowly compared to MUSA-I. This was especially evident for MUSA-III (Figure 3.2(c)) where not only stress in the pre-strain step rose even more slowly but the saturation stress values were also reduced as the pre-strain steps were added. Lastly, Figure 3.2(d) for continuous tensile tests to fracture at three constant temperatures, with 2 different crosshead speeds at 400˚C are typical of magnesium sheet materials. Significant work hardening to saturation was observed at room temperature whereas at higher temperatures a quick rise to peak stress and an extended period of strain softening was observed.

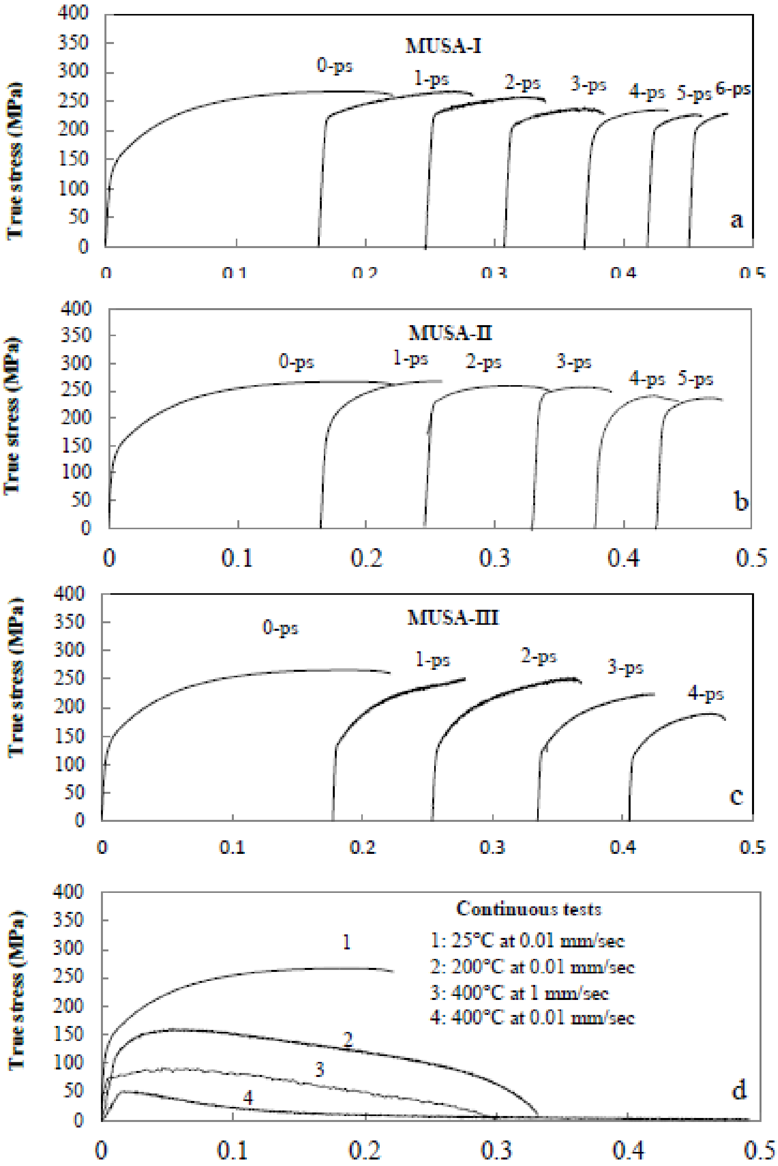

Fig. 3.2. Stress-strain curves of AZ31 deformed by (a) MUSA-I, (b) MUSA-II, (c) MUSA-III and (d) continuous tests to fracture.

Fracture profiles of failed tensile specimens at the end of three MUSA process are shown in Figure 3.3 where 3 optical micrographs for each MUSA process correspond to 4 different steps, as per Figure 3.1. The specimen in the first step of MUSA-I exhibited a slant fracture without any visible necking. The mode of fracture, however, gradually changed to more ductile and visual necking started to appear prior to fracture after the third step. During MUSA-II, the onset of visible necking was observed earlier in the second step. In contrast to MUSA-I and II, the visible necking was observed from the very first step in MUSA-III.

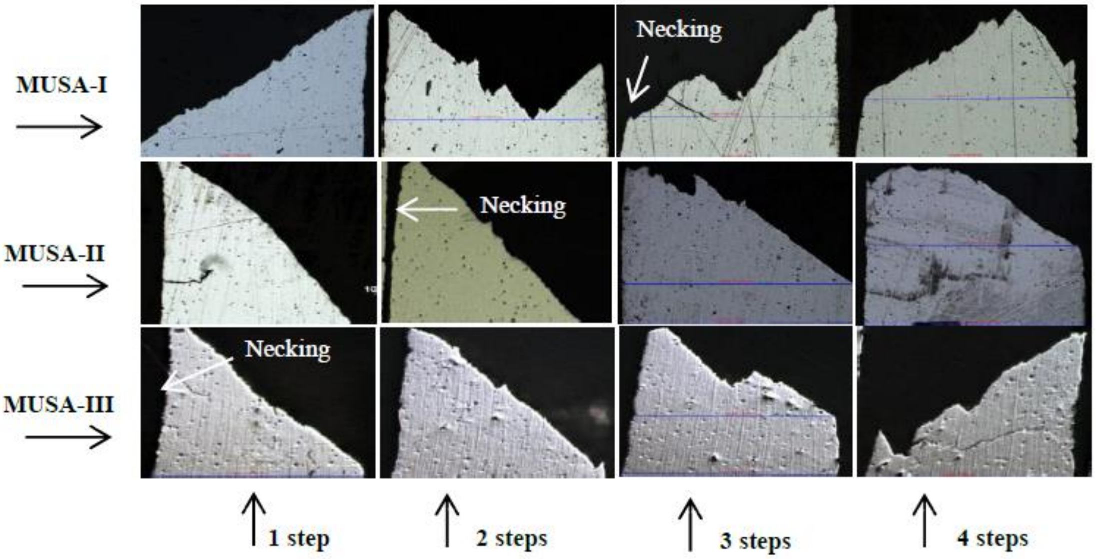

Fig. 3.3. LT plane observation of the gage length area for MUSA-I, II and III processes.

The changes in the yield stress, ultimate tensile strength, cumulative elongation and n-value as a function of MUSA step number are shown in Figure 3.4(a-d) respectively. For MUSA-I specimens, the yield strength after pre-strain steps was significantly higher for the first three steps compared to the initial yield strengths of the fully annealed specimen (Figure 3.4(a)) but showed subsequent drop with the number of MUSA steps. The ultimate tensile strength continued to drop with MUSA steps but fell well below the initial annealed value (Figure 3.4(b)).

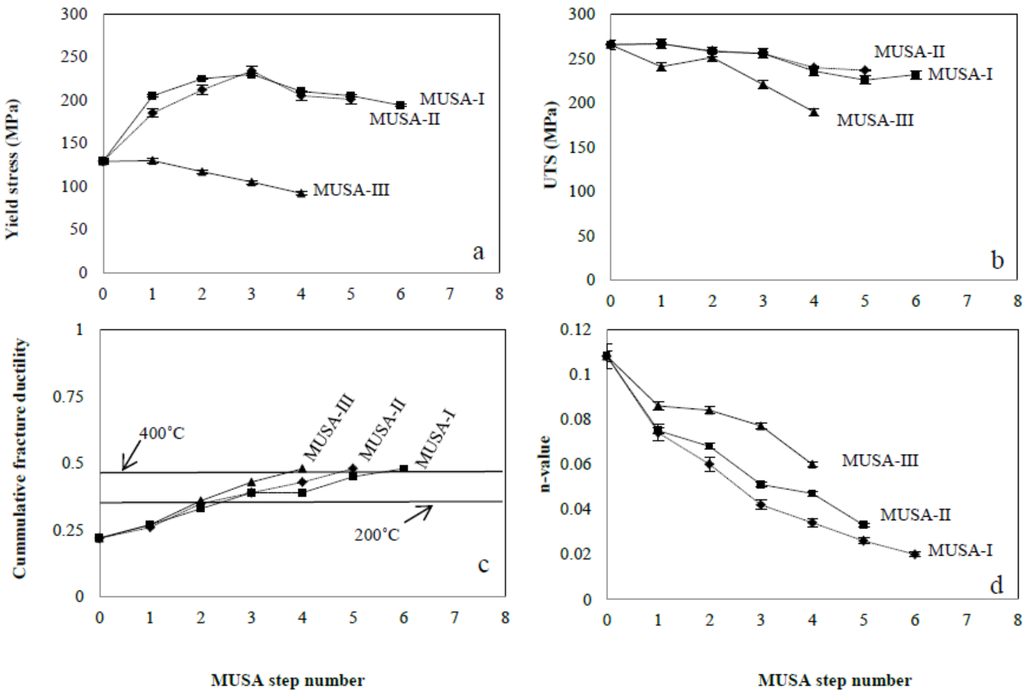

Fig. 3.4. Changes in material properties as a function of MUSA steps.

A similar trend in yield strength and ultimate strength change with MUSA step was observed for MUSA-II. The final yield strengths for both MUSA-I and II remained quite similar. For MUSA-III, both yield and tensile strengths dropped rather rapidly from their initial values in the first 4 MUSA steps and attained values even below those at room temperature in the fully annealed condition. MUSA processes led to a cumulative strain at fracture of 0.35 and 0.48, values that could be achieved only at 200°C and $400^{\circ}C$ in continuous tensile tests (Figure 3.4(c)). The approach followed was to attain similar cumulative strain values in MUSA at room temperature. The benchmark cumulative strain value of 0.35 was achieved in three steps of MUSA-I and two steps of MUSA-II and III whereas the 0.48 was achieved at 6, 5 and 4 steps of MUSA-I, II and III, respectively. A plot of n-values as function of MUSA step (Figure 3.4(d)) revealed a progressive loss of the work hardening capacity of the material with number of MUSA steps. The lower temperature at shorter anneal time (MUSA-I) showed a rather steep drop in the n-value while higher temperature at shorter time (MUSA-III) exhibited better retention of work hardening capacity of the material. The response of MUSA-II was observed to lie between these 2 cases. This would be further discussed in the next section.

The trend with respect to grain size change after annealing as a function of MUSA steps for the three MUSA process is shown in Figure 3.5.

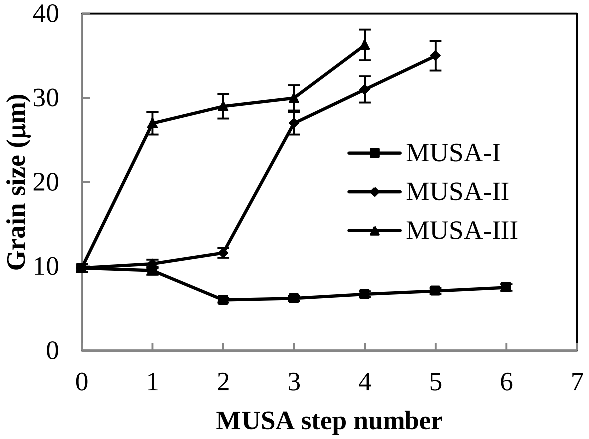

Fig. 3.5. Changes in grain size as a function of MUSA step.

As expected, the grain size increased with an increase in the annealing temperature, for the same annealing time (MUSA-I and III), and with an increase in time, for the same annealing temperature (MUSA-I and II). It is to be noted that grain refinement after annealing was observed for all steps of MUSA-I with final grain size staying below the initial grain size of 10 μm. While some scatter in the data is clearly observed, the kinetics of grain growth for MUSA-II and III was sigmoidal in shape and appeared to show 3 distinct stages. Typical optical micrographs revealing the grain structure towards the end steps for each of the 3 MUSA processes are shown in Figure 3.6 where aspects of grain refinement for MUSA-I and grain growth for MUSA-II and III can be noted.

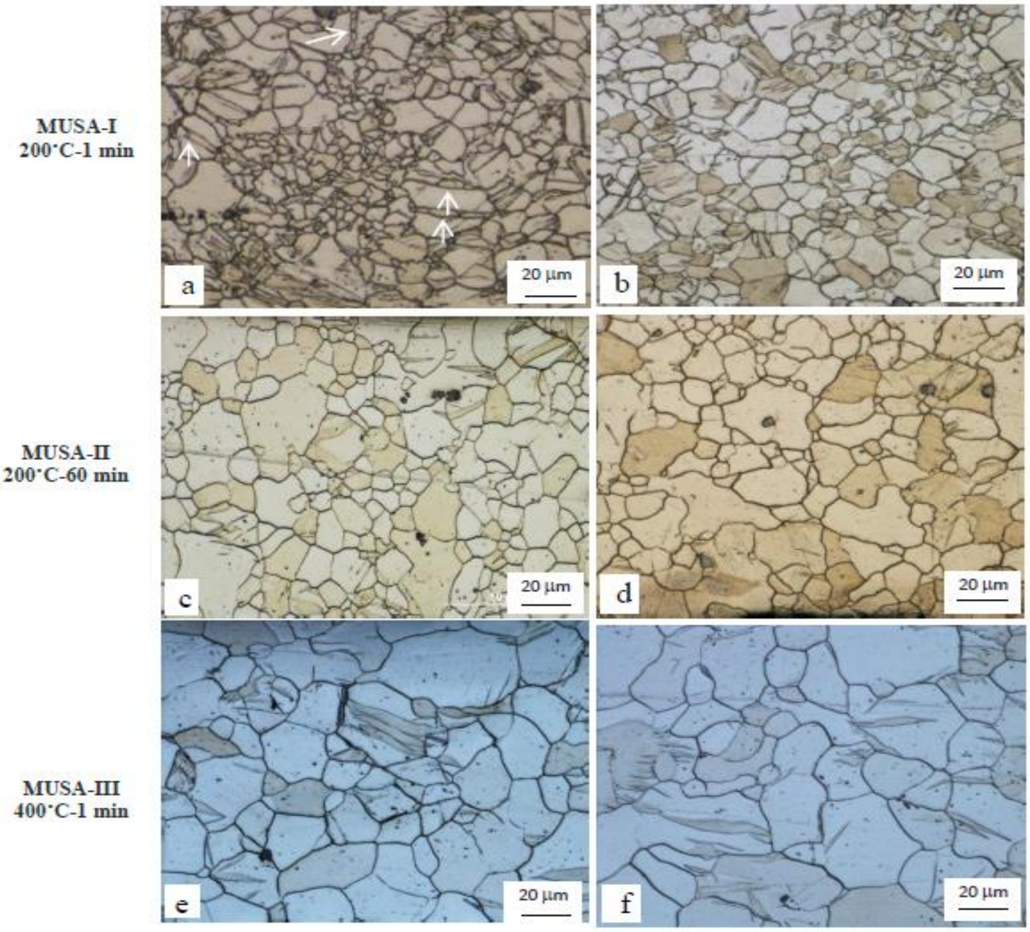

Fig. 3.6. Optical micrographs showing the microstructure of AZ31 deformed by (a) MUSA-I after 2 steps, (b) MUSA-I after 5 steps, (c) MUSA-II after 2 steps, (d) MUSA-II after 4 steps, (e) MUSA-III after 2 steps, (f) MUSA-III after 3 steps.

A cluster of refined grains were seen in MUSA-I processed material (Fig. 3.6(a,b)) along with the parent grains of original grain size. While some recrystallized finer grains can be observed for MUSA–II and III processes (Figure 3.6(c-f)), much of the grain structure consists of coarsened grains compared to MUSA-I.

Twin area fractions from optical microscopic study as a function of total engineering strain along the loading direction for the 3 MUSA processes are shown in Figure 3.7.

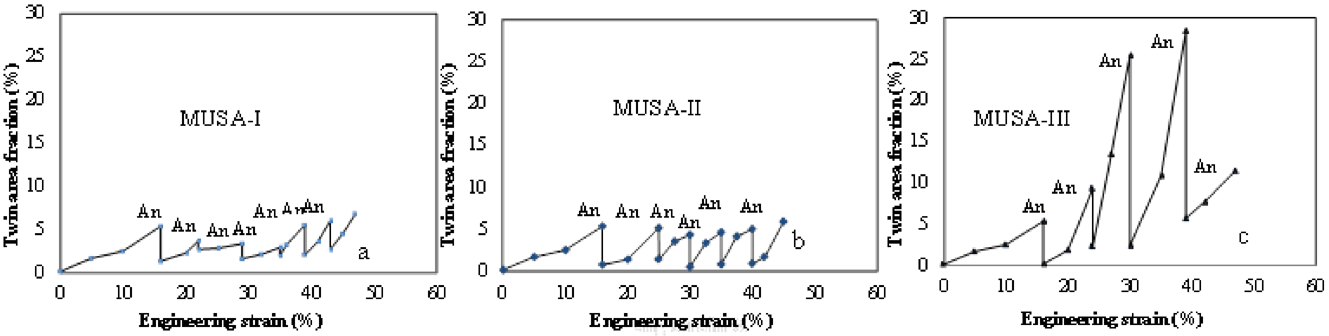

Fig. 3.7. Evolution of twin area fraction versus engineering strain during (a) MUSA-I, (b) MUSA-II and (c) MUSA-III (the symbol 'An' presents the annealing step).

The zig-zag shapes arise from the drop in the twin fraction resulting from intermediate annealing at each pre-strain step. For MUSA-I process, the residual twin fraction remained constant at about 2% while it dropped to near zero value for MUSA-II. For MUSA-III, the twin fraction increased more rapidly during pre-straining compared to the other MUSA processes as well as dropped significantly during annealing. In this case, the change in twin fraction on pre-straining and residual twin fraction on annealing increased with the number of MUSA steps. The role of twin fraction on work hardening characteristics and cumulative elongation is discussed in the next section.

To analyze the nature of the final failure at the microstructural level, optical microscopy was performed in the necked region where strains were large. Figure 3.8 shows optical micrographs from ND plane for each of the 3 MUSA processes and an engineering strain of about 0.46. The darker regions within the grains are evidence of micro-cracks that were often associated with twins within the grain. More of such twin-induced micro-cracks were visible in

MUSA-II and III specimens and less so in MUSA-I. While micro-cracks initiated at the twins, their propagation path was along the grain boundaries (see Fig. 3.8(c)).

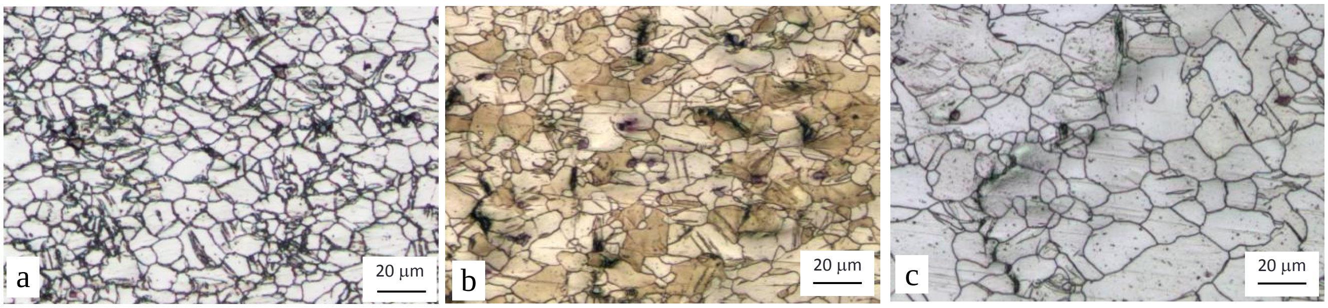

MUSA-I
200˚C-1 min
6 steps

MUSA-II
200˚C-60 min
5 steps

MUSA-III
400˚C-1 min
4 steps

Fig. 3.8. Optical micrographs showing the microstructure of AZ31 deformed by (a) MUSA-I after 6 steps, (b) MUSA-II after 5 steps, (c) MUSA-III after 4 steps.

As noted earlier in Figure 3.5, the grain size was a function of a specific MUSA process conditions. Twin induced recrystallization also led to grain reorientation affecting both the texture intensity and spreading. Comparing the macro-texture of annealed and MUSA-I (Fig. 3.9(a, b)), it is evident that texture intensity did not change significantly by grain refinement. Also, fine recrystallized grains on twins in MUSA-I did spread the final texture. In contrast, Fig. 3.9(c, d) for MUSA-II and III processes showed an increase in the texture intensity and spreading that is attributed to grain coarsening. The texture spreading appears similar to that achieved from continuous tensile tests at 200˚C and 400˚C (compare Fig. 3.9(c,d) with Figure 3.9(e, f)).

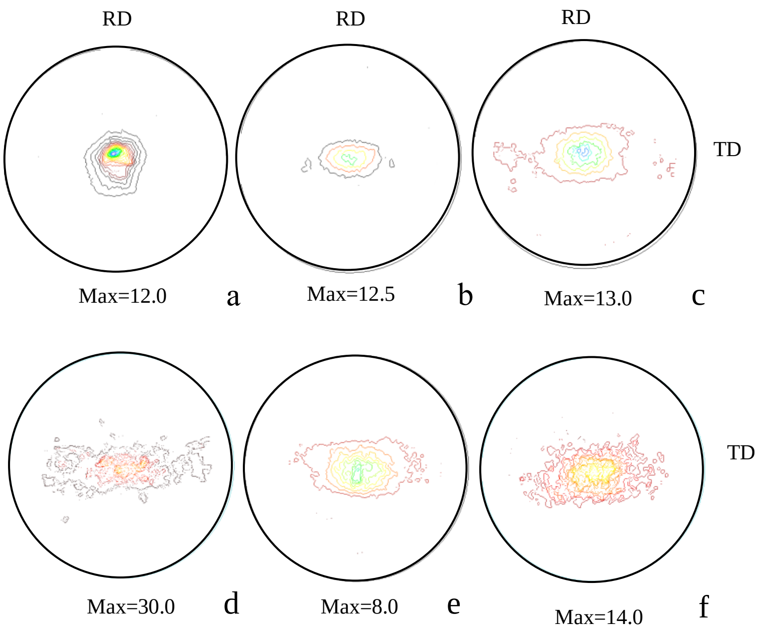

Fig. 3.9. Macro-texture results from XRD experiments showing (0001) pole figure on ND plane by XRD test for (a) H-24 annealed, (b) MUSA-I after 6 steps, (c) MUSA-II after 5 steps, (d) MUSA-III after 4 steps, (e) high temperature tensile test at 200°C, (f) high temperature tensile test at 400°C.

The micro-textures of MUSA-II from EBSD experiments for annealing, pre-straining and subsequent annealing are presented in Fig. 3.10. In agreement with the XRD results, the reference material (Fig. 3.10 (a)) is shown to have a strong basal texture. The overall intensity of textures, however, is different from that of XRD results. It is believed that the intensity from XRD could be more reliable due to larger areas of data collection. However, the detector shadow problem in XRD does limit the data collection for the poles distributed between 75˚ and 90˚. This could be resolved with the EBSD experiments. Therefore, the texture spreading without much increase in texture intensity can be observed after a few steps of MUSA in Fig. 3.10 (b-e). The intensity was observed to increase by pre-forming steps and decrease by the subsequent annealing steps. The contribution of twins towards texture spreading was found negligible in first few steps of MUSA-II. This can be inferred from the small pole intensities of the twins' orientations (~36˚ and ~86˚) in Fig. 3.10 (b,d). However, the contribution of twins adds up cumulatively over the steps and affects the final texture after 5 steps where a high pole intensity distribution at 86˚ (mis-orientation of the extension twin) and 36 ˚ appears with respect to the original pole position (see Fig. 3.10(e)).

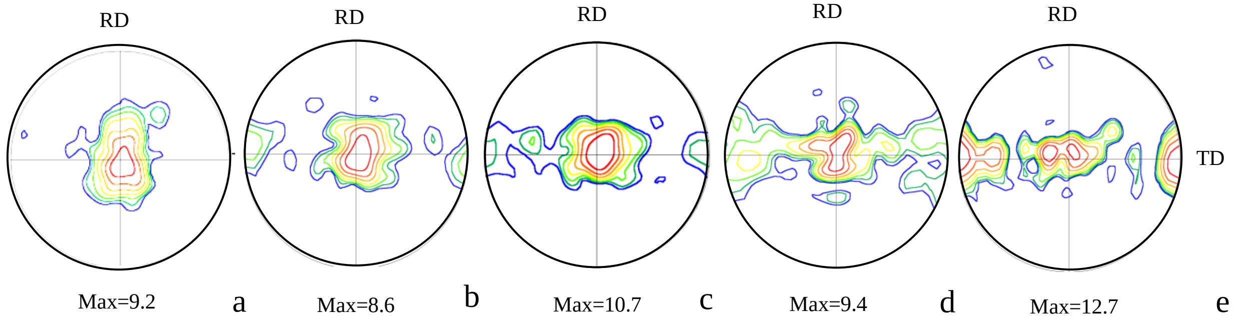

Fig. 3.10. Micro-texture results from EBSD experiments for MUSA-II specimens showing (0001) pole figure on ND plane by EBSD test for (a) H-24 annealed, (b) MUSA-II after first annealing, (c) MUSA-II after second pre-straining, (d) MUSA-II after second annealing and (e) MUSA-II after fifth pre-straining.

[3.4]. Discussion

[3.4.1]. The effect of MUSA process on the grain size of AZ31

A combination of pre-strain value and annealing conditions (temperature and time of annealing) as well as the number of steps affects the grain recrystallization and grain growth process and consequently the resulting grain size achieved in MUSA processed materials. The uniaxial tensile strain required for initiating the grain recrystallization in AZ31 has been reported to be in range of 0.01-0.03 [5]. The pre-strain values, as shown in Fig. 3.2, and verified by separate microstructural observations, was large enough in first step of all the MUSA processes to provide the driving force for recrystallization. In order to roughly estimate the starting and finishing time of recrystallization at 200˚C and 400˚C, the hardness values at a pre-strain of 0.17 were measured after annealing at 200˚C and 400˚C for a range of times (5 seconds to 1200 seconds). The results, as shown in Fig 3.11, indicated that the strength softening and recrystallization at 200˚C started between 30 seconds and 90 seconds. However, at 400˚C, the softening started almost immediately and finished after 50 seconds.

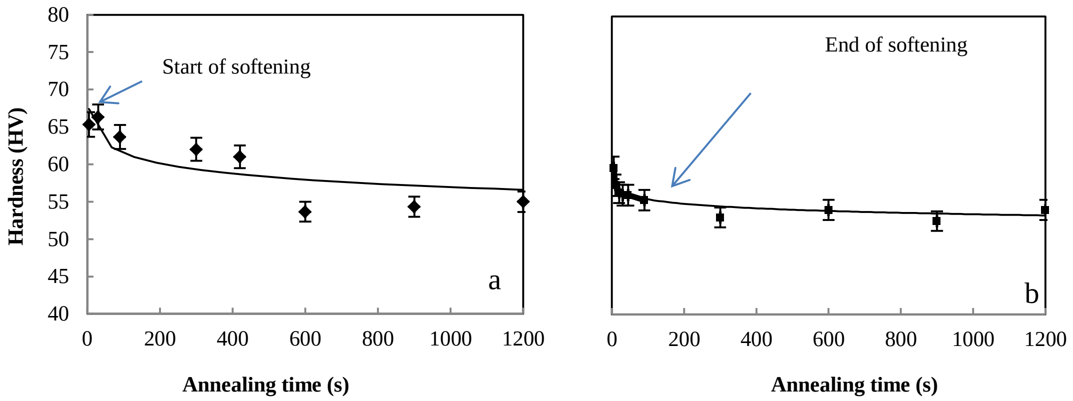

Fig. 3.11. Strength softening during annealing at different times for the 0.17 pre-strained AZ31 at (a) 200˚C and (b) 400˚C.

This is consistent with a variation in the grain size during MUSA-I, II and III processes with their respective annealing temperatures and times. For example, for MUSA-I process with annealing temperature of 200˚C and annealing time of 60 seconds, a decrease in grain size initially and a subsequent gradual increase was observed (see earlier Figure 3.5). The driving force for recrystallization comes from the pre-strains applied in the various steps. Also, as observed in Figure 3.6(a) for MUSA-I process after 2 steps of pre-straining, the number of newly recrystallized grains (at sizes smaller than the original grain size of 9.3 μm) exceeds the number of grains having the original grain size. This is indicative of the release of stored energy through early stage of recrystallization [7]. The gradual increase in grain size that is observed in the subsequent steps (again, see MUSA-I curve in Figure 3.5 and 3.6(a,b)) could be attributed to grain growth that is expected on further annealing after complete recrystallization, as observed by Zhang et al. for AZ31 [5]. MUSA-II, in contrast, started with negligible grain growth in the first two steps (see Fig. 3.6(c)). The annealing time was, however, long enough to complete the recrystallization and regain the original grain size in these steps. As the pre-strain dropped after the second step, grains began to rapidly grow from step 2 to step 3 by further annealing. The grain growth rate, however, was reduced in the subsequent steps due to larger initial grain sizes after the third step (Figure 3.5 and Figure 3.6(d)). A 3-stage behaviour similar to MUSA-II was observed in MUSA-III, where higher temperature of annealing as well as larger amount of pre-strain provided significantly more driving force which resulted in earlier and faster recrystallization and grain growth to occur [7] (see Figure 3.5 and Figure 3.6(e,f)).

[3.4.2]. The effect of MUSA process on work hardening behavior of AZ31

The strain hardening exponent (n-value) of a material, a measure of its work hardening ability, is typically related to rate of change of dislocation density (dislocation hardening). Dislocation density and thus the n-value is strongly influenced by obstacles or barriers to dislocation motion such as grain boundaries, sub-grains, dislocation cells and twins in magnesium alloys [7-10]. As the dislocation density increases, the rate of change of dislocation density decreases and consequently the work hardening capacity or the n-value is decreased. Larger grain size materials, in their annealed condition, have larger mean free path for dislocations and thus have a higher initial capacity for work hardening giving rise to a higher initial n-value. As noted in Fig. 3.4, the n-value is larger in MUSA-III compared to MUSA-I and II and the drop with number of steps is less. As with the grain size for MUSA-III, it is likely that dislocation hardening as discussed above and twin hardening (with wider and longer twins within the large grains, Figure 3.6(e,f) and Figure 3.7(c)) play important role in changing the n-value. For MUSA-III process with higher annealing temperature, the dislocation density at the start of each pre-strain step is expected to be lower (caused by significant dislocation annihilation during annealing) and is expected to rise more rapidly with pre-strain in a given step compared to the other two MUSA processes. Similarly, the twin fraction is somewhat higher for MUSA-III at the start of the pre-strain (especially for larger pre-strain steps, see Figure 3.7) compared to the other two MUSA processes. A higher initial twin fraction and rapid rise in twin fraction with pre-strain is expected to provide a stronger barrier to dislocation motion contributing further to dislocation hardening and increase in the n-value. Lastly, larger twins in MUSA-III also undergo twin hardening which can contribute to a higher n-value. It should be noted that the n-values for magnesium are lower than for other common formable Al alloys and steels and that is to be expected from its limited slip system activity compared the other materials. A progressive drop in n-value with number of steps for all three MUSA processes coupled with experimental observations of cumulative damage in the form of micro-cracks (Figure 3.8) leads to instability and failure of the specimens.

[3.4.3]. The effect of MUSA process on the yield stress of AZ31

A higher yield stress was reported in Figure 3.4(a) for MUSA-I and II processes compared to MUSA-III process. Also, in Figure 3.5, a lower grain size was observed for MUSA-I and II processes compared to MUSA-III process. As discussed by Barnett and co-workers [11, 12], a higher yield stress in fine grained Mg alloys is due to a higher level of stress which is required to activate the twins. The above quoted work provides support for MUSA-I process which exhibited a consistently smaller grain size as a function of number of MUSA steps (Figure 3.5) and a higher yield stress (Figure 3.4(a)). It appears that a similar explanation could be offered for coarse grain MUSA-III process and consequently lower yield strength values.

[3.4.4]. The number of required steps for a specific cumulative strain in MUSA

As the twins are hard to form in finer grained material than in a coarser grained material [11, 12], the MUSA-I material with finer grain size suppressed further twining with an increase in the number of steps (see Figures 3.7(a) and 3.8(a). The reduction in twin fraction from twin suppression resulted in a decrease in the failure strain at each subsequent step. Therefore, MUSA-I took more steps to get to the desired cumulative strain (see Figure 3.4(c)). The larger grain size and consequently larger twins that were developed by MUSA-II and III (see Figs. 3.6(e, f)) helped reorient a larger portion of microstructure into favorable orientation for dislocation slip. It is believed that this provided larger strain accommodation at each pre-strain step, and consequently, smaller number of steps was required to get to the desired cumulative tensile ductility.

[3.5]. Conclusions

MUSA was shown as an effective process to enhance the uniaxial tensile ductility of AZ31 at room temperature. The benchmark strain of 0.35 at 200°C from continuous tensile test was achieved in three steps of MUSA with annealing at 200°C for 1 minute whereas 0.48 at 400˚C was achieved in four steps of MUSA at 400˚C for 1 min. The work hardening rate and other material properties were quantified as a function of number of MUSA steps for all three MUSA processes that were experimentally studied. The grain size, twin fraction and texture were shown to be affected by the three MUSA process parameters. The twin fraction and twin formation rate in each step of pre-forming were quantified and were found to be dependent upon pre-strain values at each step, as well as the temperature and time of intermediate annealing. Micro-cracking was observed at the twins at large strains in all three MUSA processes. The development of such micro-cracks along with a progressive reduction in n-value with increasing pre-strain steps are likely the two dominant mechanisms that limit the cumulative fracture strain for the three MUSA processes. The shorter annealing time for MUSA-I was shown to reduce the grain size and decrease the twin activity. However, longer time or higher temperature of annealing (i.e., MUSA-II and III processes) improved twin activity and resulted in larger texture spreading and further increase in uniaxial tensile ductility of AZ31. Largest cumulative fracture strain in fewer MUSA steps was achieved for MUSA-III process arising from higher annealing temperature and shorter annealing times. This methodology can be applied to industrial stamping processes to improve the formability of AZ31 magnesium sheet at room temperature.

References

[1]. X. Huang, K. Suzuki, M. Yuasa, Y. Chino, Mater. Sci. Eng. A 587 (2013) 150–160.

[2]. A. Bussiba, A. Ben Artzy, A. Shtechman, S. Ifergan, M. Kupiec, Mater. Sci. Eng. A 302 (2001) 56–62.

[3]. D. H. Kang, D.W. Kim, S. Kim, G.T. Bae, K.H. Kim, N. J. Kim, Scripta Mater., 61 (2009) 768-772.

[4]. J. J. Li, S. Kim, T. M. Lee, P. E. Krajewski, H. Wang, S. J. Hu, Mater. Sci. Eng. A 582 (2011) 3905-3914.

[5]. H. Zhang, G. Huang, L. Wang, J. Li, Scripta Mater., 67 (2012) 495-499.

[6]. L. Jiang, J.J. Jonas, R.K. Mishra, A.A. Luo, A.K. Sachdev, S. Godet, Acta Mater. 55 (2007) 3899–3910.

[7]. F.J. Humphreys, M. Hatherly, Recrystallization and related annealing phenomena, second ed., Elsevier, 2004.

[8]. Z. M. Li, A. A. Luo, Q. G. Wang, L. M. Peng, P. H. Fu, G. H. Wu, Mater. Sci. Eng. A 564 (2013) 450–460.

[9]. Z. Fun, H. Mingzhi, S. Deke, Mater. Sci. Eng. A 122 (1989) 211-213.

[10]. M. Knezevic, A. Levinson, R. Harris, R. K. Mishra, R. D. Doherty, S. R. Kalidindi, Acta Mater. 58 (2010) 6230–6242.

[11]. O. Muransky, M. Barnett, D. Carr, S. Vogel, E. Oliver, Acta Mater. 58 (2010) 1503-1517.

[12]. M. R. Barnett, Scripta Mater. 59 (2008) 696–698.

Chapter 4

Effect of surface modification on cumulative tensile ductility of AZ31 Magnesium sheet

The study reported in this chapter was mostly conducted by this doctoral candidate (Mahdi Habibnejad-korayem) with continuous supervision, over a period of 4 .5 years, by his supervisor, Dr. Jain, and occasional technical advice from Dr. Mishra of General Motors (GM), the industrial sponsor of the project. Some experiments related to texture measurements were assisted by Mr. Kubic of GM as well. The chapter was prepared by this candidate with many discussions of its structure, focus, content, conclusions, language, and writing style with Dr. Jain. This paper is an extended version of a short published paper in Materials Science Forum Vols. 828-829 (2015) pp 340-344 for publication in a peer reviewed journal

Effect of Surface Modification on Cumulative Tensile Ductility of AZ31 Magnesium Sheet

Mahdi Habibnejad-korayem [a,1], Mukesh K. Jain [a], Raja. K. Mishra [b]

a McMaster University, Department of Mechanical Engineering, Hamilton, ON, Canada L8S4L8
b General Motors Research and Development Center, Warren, MI 48090, USA

Abstract

Wire brushing and annealing (WBA) process was developed, optimized and utilized to modify the surface layer microstructure of AZ31 automotive magnesium sheet material. The wire brushing process was carried out using softer brass wire brushes to mitigate the effect of wire brushing on surface quality and damage. The influence of modified surface grain structure and crystallographic texture was studied by continuous uniaxial tension test as well as by a newly proposed multi-step uniaxial stretching and annealing (MUSA) process to assess its cumulative uniaxial tensile ductility. A rotational speed of 2800 RPM for the wire brush with a near-zero depth of cut followed by annealing at $200^{\circ}C$ for 60 minutes resulted in acceptable surface quality with a refined grain layer of depth 30 μm, and a modified crystallographic texture on the surface. Material flow behavior, grain microstructure and texture evolution of WBA processed material during subsequent MUSA process was analyzed to assess the role of wire brushing in enhancing the MUSA response of AZ31 sheet. Original fully annealed AZ31 sheet (in the non-WBA condition) was also subjected to identical MUSA process for comparison purposes. The results showed improvement in terminal uniaxial tensile ductility of WBA-MUSA processed material compared to Standard-MUSA material. The ductility improvement is attributed to non-basal texture development and tilt in texture, as well as to grain refinement within the highly deformed surface layer from the combination of WBA and MUSA processes.

Keywords: AZ31; wire brushing; annealing; texture; microstructure; tensile ductility

[4.1]. Introduction

---

[1] Corresponding author

Mg alloys, as the lightest structural metallic materials available commercially in large scale, are finding increased application in automotive industry. Their applications, as a rolled sheet material for conventional stamping, have been limited by their poor room temperature formability compared to Al alloys and steel. Severe plastic deformation (or SPD) processes such as equi- channel angular pressing (ECAP), differential speed rolling (DSR) and friction stir welding (FSW) etc., have been shown to impart a fine grain structure and a more randomized crystallographic texture to magnesium sheet surface [1-6]. Such microstructural and textural modifications have been shown to improve their ultimate tensile strength and tensile ductility. The above processes are still quite limiting in terms of room temperature ductility for conventional stamping, cost-effective production, and required commercial blank sizes for automotive applications. More conventional surface modification processes such as wire brushing (WB) [7-9], shot peening (SP) [10] and surface mechanical attrition treatment (SMAT) [11] may have certain advantages for automotive stamping applications over others noted above, and for the limitations noted above. Specifically, wire brushing, often employed for surface polishing and rust removal, has been shown to refine the surface layer grain size of various ferrous and non-ferrous materials such as steel, Al, Cu, Pb [7] and Mg [8]. Most of these studies have focused on development of nano-size surface grains from dynamic recrystallization that occurs during wire brushing and their role in improving uniaxial tensile strength [7-11]. Relatively little attention has been paid to the role of annealing on surface layer microstructure and crystallographic texture development, both of which are linked to uniaxial tensile ductility. Also, no effort has been made to subject pre-processed sheet by any of the aforementioned processes to large strains by subsequent multi-step forming and annealing process. In recent studies, present authors aimed to fill this gap by focusing on formability improvement of annealed AZ31 sheet by multi-step uniaxial stretching and annealing (MUSA) [12], and multi-step bending and annealing (MBA)[13]. By changing annealing conditions and pre-strain values in different deformation steps, the grain structure and texture of AZ31 sheet was modified which led to significant gains in room temperature tensile ductility and bendability [12, 13]. There are still gaps in attaining desirable room temperature ductility in magnesium sheet for automotive stamping applications. The objective of the present paper, therefore, is to exploit the combined potential of wire brushing and multi-step forming and annealing processes to improve the room temperature formability of magnesium sheet. Specifically, this study aims to combine wire brushing and annealing (or WBA) as a pre-process and MUSA as a subsequent process to assess the cumulative room temperature ductility of AZ31 magnesium sheet. Both of these processes are studied experimentally using suitable microstructural and texture characterization tools and techniques in an attempt to analyze the relationship between process parameters, surface quality, grain structure and texture development, and to correlate process and material parameters to cumulative uniaxial tensile ductility.

[4.2]. Experimental procedure

[4.2.1]. Materials and processing

AZ31 magnesium sheet of 1.5 mm thickness in the H24 temper condition was annealed at 400˚C for 2 hours and cut along the rolling direction (RD) to a size of 300 mm × 200 mm. The sheet was then subjected to wire brushing process on a milling machine (Figure 4.1) using brushes with steel and brass wires. The wire brush assembly was rotated at 500, 1500 and 2800 RPM values, as it was pressed against and moved over the surface of the sheet along the rolling direction at a feeding rate of 1 mm/s. The depth of cut was kept constant during the process at values of 0, 0.5 and 1 mm so that either the tip of wires touched the surface or the surface was swept by the assembled wires, as shown in Figure 4.1(b). Wire brushing process was then followed by annealing at 200˚C for 60 minutes.

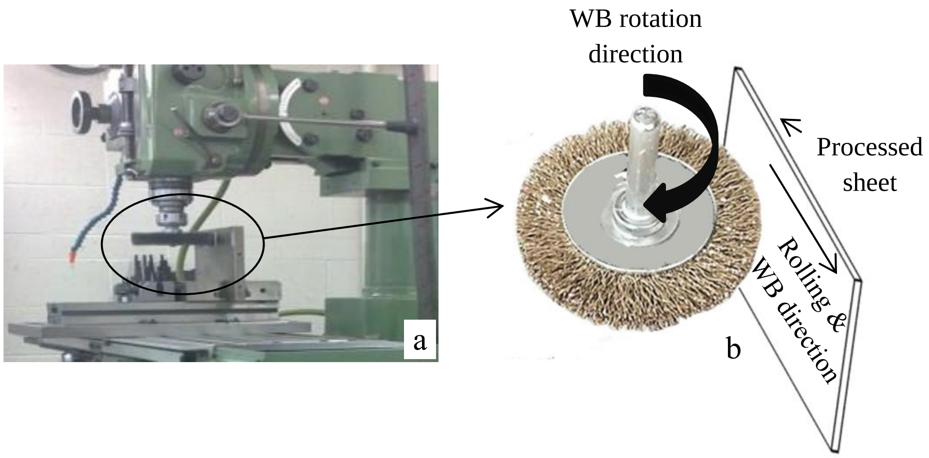

Fig. 4.1. (a) Set up for wire brushing on a milling machine and (b) schematic illustration of the brass wire brush during rotation on the processed sheet.

[4.2.2]. Microstructural characterization

Specimens for the microstructure study were prepared by sectioning, polishing and etching. The polishing was done by 9 μm, 3 μm, and 1 μm diamond solutions, followed by 50 nm colloidal silica slurry. The polished samples were etched with picric acetic solution (1 ml acetic acid, 1 ml water, 420 mg picric acid and 7 ml ethanol) for 3 seconds to reveal the grain structure. Samples for texture studies were polished and etched as above, but given a final short etch (5–10 seconds) with a solution of 60% ethanol, 20% water, 15% acetic acid and 5% nitric acid. Grain size measurement on polished and etched LT plane was carried out by the grain count method (number of grains per unit area) using metallographic images from an optical microscope (Nikon, Model: DS-Fi2-ECLIPSE LV100) at a magnifications of 100X and 200X. The surface quality and topography of as-received and WB materials were characterized using Zygo NewView 5000 white-light interferometer.

The textures were obtained by 3 different techniques namely X-ray diffraction (XRD), electron backscattered diffraction (EBSD) and focused ion beam (FIB) due to the complementary nature of these techniques. For example, XRD provided data from a larger depth (or volume) of sample but at the expense of lesser sensitivity to surface deformation compared to EBSD. A high resolution EBSD system fitted to a Zeiss N-Vision FIB with field emission electron gun was used for smaller step size scans of the sample surface that was not possible with Leo 1450 SEM. XRD texture measurements were performed using Bruker D8 DISCOVER diffractometer equipped with a cobalt sealed tube source, Vantec 500 area detector, parallel focus Goebel mirror, and Chi cradle. The sample to detector distance was 20 cm and the power setting was 35 kV and 45mA during the experiment. Texture analysis and construction of pole figures were carried out using GADDS software package. EBSD was conducted by using a LEO 1450 SEM at an acceleration voltage of 20 keV, a working distance of 18 mm, and a tilt angle of 70˚. The SEM was equipped with commercial TSL data acquisition software that utilizes a dynamic theory of electron diffraction for formation of Kikuchi bands and an automated indexing algorithm for determination of crystallographic orientations. The data collection was done on ST plane with an area of observation of 150 μm × 200 μm (length × thickness). This data was then projected on to ND plane with a 90˚ rotation about TD (transverse direction) axis to be consistent with the reported results in the literature for Mg alloys. EBSD maps are reported for only those points with a confidence index (CI) and image quality (IQ) higher than 0.1 and 150 respectively. These values were obtained from fully recrystallized AZ31 as they represented minimum values for acquiring the mis-orientation patterns in deformed grains. The grains with CI and IQ values below and above 0.1 and 150 were classified as deformed and deformation free respectively. High resolution EBSD experiments was carried out using a Zeiss N-Vision field emission scanning electron microscope (FE-SEM) at an acceleration voltage of 20 KV with a working distance of 15 mm and a tilt angle of 70°.

Fractography was performed on failed uniaxial tensile specimens from H-24 and WBA materials to assess any surface-topography induced damage and crack initiation, using SEM (model JEOL 6610LV).

[4.2.3]. Determination of tensile properties from continuous tests and MUSA processes

Annealed and selected WBA-processed materials were machined along the rolling direction (RD) in to 10 mm wide and 100 mm long tensile specimens (ASTM-10.1520/B0557M-14) and tested on a servo-hydraulic mechanical test system (MTS, model # 312.31) equipped with a clip-on extensometer to control the strain rate. Multi-step uniaxial stretching and annealing (or MUSA) process consisted of the following. First sample was pulled to fracture at an initial strain rate of $0.01s^{-1}$(MUSA-step 1). The second sample was pulled to 85-90% of the first sample elongation to fracture, followed by annealing at 400˚C for 1 minute (MUSA-step 2). The third sample was pulled to 85-90% elongation of a sample that mimicked the deformation and annealing history of the second sample but was taken to fracture. The deformation was again followed by annealing at 400˚C for 1 minute (MUSA-step 3). The pre-straining and annealing steps were repeated using the above methodology to steps 4 and 5 to obtain a cumulative true strain value. For more details about the MUSA process, the reader is directed to reference [12]. Two different starting materials for MUSA process were considered in the present work; (i) an annealed material (i.e., H24 temper material with an original warm rolled surface from an industrial rolling process, annealed at 400˚C for 120 minutes in the laboratory), and (ii) a wire brushed and annealed (WBA) material with annealing after wire brushing at 200˚C for 60 minutes. The former and latter processes are referred to as Standard-MUSA and WBA-MUSA processes in the rest of the paper.

Micro-hardness measurements were carried out on polished specimen surfaces using CLEMEX micro-hardness tester fitted with a Vickers pyramidal indenter to obtain an understanding of local strength characteristics though the sheet thickness. For this purpose, an indention load of 25 gf for a dwell time of 15 seconds was utilized. Average micro-hardness values were obtained from triplicate tests from indentations observed at a magnification of 400X.

[4.2.4]. Surface roughness measurements

Average surface roughness (R_a) was measured with a portable digital surface roughness tester (Model: TR100, Obsnap Instruments) equipped with a diamond probe of tip radius of 10±2.5µm. For these measurements, a force-based probe-specimen contact limit of 0.75mN with an accuracy of ±15% was utilized. The probe was positioned normal to the sheet surface.

[4.3]. Results

This section presents grain structure and texture results first and then the macroscopic uniaxial tensile loading response of WB and WBA materials. This is followed by a comparison of microscopic and mechanical test results for Standard-MUSA and WB-MUSA materials.

[4.3.1]. WB process parameters and material properties

The wire brushing parameters and resulting material properties are given in Table 4.1.

Table. 4.1. Wire brushing parameters and wire brushed materials properties

	WB parameters		Wire brushed material properties		
	RPM	Depth of cut (mm)	Remaining thickness (mm)	Roughness R_a (µm)	Hardness (HV)
Annealed	0	0	1.57	4.22	70±5
Wire brushed with Brass	500	0	1.5±0.05	5.25	72±5
		0.5	1.5±0.05	5.31	72±5
		1	1.5±0.05	5.53	70±5
	1500	0	1.4±0.05	5.45	80±5
		0.5	1.4±0.05	5.51	80±5
		1	1.3±0.05	7.56	80±5
	2800	0	1.4±0.05	5.8	85±5
		0.5	1.4±0.05	7.3	80±5
		1	1.3±0.05	9.02	80±5

As shown, WB caused some material removal from the surface which led to a reduction in original thickness, surface roughening as well as surface hardening as indicated by micro-hardness values, all commensurate with increasing depth of cut and spindle rotational speed. Brass wire-brushed surfaces typically appeared brighter as the original brown-tinged warm-rolled oxidized surface layer was removed. Typical surfaces for as-received and WB materials are shown in Figure 4.2(a-c). The original as-received surfaces exhibited clearly noticeable roll lines through the oxidized surface as well as from optical profile measurements (see Figure 4.2(a)). Depending on the processing parameters, the wire brushing process resulted in either slightly deeper scratches (see Figure 4.2(b)) or significant grooves on the surface that were unacceptable for subsequent forming (Figure 4.2(c)). Line scans from Figures 4.2(a-c) indicating roughness profiles are shown in the figures that are inserted in Figures 4.2 (a-c) where relative deterioration in surface quality from wire brushing can be noted.

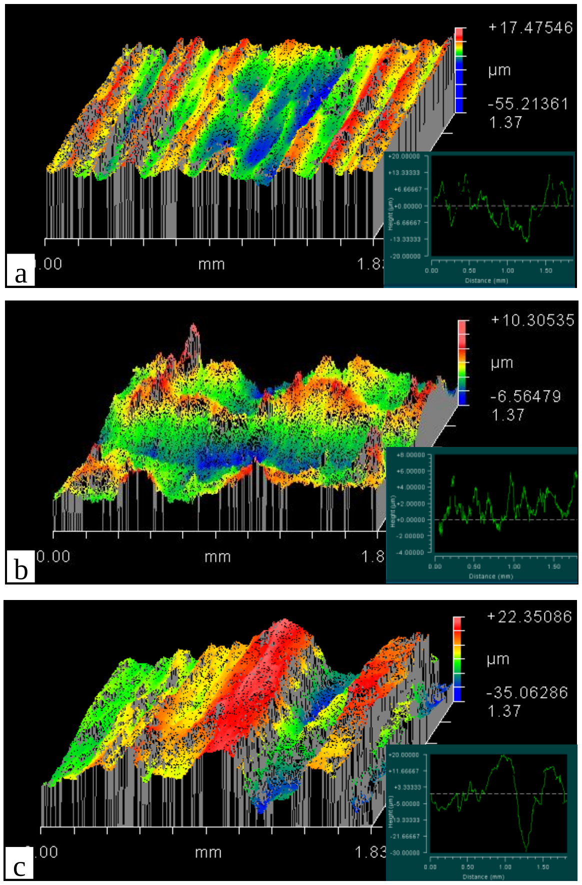

Fig. 4.2. Surface appearance of the wire brushed AZ31 using (a) H-24 material, (b) wire brush at 2800 RPM and 0 mm depth of cut, (c) wire brush at 1500 RPM and 1 mm depth of cut. Plots show the scratches' heights on samples.

It should be noted that no brass contamination from the brass brushes was observed on AZ31 sheet surface.

[4.3.2]. Microstructure of WB and WBA materials

[4.3.2.1]. Grain structures

Figure 4.3 shows optical micrographs from ST plane corresponding to 3 different WB conditions in Table 4.1. The right side corresponds to the wire brushed surface. Depending upon spindle speed and depth of cut, twinning, uniform and abnormal grain growth can be noted. At 500 RPM and a depth of cut of 1 mm, a uniform grain size with extensive twin formation (blue arrows in Figure 4.3(a)) as well as some abnormal grain growth was observed in the sub-surface layers (as shown by black arrows). Increasing the brush rotational speed, however, resulted in appearance of a deformed and refined layer on the surface, as shown in Figure 4.3(b).

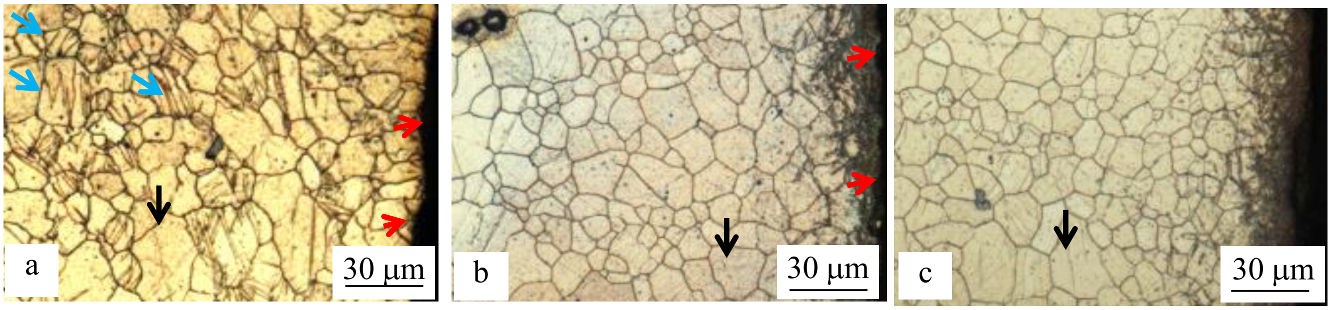

Fig. 4.3. ST plane micrographs of the Brass wire brushed AZ31 at (a) RPM: 500, DC:1 mm, (b) RPM: 1500, DC: 0 mm, (c) RPM: 2800, DC:0. Blue arrows point at twins, black arrow point to abnormal grains and red arrows show scratches on the surface.

This layer, to a depth of 20-30 μm from the surface, was noticeably different in terms of grain structure from that in the interior of the material. Grains were difficult to resolve by optical metallography due to their ultra-small size from severe plastic deformation. The nature of this layer will be discussed in details in the discussion section. On the other hand, relatively coarser grains were observed in the internal regions below the depth of 30 μm. At the highest tested rotational speed, 2800 RPM, the affected layer appeared to be more uniform and the extent of abnormal grain growth in the sheet interior (as shown by black arrows in Figure 4.3(c)) was reduced. There was also smaller number of scratches seen on the surface (showing by red arrows) at this processing condition. This processing condition therefore was selected for further annealing and investigation of texture development and uniaxial tensile properties.

[4.3.2.2]. Textures

Texture of original AZ31 sheet after annealing in the form of EBSD based OIM maps are shown in Figure 4.4.

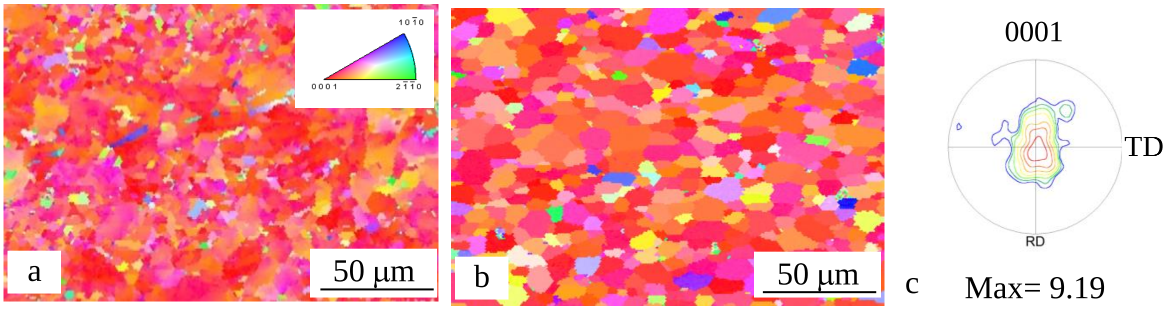

Fig. 4.4. EBSD results showing OIM map of (a) ND plane, (b) ST plane with 90 ˚ rotation and (c) {0001} pole figure of annealed AZ31.

The data in the form of inverse pole figure (IPF), and (0001) pole figure (PF) are taken from sheet normal and short transverse planes where a large majority of the grains are shown to have basal orientation. A strong basal texture with a maximum intensity of 9.19 is present from rolling process at the center of pole figure. Similar data for WB processed AZ31 sheet from ST plane in Figure 4.5 shows a bi-layer grain structure of large matrix grains where surface grains appear in the form of a random dot pattern due to experimental limitations (raised by large deformation) in analyzing them. The various OIMs shown in Figure 4.5 are essentially expanded large magnification images of sub-regions within lower magnification OIM in Figure 4.5(a) to illustrate textural characteristics and limitations of the data. As Figure 4.5(b,c) illustrates, no distinct grains which characteristic Kikuchi pattern for grain orientation analysis could be discerned within the refined surface layer even with FIB at 1000X magnification and small step sizes. This is not to suggest that sub-micron grains did not exist in the WB surface layer region, but only that sample preparation/inspection techniques utilized were unable to reveal them in texture measurements. Figure 4.5(d) shows the OIM map of region next to the fine grain surface layer where some twin formation (shown with black arrows) can be noted. Twins in single and lamellar structure were detected primarily when their thickness was large.

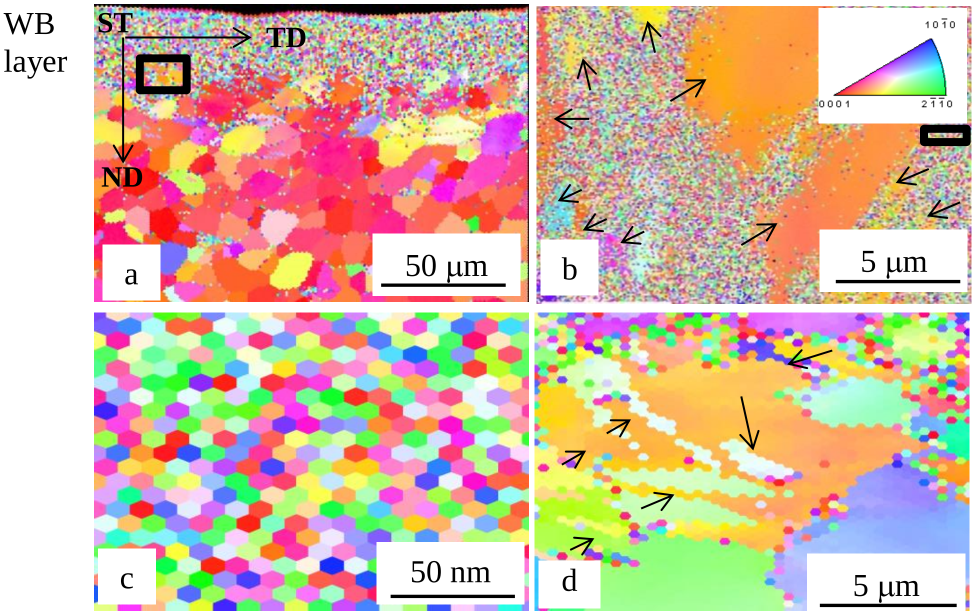

Fig. 4.5. OIM maps of the wire brushed microstructure on ST plane (a) from EBSD experiment at 200X and step size of 1 μm (b) from FIB experiment at 1000X and step size of 100 nm in small box that is drawn in Fig. 4.5(a), (c) from FIB experiment at 1000X and step size of 5 nm in small box that is drawn in Fig. 4.5(b) and (d) from FIB experiment for the bottom layer at 1000X and step size of 100 μm.

OIM map of WBA-processed material, as shown in Figure 4.6(a), indicates that larger recrystallized surface grains could be analyzed. The map reveals very fine grains in the surface region with non-basal orientation in blue, pink and yellow. The grain size increased rather rapidly in the transition region between the surface and sheet interior. Grains from the surface region in WBA-processed sheet indicate that they have been rotated by 90° about the c-axis towards the prismatic planes $\{10\bar{1}0\}$. Also, in contrast to WB material, no twins were identified in the transition region between the surface and sheet interior, the latter exhibiting majority of the grains with basal orientation as in the original annealed material. An optical micrograph of WBA processed material, presented in Figure 4.6(b), also shows a rapid grain size change in the transition region from surface towards the sheet interior with a size rather close to the original annealed material. Overall, grain size in the surface layer was refined to 5.5 μm and up to a depth of about 30 μm.

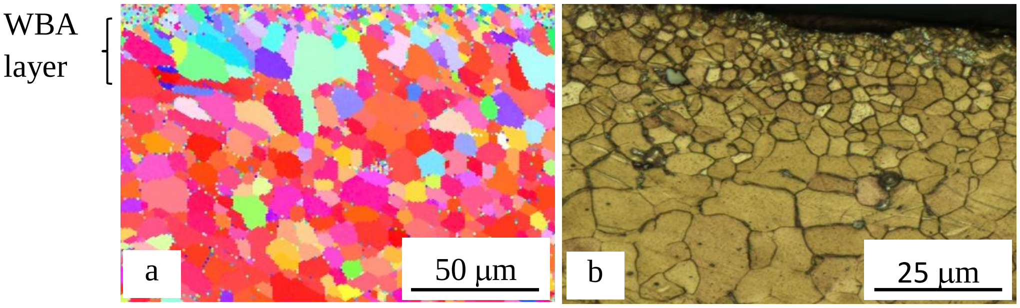

Fig. 4.6. The ST plane observation of the wire brushed and annealed AZ31 (a) OIM map from EBSD with 90˚ rotation on ND plane, (b) optical micrograph.

EBSD results in the form of through-thickness (0001) pole figures from ST plane for WB and WBA processed materials are compared in Figure 4.7.

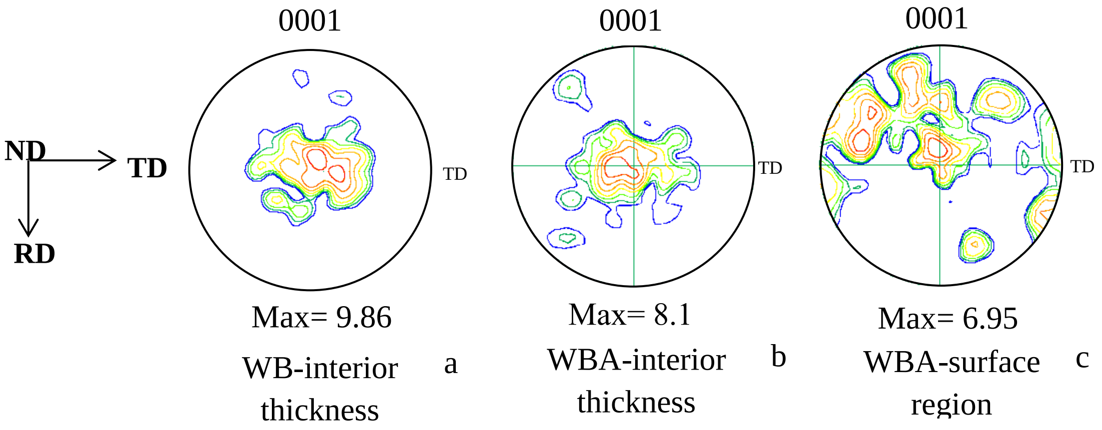

Fig. 4.7. (0001) pole figure of the ST plane from EBSD experiment for (a) the interior region of WB processed, (b) the interior region of WBA processed, (c) the surface region of WBA processed AZ31.

For the interior region of WB sample (Figure 4.7(a)), a bimodal pole distribution, consisting of a larger contour at the center and a smaller contour to the right, was observed. The maximum intensity in this region remained almost unchanged from that of as-received material. As with earlier OIM data, no reliable pole figure could be obtained from highly deformed surface region. By annealing the wire brushed material, pole distribution in the interior region rotated back to the strong basal texture of as-received material with a drop from 9.86 to 8.1 in maximum intensity due to annealing step of WBA process. Surface region of this material (Figure 4.7(c)) exhibited significantly tilted texture with poles distribution largely concentrated in the upper half of pole figure. Maximum texture intensity decreased even further for this layer in comparison to mid-thickness region.

As mentioned earlier, additional texture experiments using XRD technique were carried out on ND plane of WB and WBA processed materials to see if surface layer pole figure could be obtained by this method. The results, shown in Figure 4.8(a,b), exhibit similar shear textures for both materials in terms of high intensity contours at the center, and pole distribution towards center-left and center-right regions of the pole figures.

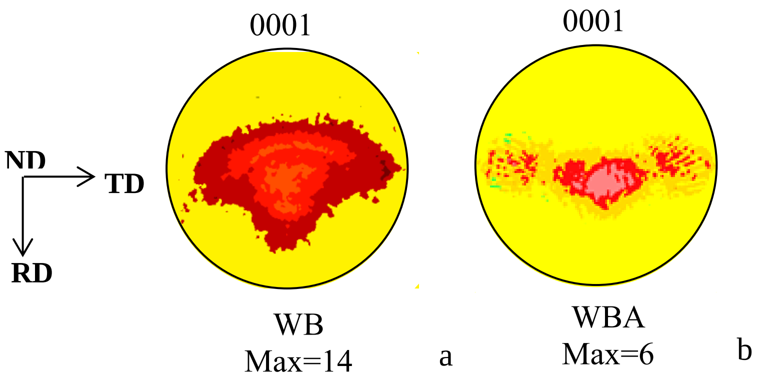

Fig. 4.8. (0001) pole figure of the ND plane by XRD experiment for (a) the surface region of WB processed and (b) the surface region of WBA processed.

The maximum intensities, however, differed significantly as they increased from about 9.19 in the annealed material to about 14 for WB material and then decreased on subsequent annealing (for WBA) to 6. Comparing Figure 4.8(b) with the earlier EBSD results in Figure

4.7(c) indicates absence of distributed poles at the 90˚ position with respect to the center. This could be ascribed to detector shadow problem in XRD which limits data collection for poles distributed between 75˚ and 90˚. It is to be noted the material volume (or depth below surface) for pole figure determination by XRD was larger compared to EBSD technique.

[4.3.3]. Mechanical properties of WB and WBA materials

Engineering stress–strain curves from uniaxial tensile tests are shown in Figure 4.9 where general work hardening characteristics and limiting strains of materials in H-24, annealed, WB and WBA conditions can be observed. Note that n-values, as a measure of work hardening corresponding to the different stress-strain curves, are shown directly on the graph. As expected, the H-24 temper material (curve 1) is already in partially deformed condition from warm rolling and thus exhibits rapid work hardening to saturation and fails early. Annealed material exhibits much lower yield strength and shows a long regime of work hardening to saturation and larger limit strains.

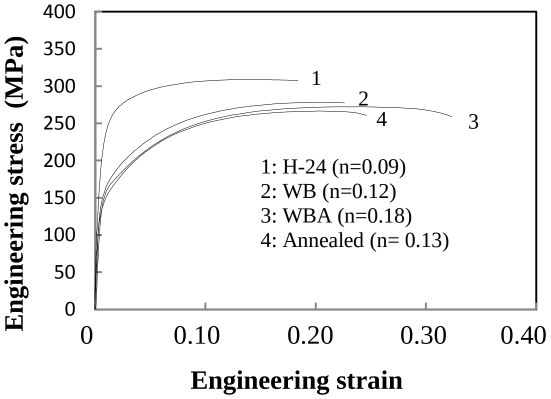

Fig. 4.9. Stress-strain curves for AZ31 samples in monotonic tensile tests.

An intermediate response between H-24 temper and annealed material is exhibited by the WB material since it consists of annealed microstructure in the sheet interior and a high work hardened surface from the WB process. However, the work hardening behavior is rather close to the annealed condition. Lastly, the WBA material also exhibits work hardening similar to the annealed material but a long regime of stable flow followed by localized necking (as shown by slight stress drop) and fracture. The resulting limit strain for this material of about 0.34 was significantly higher than the other tempers and processing conditions.

[4.3.4]. Microstructure of Standard-MUSA and WBA-MUSA materials

The results presented in this section include both Standard-MUSA and WBA-MUSA materials. While the emphasis is on WBA-MUSA material, the former are included as a bench mark for comparison purposes**.** Standard-MUSA process was defined earlier in Section 4.2.3.

[4.3.4.1]. Grain structures

A set of representative optical micrographs of Standard-MUSA and WBA-MUSA processed materials after MUSA steps 1 and 3 are shown in Figure 4.10.

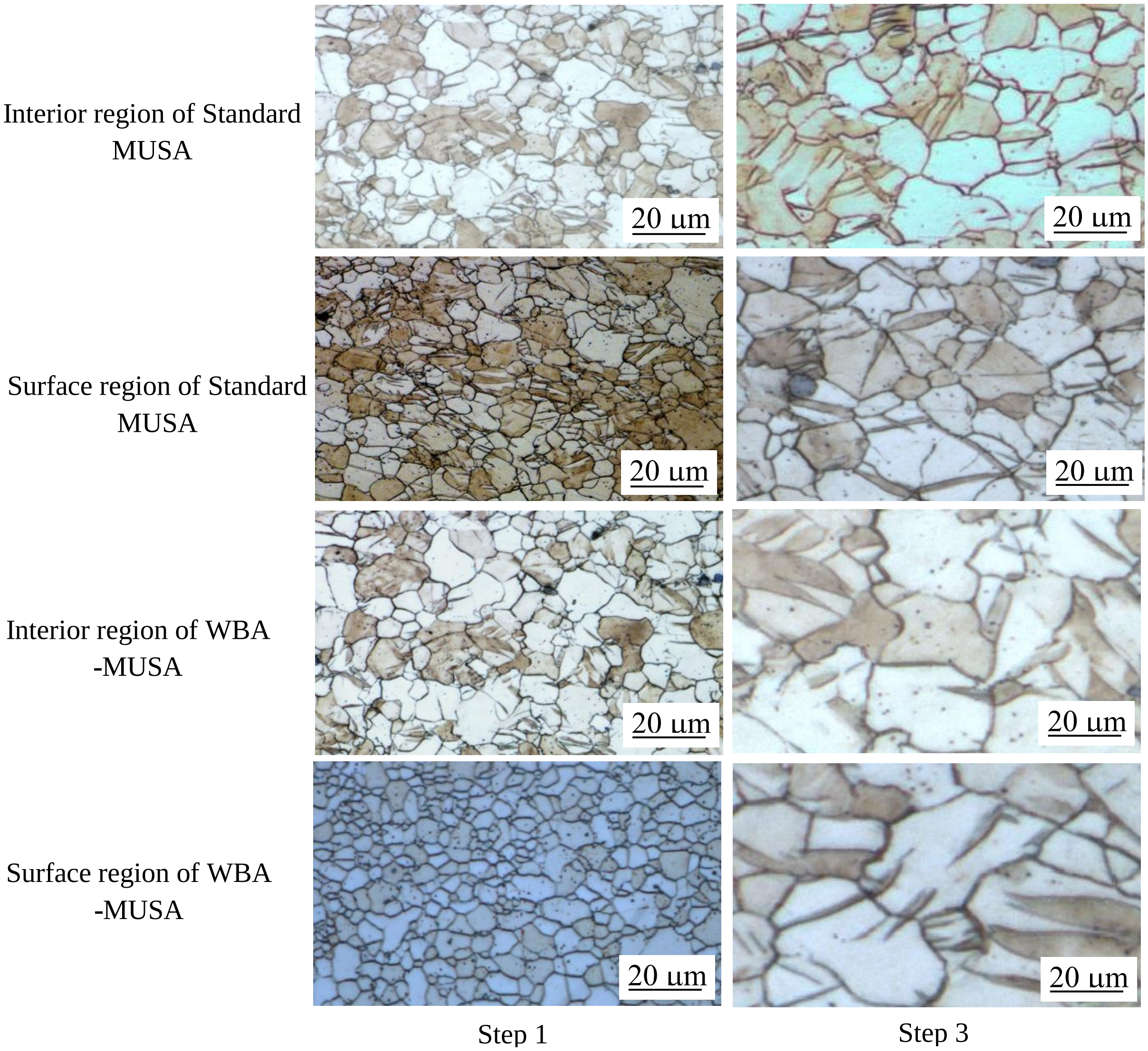

Fig. 4.10. Optical micrographs showing the microstructure of standard MUSA and WBA-MUSA processed materials.

Significant grain coarsening is evident at step 3 for all the cases as well as twinning in the larger grains in step 3. No twinning was observed in smaller grains corresponding to surface regions, especially in the original WBA material. Grain coarsening trends for the two MUSA processed materials for sheet interior and surface regions, as shown in Figure 4.11, were largely similar with WBA-MUSA process representing grain size band lower and upper limits corresponding to surface and sheet interior at each MUSA step.

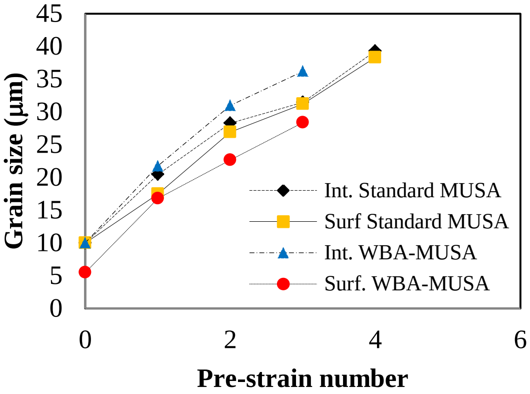

Fig. 4.11. Grain size measurement for the interior and surface regions of both annealed and WBA processed materials.

[4.3.4.2]. Textures

A set of OIM maps from interior and surface regions of Standard-MUSA material for different MUSA steps are presented in Figure 4.12. Predominantly dark micrographs from pre-strained materials (i.e., prior to annealing at each step) at earlier MUSA steps did not yield any reliable grain mis-orientation pattern as the CI and IQ values stayed below their threshold values, as mentioned earlier. This was largely because of deformed grain structure from pre-straining resulted in development of dense dislocation networks in the microstructure. Subsequent grain growth from intermediate annealing, however, did alleviate this problem as evident in MUSA steps 3-5 where mis-orientation patterns for most of the grains could be captured. It is to be noted that the extent of pre-strain varied between MUSA steps, and consequently the extent of grain recrystallization from identical annealing condition (400˚C, 1 minute between steps) also varied.

Therefore, some MUSA material still had deformed microstructure due to incomplete grain recrystallization which led to rather limited grain mis-orientation data for these cases. This is reflected in a scatter of dark EBSD micrographs in the montage presented in Figure 4.12.

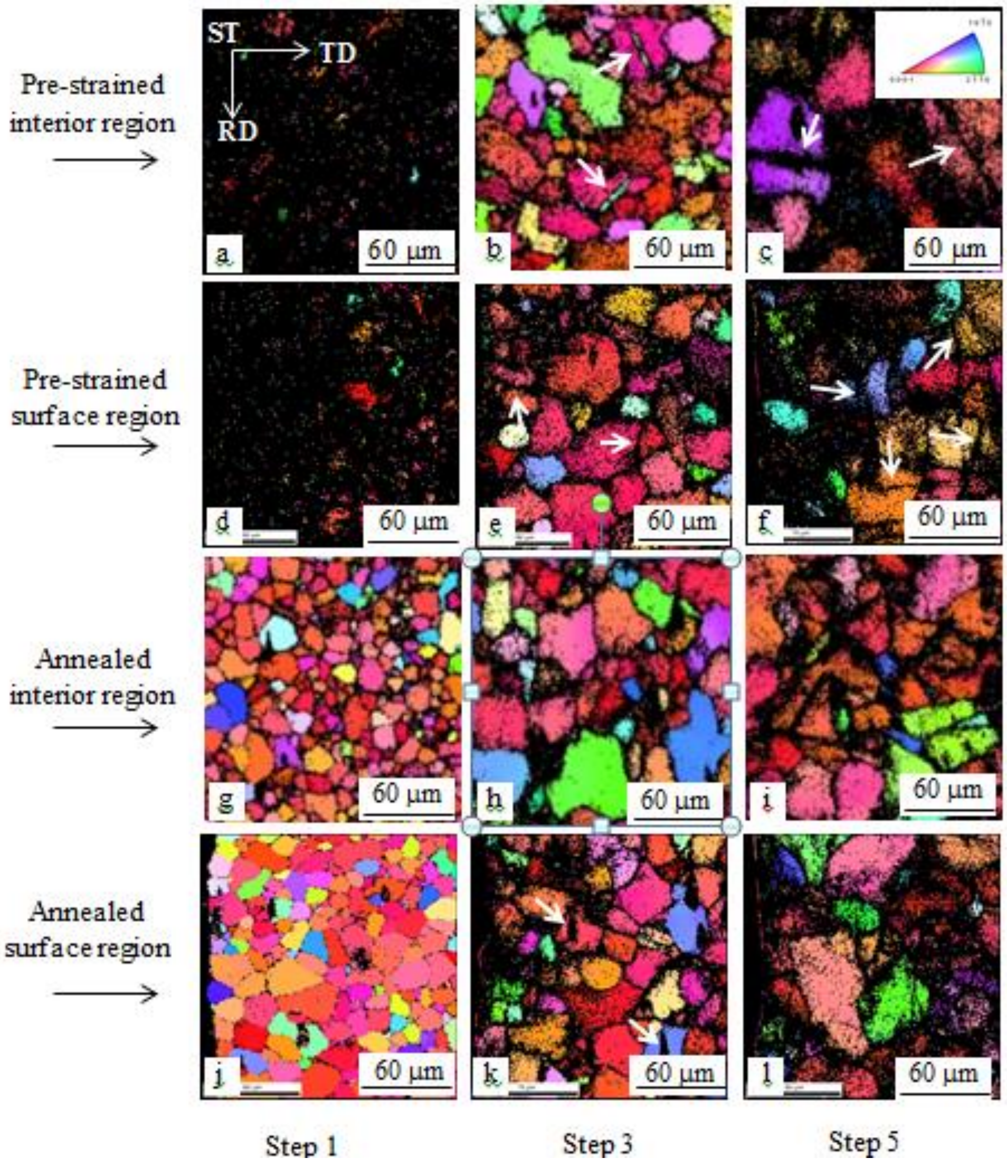

Fig. 4.12. EBSD micrographs from ST plane of AZ31 during deformation and annealing steps of standard MUSA process; (a-c) interior thickness after deformation, (d-f)) interior thickness after annealing, (g-i) surface region after deformation (j-l) surface region after annealing. The numbers at the bottom show the pre-straining or annealing step number of MUSA process.

In spite of these limitations, some useful texture characteristics can be noted from the micrographs. For example, after step 3 pre-straining, a few wide twins (mostly extension twins based on point to point mis-orientation analysis) are evident in Figure 4.12(b) which subdivide the grains with basal orientation (location of twins are marked by arrows). Also, a 90˚ grain rotation from basal orientation $\{0001\}$ to non-basal orientation $\{2\bar{1}\bar{1}0\}$, as indicated by inset IPF, can be observed in grains that appear green in Figure 4.12(b). As MUSA proceeded, pre-strained material exhibited increased twin fraction and narrower twins in the microstructure. In larger steps of MUSA, some grains rotate less than 40˚ and appear orange and purple in Figure 4.12(c). Similar features to the interior region can be pointed from Figures 4.12 (d-f) for the grains in the surface region. MUSA material after annealing, as shown in the bottom 2 rows of Figure 4.12(g-l), generally yielded better mis-orientation patterns for most MUSA steps. After MUSA step 1 annealing, a cluster of fine grains in the midst of coarsened original grains, but with similar mis-orientation, could be observed in the sheet interior. As MUSA step number increased, bands of refined grains with new mis-orientations appeared in the surface region. A larger fraction of grains with $\{10\bar{1}0\}$ non-basal poles were revealed in the annealed microstructure in comparison to the pre-strained microstructure. However, grains from pre-straining step with non-basal orientation of $\{2\bar{1}\bar{1}0\}$ and small fraction of twins still remained in the microstructure after annealing.

Results complementary to Figure 4.12 in the form of (0001) pole figures for Standard-MUSA material are shown in Figure 4.13 where a strong basal texture in the interior of pre-strained samples after MUSA steps with some spread towards TD is noted (see row 1). The results also show a continuous increase in the maximum texture intensity as the MUSA steps increase. In the surface region (see row 2), however, a bimodal pole distribution was developed in the first step of pre-straining that continued to develop and became more diffuse with increase in MUSA steps and a rather high maximum texture intensity was reached at the last step where some poles were present at almost 90˚ with respect to the pole figure center (see row 3). Relatively larger texture spreading was observed in the sheet interior after annealing but the texture intensities were low and increased more gradually with MUSA steps. With respect to annealed surface texture, multiple poles with some asymmetry around the center of the pole figure were observed, and the maximum texture intensity rose gradually to reach a value similar to the sheet interior as the MUSA steps increased (see row 4).

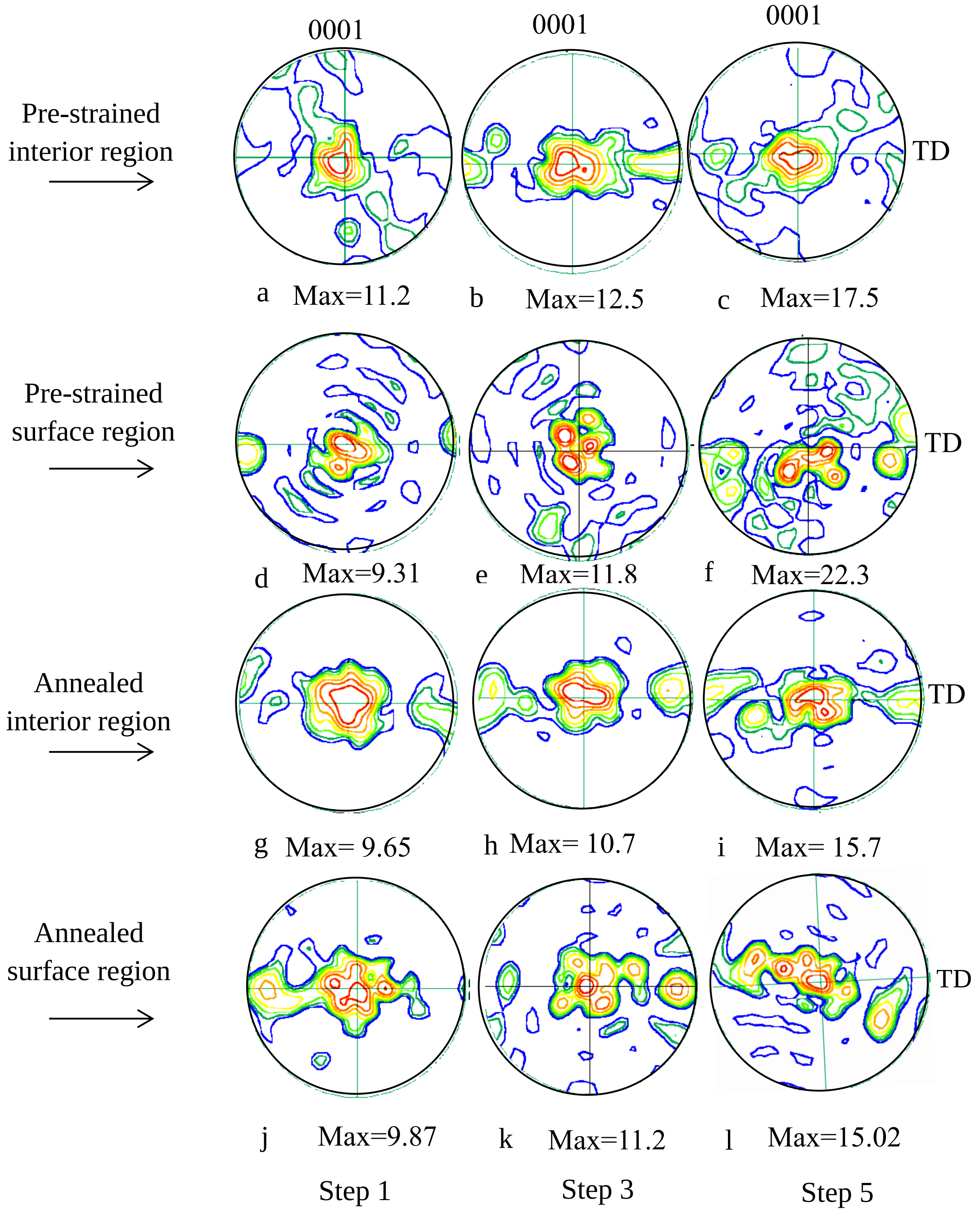

Fig. 4.13. Micro-texture results from ST plane of EBSD experiments for MUSA process of annealed AZ31 showing (0001) pole figures for (a-c) interior of the thickness after deformation, (d-f) interior of the thickness after annealing, (g-i) surface region after deformation (j-l) surface region after annealing. The numbers at the bottom show the pre-straining or annealing step number of MUSA process.

Comparable OIM data to earlier Figure 4.12 for Standard-MUSA material from ST plane through the sheet interior and surface of WBA-MUSA materials are shown in Figure 4.14.

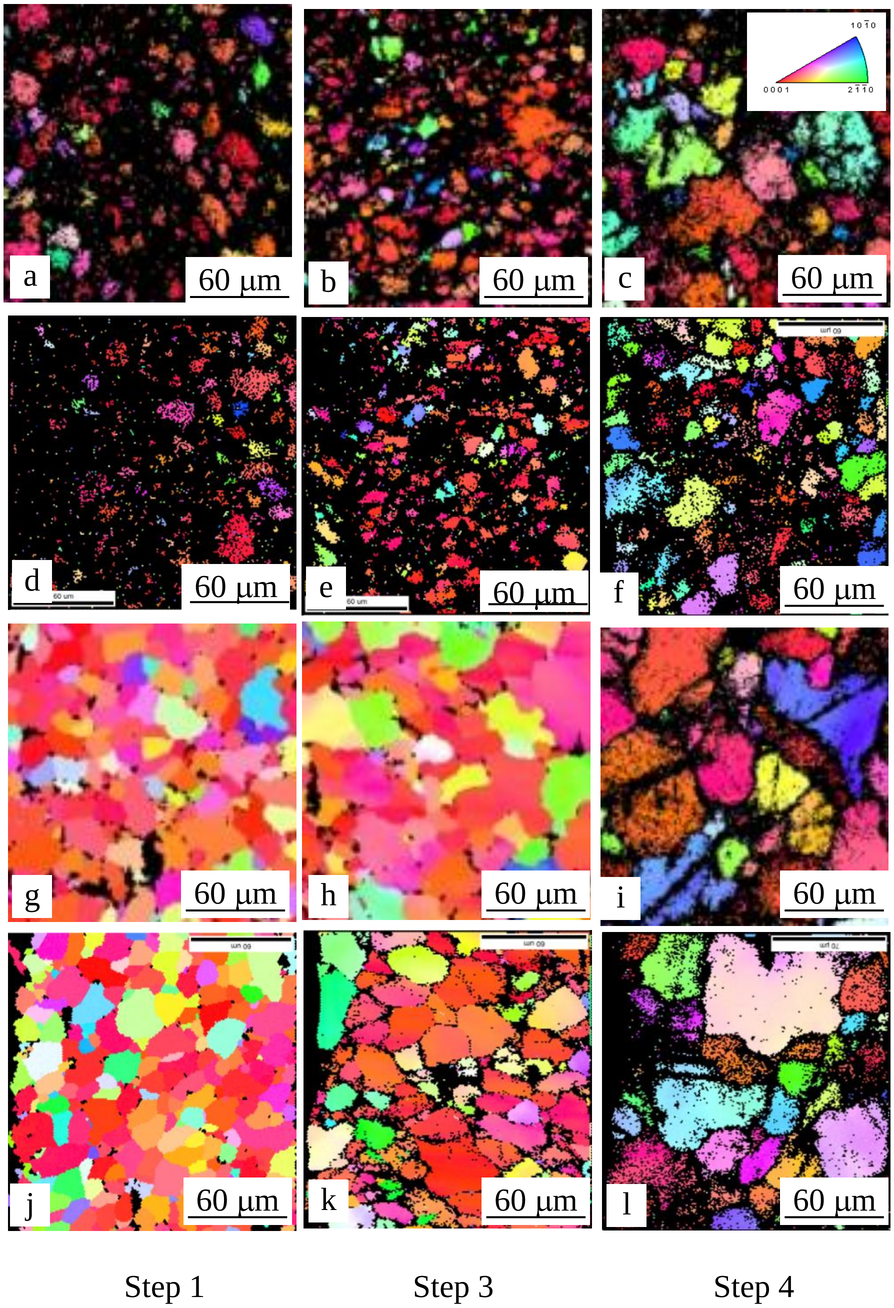

Fig. 4.14. EBSD micrographs of WBA processed AZ31 during deformation and annealing steps of MUSA process; (a-c) interior of the thickness on ST plane after deformation, (d-f) interior of the thickness on ST plane after annealing, (g-i) surface region of ST plane after deformation (j-l) surface region of ST plane after annealing. The numbers at the bottom show the pre-straining or annealing step number of MUSA process.

Rather large deformation was present at the end of pre-strains for each MUSA step compared to the annealed materials, and only a small fraction of grains could be reliably analyzed due to experimental issues described earlier with reference to Figure 4.12. In Figure 4.14, grains with basal orientation are marked with red and pink and constitute a large majority of grains whereas non-basal orientations appear in smaller numbers at smaller MUSA steps in blue, green and yellow (see rows 1 and 2). In general, surface grains revealed a large fraction of grain with non-basal poles compared to the interior. Figure 4.14, in contrast with earlier results in Figure 4.12, indicates that only a few grains were subdivided by twins in MUSA deformation of WBA processed materials (mainly noticed in the microstructure after fourth pre-straining). On annealing, mis-orientation patterns were successfully captured for most of the grains through the sheet thickness. After the second annealing, however, a large portion of grains had a high dislocation density from pre-straining, and thus appeared dark in the map. Significant texture spreading occurred in later MUSA steps as indicated by grains in a range of colors with pink and orange representing basal, and green, blue, and yellow representing non-basal and twin mis-orientations. This occurred specially in grains located in the surface region compared to the rest of grains (see row 4). As observed earlier for Standard-MUSA material (Figure 4.12), significant grain coarsening occurred in the annealed micrographs. However, short annealing time of 1 minute was found to be ineffective in removing the entire twin content of microstructure specifically after step 4 pre-straining.

As shown earlier, OIM micrographs are compared with (0001) pole figure representation for WBA-MUSA material in Figure 4.15. With a few exceptions, the majority of the pole figures indicate significant texture spreading from center of pole figure toward TD orientation, both in pre-strained and annealed states for all MUSA steps. In other words, a broader texture distribution occurs in WB-MUSA material where the poles were concentrated horizontally along the diameter of pole figure in comparison to Standard-MUSA material (see earlier Figure 4.13). Also, the texture spreading along the horizontal is strongly bi-modal in nature. The maximum texture intensity are larger in pre-strain state than in annealed state and increase more rapidly in the last stages for pre-strained state and more gradually for annealed state. These results are discussed in more detail in section 4.4 once the uniaxial tensile behavior of WB-MUSA materials has been presented in section 4.3.5.

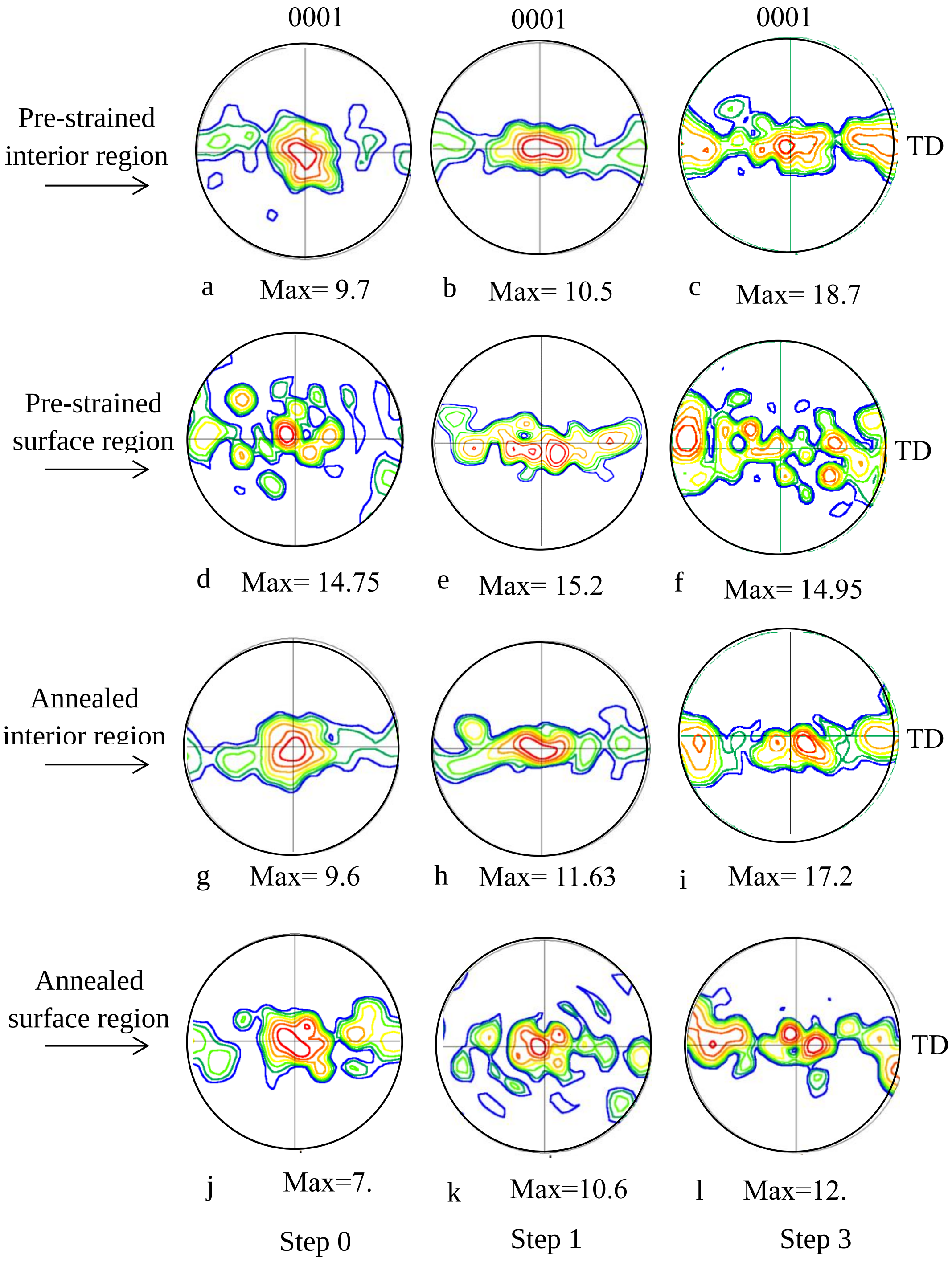

Fig. 4.15. Micro-texture results from EBSD experiments for MUSA process of WBA processed AZ31 showing (0001) pole figure for (a-c) center of thickness after deformation, (d-f) center of thickness after annealing, (g-i) sub-surface layer after deformation (j-l) sub-surface layer after annealing. The numbers at the bottom show the pre-straining or annealing step number of MUSA process.

[4.3.4.3]. Grain recrystallization fraction

OIM results from the previous section were reanalyzed to obtain a rough fraction of deformed and recrystallized grains during MUSA pre-straining and annealing steps. The smallest fraction of the deformed grains was observed in the third pass of Standard-MUSA process (see Figure 4.16(a)). Leaving aside an anomaly in the data for Standard-MUSA material at step 3, the fraction of deformed grains for the two materials are rather close with Standard-MUSA curves from center and surface regions staying slightly below those from WBA-MUSA material. Also, a slight drop in deformed grain fraction with increasing number of MUSA step can be noted. In general, a higher fraction of deformed grains was found in the surface regions compared to the interior region. Fraction of recrystallized grains for the two processing conditions is shown in Figure 4.16(b) where a significantly higher value for WBA-MUSA material can be noted. The scatter seen in the data is likely from variation in pre-strains between MUSA steps and its effect on subsequent annealing kinetics as discussed earlier with reference to Figure 4.12. Also, the curves for sheet interior and surface regions follow each other rather closely for both processed materials. It is quite possible that recrystallization kinetics were similar for the two regions.

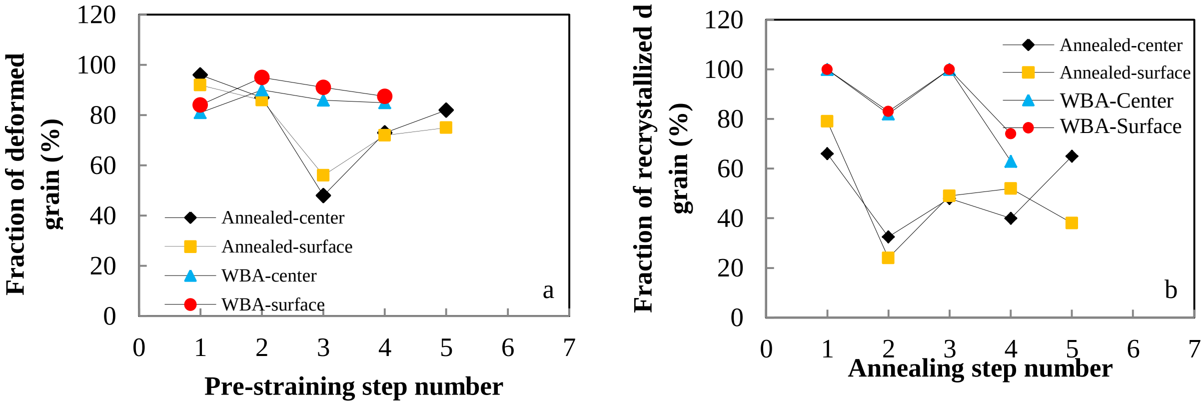

Fig. 4.16. EBSD results showing the fraction of (a) deformed grains and (b) recrystallized grains for both annealed and WBA processed materials.

[4.3.5]. Mechanical properties of Standard-MUSA and WBA-MUSA processed materials

Figure 4.17(a,b)) shows the uniaxial tensile stress-strain behavior of Standard-MUSA samples after 4 steps and WBA-MUSA processed samples after 3 larger steps.

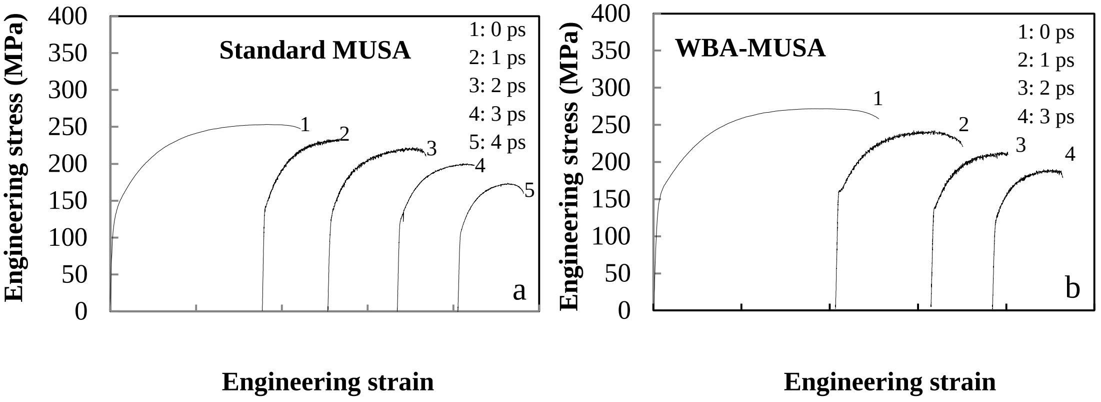

Fig. 4.17 (a) Engineering stress-strain responses of AZ31 during (a) standard MUSA process (b) WBA-MUSA process. The abbreviation “ps” stands for pre-strain number in the history of material.

Both sample histories led to a cumulative strain of about 0.6. While initial yield strength was significantly higher for WBA-MUSA material in the earlier stages, a similar descending trend in yield strength (YS) and ultimate tensile strength (UTS) was observed for the two MUSA materials (see Figure 4.18(a,b)). For Standard-MUSA material, the stress level upon reloading in the subsequent step then gradually reached the stress level at the end of last deformation step at about the same work hardening rate. Whereas WBA-MUSA material, in spite of its higher yield strength, exhibited a higher work hardening rate in the first 2 steps in order to achieve similar uniaxial tensile ductility in only 3 MUSA steps. A progressive loss of the work hardening exponent with number of MUSA steps was observed in Fig. 4.18(c) for both materials. The n-value was observed to be higher for WBA processed material in the first two passes of MUSA and then fell below that of annealed material after the second pass of MUSA. It is to be noted that cumulative elongation values in Figure 4.18(d) could only be achieved at 400˚C in monotonic continuous tensile tests [16]. Also, the Standard-MUSA, published separately by the present authors, have shown that the benchmark cumulative strain of high temperature deformation of AZ31 (200˚C and 400˚C) could be achieved in several steps depending on the intermediate annealing condition [16]. WBA results in Fig. 4.18(d), however, show a further reduction in the number of steps over Standard-MUSA process to achieve total elongations values equivalent to that of monotonic tension at higher temperature.

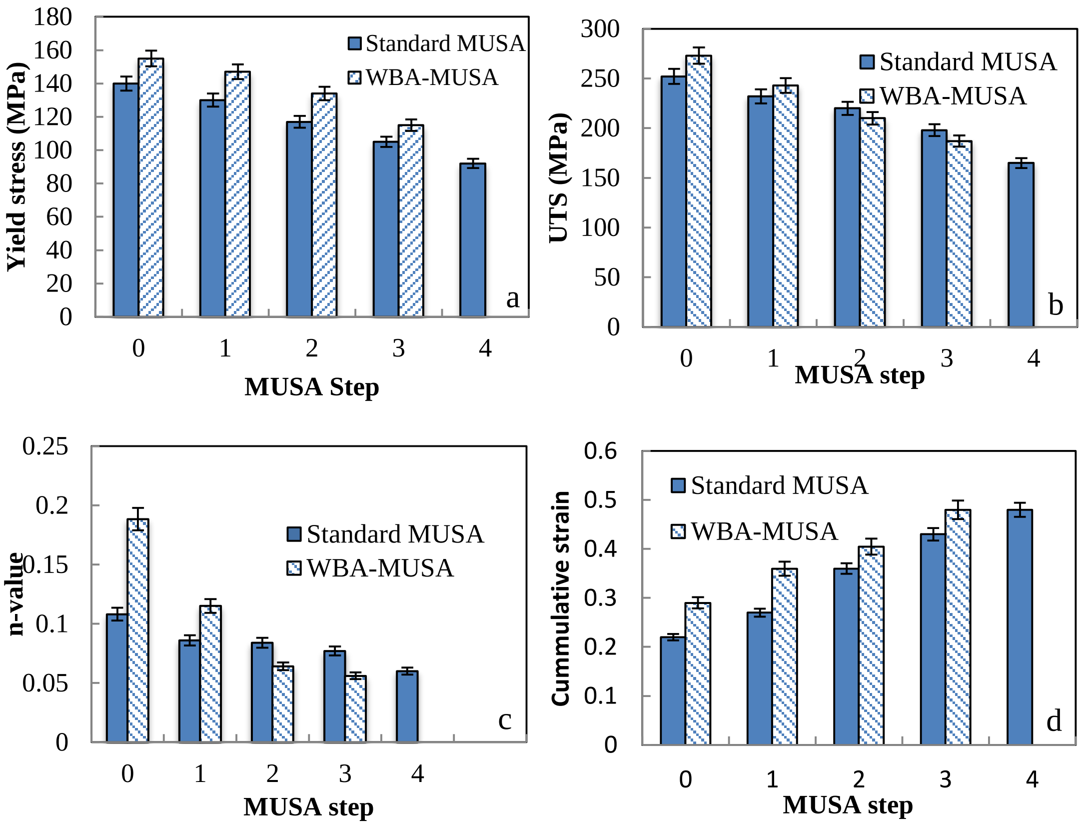

Fig. 4.18. The changes in the mechanical properties of annealed material and WBA processed materials as a function of MUSA step number for (a) yield stress, (c) ultimate tensile strength, (c) n-value and (d) cumulative elongation.

[4.4]. Discussion

[4.4.1]. Mechanics of wire brushing process

Wire brushing is a common surface cleaning process generally employed for material removal in many industrial applications. A roughened surface from wire brushing (Figure 4.2) as well as sub-surface deformation (Figure 4.3) suggest that the wire brushing not only removes material but also displaces small amounts of material from its original location to a nearby location due to large local plastic deformation. The deformation is primarily in simple shear in the plane of the sheet that results from friction between brush wires and the work piece surface. Shear induced plastic deformation is a function of friction coefficient, applied normal pressure to the specimen and yield strength in shear of the sheet (work piece) material [9]. At zero depth of cut, wire brush lightly contacted the sheet and no plastic loading of the surface occurred during brush rotation. This, as well as roughly similar strengths of brass wires and AZ31 Mg sheet, resulted in minimum surface hardening and roughening of the AZ31 sheet surface at lower RPM values (see Table 4.1). At higher RPMs, however, significant normal loading of the surface occurred as well as some penetration of the surface by the brush wires. Consequently, sheet surface was subjected to larger shear deformation and material removal leading to both surface roughening and hardening. This effect was more pronounced for steel wire brushes that are commonly used in the literature [7-9] where strength differential between the steel wires and the processed sheet is rather large and the resulting surfaces are unacceptable for any subsequent forming. With increasing depth of cut, there was clear interference between the wires and the AZ31 sheet surface which resulted in significant normal loading of the surface. Also, softer brass wires acted like a cantilever beam under transverse end loading that caused bending of the brushes on the sheet surface which tended to reduce the penetration of the wires into the surface but this likely increased the contact area and friction. When the bending was significant, minimum penetration of the wires occurred and a scratch free sheet surface was obtained with limited material removal (see Figure 4.2(b)). The process still resulted in some material removal from the surface but in a more uniform manner (see Table 4.1). Some extension twins were also observed at higher depth of cut (see Figure 4.3(a)) which could only occur due to additional compressive loading of the surface.

[4.4.2]. Grain structure

Several different microstructures resulting from the wire brushing process consisted of original, largely unaltered microstructure, microstructure with small amount of deformation and many twins (Figure 4.3(a,b)), and highly deformed microstructure (Figure 4.3(c)) depending upon depth of cut and spindle speed. Under light loading conditions of low depth of cut and spindle speed, the microstructure underneath the deformed layer remained largely unaffected. Twinned microstructure resulted from compressive loading of surface grains with strong basal texture caused by increasing depth of cut and speed, a well-accepted twinning mechanism for HCP Mg [13]. Some twinning was observed even beneath the deformed layer (Figure 4.5(d)) under intermediate depths of cut and brush rotation. With more aggressive wire brushing conditions of high depth of cut and brush rotation, the deformation became shear dominated with virtually no evidence of twin formation in the deformed layer (Figure 4.5(a-c)), and likely resulted in dense networks of dislocations. Friction induced heating during wire brushing has been reported to cause recovery of the surface by dislocation annihilation and activation of dynamic recrystallization [8,9]. However, no significant heating of AZ31 sheet was observed under the relatively gentle wire brushing conditions in the present work. Therefore, following wire brushing, an annealing step was applied to achieve a uniform layer of recrystallized grains on the surface (Figure 4.6). Softer brass wire brushes were rather effective in limiting material removal and controlling the depth of deformed surface layer.

With respect to grain structure development in WBA-MUSA process, the extent of pre-strain as well as temperature and time of annealing governed the grain recrystallization kinetics as reported recently by the present authors [12]. As per this study, uniaxial pre-strain in the range of 0.05-0.08 with a rapid anneal (1 minute at 400˚C) was sufficient to achieve grain recrystallization during the MUSA process. A complete recrystallization in the initial steps of MUSA was followed by normal grain coarsening which favored twining in the subsequent pre-straining step. The grain coarsening also reduced the rate of recrystallization in the next annealing step and increased the number of un-recrystallized twins after the next annealing step. However, a more careful consideration of the amount of pre-strain and annealing times (perhaps longer and without excessive grain growth) would have been more suitable to achieve more consistent grain recrystallization in all MUSA steps and make the process more robust as the amount of deformation and rate of recrystallization are related [14].

[4.4.3]. Texture evolution

Significant grain rotation (or texture spreading, as observed from the pole figures (Fig 4.7, 4.8)), during WBA process was likely induced by shear deformation since more aggressive wire brushing conditions were related to increased texture spreading. As shear was maximum on the surface and progressively diminished with depth, the initial basal texture (providing parallel basal planes to the surface) decreased in strength, and new near {0001} textural components appeared that tended to align with through-thickness macroscopic shear planes. This is attributed to the maximal rotation angle around the <0 0 0 1> axis which is limited to 30° due to restrictions from symmetry of the HCP crystal structure [15]. According to Suhuddin et al. [15], it is likely that other possible slip systems were activated to accommodate the rotation. Among prism, basal and pyramidal, only the prism slip could provide a lattice rotation around the <0 0 0 1> direction [15]. Although friction induced heating can aid the activation of such non-basal slip systems in the sheared zone [9], subsequent annealing of wire brushed surface was also seen to spread the texture in the present work (Figure 4.7 and 4.8). Further, as the annealed texture was a result of recrystallization of the deformation texture, it was found to have common components with the deformed texture.

The texture change during MUSA process could be related to prevailing deformation mechanisms. For example, pole figures in Figs. 4.13 and 4.15 for Standard-MUSA and WBA-MUSA processes, show a concentration of high intensity contours at the center of pole figures indicating activation of basal slip by lattice rotation. However, inhomogeneous local deformation bands and shear banding, as observed previously by the authors in AZ31 Mg [12, 13], also contributed to texture spreading. These additional deformation mechanisms could provide near basal components giving the bimodal or a more diffuse poles distribution. This is more evident in the surface regions where strain localization is more likely to occur. It is to be noted that contribution for the non-basal slip systems can still occur at room temperature during uniaxial tension of AZ31 [16]. The texture components at 90° rotation corresponded to extension twinning and appeared as high intensity contours close to TD. These components strengthened slowly during MUSA process, a result consistent with observation of increased extension twinning. Grain growth also occurred throughout the MUSA process and also contributed to easier twin activation.

[4.4.4]. Effect of microstructure on tensile properties

The poor ductility of H-24 material could be attributed to its strong basal texture that cannot alone accommodate general plastic deformation [15]. In addition, a very high initial dislocation density of rolled microstructure limited its subsequent work hardening in uniaxial tension providing a higher UTS but a significantly lower ductility. Subsequent annealing reduced the dislocation density as well as strength of basal texture to provide some ductility improvement and strength reduction (Figure 4.9). Subjecting the material to post-anneal wire brushing process increased its dislocation content in the surface region (Figure 4.5). The material as a whole gained some additional strength over the annealed material from surface strengthening. However, uniaxial tensile ductility of original material was limited due to limited work hardening capacity of the material and early onset of fracture (see Figure 4.19(a)). On subsequent annealing (i.e., WBA process), the dislocation density was reduced as the material recovered which led to a slight strength reduction as evident in Figure 4.9. The basic mechanisms regarding ductility improvement from grain refinement, role of grain boundaries in promoting uniform deformation and work hardening rate are well understood and documented in the literature for metallic materials [17]. Grain refinement in Mg alloys to the size below 10 μm has been reported to enhance the activation of other slip systems, and specifically prismatic slip around grain boundaries, to enhance uniaxial tensile ductility [18]. Texture spreading as observed on the surface of WBA material (Figure 4.7(c)) could provide favorably oriented grains for activation of different slip systems to increase the strain accommodation capacity of AZ31 sheet and to limit twin-induced strain localization [18]. A reduced grain size also reduces the twin size and minimizes the twin-induced fracture initiation [12]. It has been reported that a modified layer on the surface of WBA materials can inhibit shear band propagation from the surface [13] and thus delay the onset of necking and initiation of fracture. A combined effect of the aforementioned mechanisms (grain refinement, non-basal slip activation, twin and shear band suppression) would likely delay the fracture resulting in ductility enhancement of WBA processed material in the presence of voids (see Figs. 4.9 and 4.19(b)).

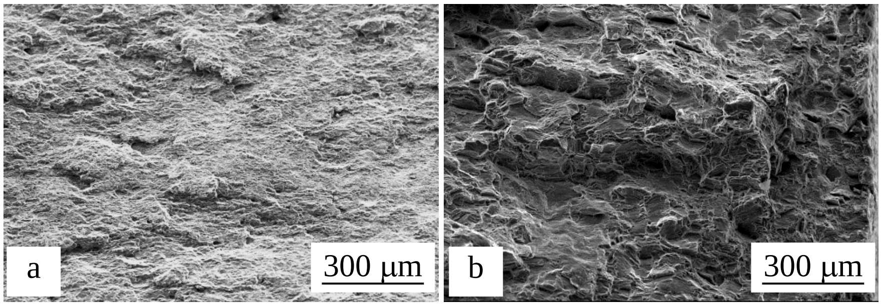

Fig. 4.19. Selected SEM fractographs of: (a) H-24, (b) WBA material.

With respect to WBA-MUSA material, because of its higher initial ductility, it could be subjected to a larger initial pre-strain compared to the Standard-MUSA material, which led to increased texture randomization after first step of annealing, and consequently, to a higher limit strain at the second MUSA step. This had a ‘cascading’ effect for subsequent MUSA steps. A larger portion of grains in the microstructure were subjected to texture reorientation in each step by means of slip and twins compared to the annealed material (Figure 4.14). This resulted in reduced MUSA steps for WBA materials to the desired tensile elongation comparing to the annealed material. Further, a distinctly higher n-value was observed in the earlier MUSA steps for WBA material compared to the annealed material (Figure 4.18(c)). As with the grain size, it is likely that both dislocation and twin hardening played a role in changing the n-value. For WBA material, the fraction of recrystallized grains in each of the MUSA steps was higher compared to the annealed material (Figure 4.16). This provided a lower initial dislocation density at the start of each pre-straining step and thus a higher work hardening rate for WBA-MUSA material which resulted in a larger n-value. The tendency for twin formation, on the other hand, increased with grain growth during MUSA steps, and provided new barriers to dislocation motion thus contributing further to dislocation hardening. The overall impact of aforementioned mechanisms was a reduction in rate of change of dislocation density and consequently the work hardening capacity (or the n-value) in the subsequent MUSA steps for both materials.

[4.5]. Conclusions

[1]. A wire brushing technique based on severe plastic deformation (SPD) of surface using softer brass wire brushes and optimized depth of cut and brushing speed led to formation of a twinned or highly sheared surface layer up to a depth of $30\mu m$ and a smooth polished surface on warm-rolled AZ31 magnesium sheet.

[2]. Wire brushing followed by annealing (WBA) was found to be an effective process for fine surface grain generation and basal texture modification of the warm-rolled AZ31 sheet with superior surface properties.

[3]. WBA processed material showed good surface quality and significant improvement in room temperature uniaxial tensile ductility as a result of grain refinement and texture randomization and could be utilized as a pre-process to extend room temperature forming applications of AZ31 sheet.

[4]. Further enhancement to room temperature cumulative uniaxial tensile ductility of WBA-processed AZ31 sheet was achieved by utilizing a recently proposed multi-step uniaxial stretching and subsequent annealing (MUSA) method [16]. A target uniaxial limit strain (engineering strain) from literature of 0.61 at 400°C from continuous tensile test was achieved in three MUSA steps on WBA processed material whereas the same target could be achieved in four MUSA steps for the Standard-MUSA process with unmodified surface.

[5]. Microstructure and texture development on AZ31 magnesium sheet surface and in the interior as well as its uniaxial stress-strain response was studied for WBA-MUSA and standard-MUSA processes. These studies revealed grain growth, twin formation within larger grains, non-basal texture development and texture spreading, and consequent changes to material work hardening behavior, as a function of number of MUSA steps. Grain size, and texture intensity and spread were significantly increased in the sheet interior and on the surface for both materials. The main mechanisms of texture spreading were observed to be slip-induced and twin-induced texture rotation. In the case of WBA-MUSA material, larger amount of texture spreading was seen at each MUSA step resulting in similar uniaxial tensile ductility to Standard-MUSA material but in fewer steps.

[6]. WBA-MUSA, a new combined sheet pre-processing and subsequent forming process, offers good potential for room temperature industrial sheet stamping applications of AZ31 magnesium sheet.

Acknowledgements

The authors gratefully acknowledge Mr. Robert Kubic of General Motors R&D, Warren, MI, USA, for his help in conducting EBSD and FIB experiments. Also, they would like to thank Ms. Victoria Jarvis of the McMaster Analytical X-ray Diffraction Facility (MAX) Hamilton, Canada for her assistance with the XRD work.

References

[1]. J. A. Del Valle, F. Carreno, O. A. Ruano, Acta Mater. 54 (2006) 4247-4259.
[2]. J. Koike, Metall. Mater. Trans. A, 36A (2005) 1689-1696.
[3]. J. H. Cho, H. W. Kim, S. B. Kang, T. S. Han, Acta Mater. 59 (2011) 5638-5651.
[4]. S. R. Agnew, J. A. Horton, T. M. Lillo, D. W. Brown, Scripta Mater., 50 (2004) 377-381.
[5]. X. Huang, K. Suzuki, A. Watazu, I. Shigematsu, N. Saito, Mater. Sci. Eng. A 488 (2008) 214-220.
[6]. W. Yuan, R. S. Mishra, Mater Sci Eng A 558 (2012) 716-724.
[7]. M. Sato, N. Tsuji, Y. Minamino, Y. Koizumi, Sci. Tech. Adv. Mater. 5 (2004) 145–152.
[8]. H. Kitahara, T. Yada, F. Hashiguchi, M. Tsushida, S. Ando, Surf. Coat. Technol. 243 (2014) 28-33.
[9]. K. Dehghani, M. Nasirizadeh, S. Bagherzadeh, Proc. IMechE, 224 (2010) 190-198.
[10]. Z. Jin, O. Xingbin, Y. Donghua, S. Zhifu, Journal of Wuhan University of Technology-Mater. Sci. Ed. (2009) 515-519.
[11]. H. Q. Sun, Y. N. Shi, M. X. Zhang, K. Lu, Acta Mater. 55 (2007) 975–982.
[12]. M. Habibnejad-korayem, M. K. Jain, R. K. Mishra, Mater. Sci. Eng. A. 619 (2014) 370–377.
[13]. M. Habibnejad-korayem, M. K. Jain, R. K. Mishra, Mater. Sci. Eng. A. 619 (2014) 378-383.
[14]. F. J. Humphreys, M. Hatherly, Recrystallization and Related Annealing Phenomena, second ed., Pergamon Press, Oxford, 2004.

[15]. U. F. H. R. Suhuddin, S. Mironov, Y. S. Sato, H. Kokawa, C. W. Lee, Acta Mater. 57 (2009) 5406–5418.

[26]. S. B. Yi, C. H. J. Davies, H.G. Brokmeier, R. E. Bolmaro, K. U. Kainer, J. Homeyer, Acta Mater. 54 (2006) 549–562.

[17]. G. E. Dieter, Mechanical Metallurgy, McGraw-Hill, United Kingdome, 1988, 186.

[18]. R. K. Mishra, A. K. Gupta, P. R. Rao, A. K. Sachdev, A. M. Kumard, A. A. Luo, Scripta Mater. 59 (2008) 562–565.

Chapter 5

Large deformation of magnesium sheet at room temperature by preform annealing, part II: "bending"

The study reported in this chapter was mostly conducted by this doctoral candidate (Mahdi Habibnejad-korayem) with continuous supervision, over a period of 4 .5 years, by his supervisor, Dr. Jain, and occasional technical advice from Dr. Mishra of General Motors (GM), the industrial sponsor of the project. Some experiments related to texture measurements were assisted by Mr. Kubic of GM as well. The chapter was prepared by this candidate with many discussions of its structure, focus, content, conclusions, language, and writing style with Dr. Jain.

This paper is published in Materials Science & Engineering A619 (2014) 378–383.

Large deformation of magnesium sheet at room temperature by preform annealing, part II: "Bending"

Mahdi Habibnejad-korayem [a], Mukesh K. Jain [a,1], Raja K. Mishra [b]

a McMaster University, Department of Mechanical Engineering, Hamilton, On, Canada L8S4L8
b General Motors Research and Development Center, Warren, MI 48090, USA

Abstract

Automotive magnesium sheets are typically difficult to deform up to large strains at room temperature for stamping applications. This paper is part II of a study to assess the effect of multi-step bending and annealing (MBA) on cumulative bendability of AZ31 magnesium alloy at room temperature. The deformation mechanisms during the MBA process are studied by V-bending and Electron Backscattered Diffraction study. MBA process is shown to improve the cumulative bendability of AZ31 at room temperature by grain refinement and texture modification. The results are also compared with part I of the study where the effect of multi-step uniaxial stretching and annealing is studied on the uniaxial tensile ductility of AZ31 at room temperature.

Keywords: magnesium sheet*; bending; annealing; texture; recrystallization*

[5.1]. Introduction

Bending is an important forming operation in stamping automotive components. Magnesium alloys are new candidates for this, but generally exhibit poor bendability compared to most automotive steel and aluminum sheet materials. As the limited room temperature bendability is due to lack of sufficient slip systems, prior bending and hemming studies on Mg sheets have mostly focused on application of local heating while performing the bending operation [1-3]. However, ability to carry out room temperature bending of Mg sheet is desired to reduce process cost and complexity associated with high temperature bending. In order to improve room temperature formability, grain reorientation and refinement have been proposed [4,5] and many processing methods such as equal channel angular extrusion (ECAE) have been

---

[1] Corresponding author

developed. Since these methods are difficult to implement on a large scale sheet forming application, the feasibility of multi-step forming has been investigated, particularly for low ductility materials which could not be formed in a single continuous operation [6]. Also, the possibility of small radius bending of Mg alloys at room temperature is itself not paid enough attention in literature. The majority of efforts have been focused on understanding the complex twinning behavior [7,8] as well as on anomalous observations of neutral axis shift in Mg materials during bending [9,10]. In general, there is lack of an industrially viable bending technique that is based on microstructure modification at room temperature. Typically, the appearance of localized deformation bands in bending which result in through-thickness instability is the main obstacle to further bending of sheet materials. The present paper employs a multi-step bending and annealing (MBA) method to modify the microstructure and texture of AZ31 Mg sheet and to assess its effect on cumulative bendability. MBA is a process where a specimen is placed in a die and partially bent, and then annealed to eliminate cold work. It is then bent to the final shape using the same die. MBA involves more than one bending and annealing to achieve the final shape.

[5.2]. Experimental procedure

AZ31 magnesium sheets of 1.5 mm thickness in the H24 temper condition were annealed at 400°C for 2 hours and cut along the rolling direction (RD) to 30 mm × 20 mm size coupons. The RD specimens were bent perpendicular to the RD direction at a speed of 2 mm/min in a V-bending jig using a 30° mandrel with a tip-radius of 0.5 mm. MBA, as schematically illustrated in Fig. 5.1, was used to bend the samples.

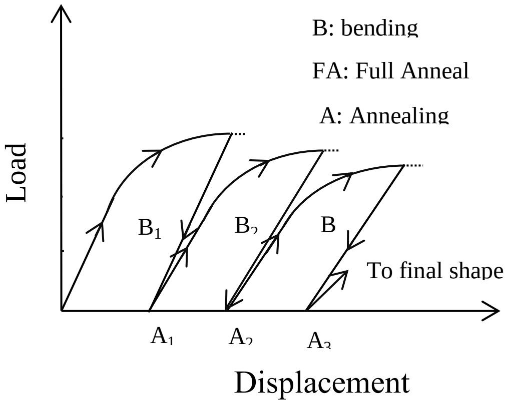

Fig. 5.1. A schematic illustration of multi-step bending and annealing.

The first sample was bent up to fracture at room temperature. The second sample was bent to 90% of the first displacement to fracture followed by annealing at 200˚C for 60 minutes. The specimen was then bent to fracture at room temperature. The same bending and annealing was repeated 2, 3 … 16 times resulting in 3rd, 4th … 17th sample where it was followed by bending to fracture. Specimens for the optical and SEM microscopy studies were prepared by optical metallographic methods of sectioning, polishing and etching. The polishing was done progressively by 9 μm, 3 μm, and 1 μm diamond solutions, followed by 50 nm colloidal silica slurry. The polished samples were etched with picric-acetic acid solution (1 ml acetic acid, 1 ml water, 420 mg picric acid and 7 ml ethanol) for 3 seconds to reveal the grain structure. The microstructural features of MBA were investigated along the LT and ST planes by optical microscopy. In addition, a miniature V-bending test jig was used to perform incremental bending and the surface was observed by placing the test jig with loaded bent sample inside the chamber of Philips 515 SEM. The microstructural features arising from MBA process were then observed along ST and NT planes. The micro-texture was studied by electron backscatter diffraction (EBSD) technique. The samples for the EBSB-based texture studies were prepared by polishing as noted earlier and a quick final etching step (5–10 s) with a solution of 60% ethanol, 20% water, 15% acetic acid and 5% nitric acid. These experiments were conducted using a LEO VP SEM equipped with TSL data acquisition software at an acceleration voltage of 20 keV, with a working distance of 18 mm and a tilt angle of 70˚.

[5.3]. Results and discussion

Fig. 5.2 presents the bending mandrel load versus displacement traces from various samples up to the last step of MBA. The displacement for the first sample (with no preforming) was observed to be significantly larger than the others. A bendability of 2.92 (r_{min}/t value) was achieved (see the embedded table in Fig. 5.2). The bendability was improved by one-step of bending and annealing by decreasing the r_{min}/t value to 2.36 (a lower r_{min}/t value indicates better bendability). The trend in bendability improvement continued with each additional step of MBA leading to the final bendability of 1.07. It is worth noting that the bending of Mg sheet to such a low value of r_{min}/t has been only reported at temperatures higher than 290˚C in single-step bending [11].

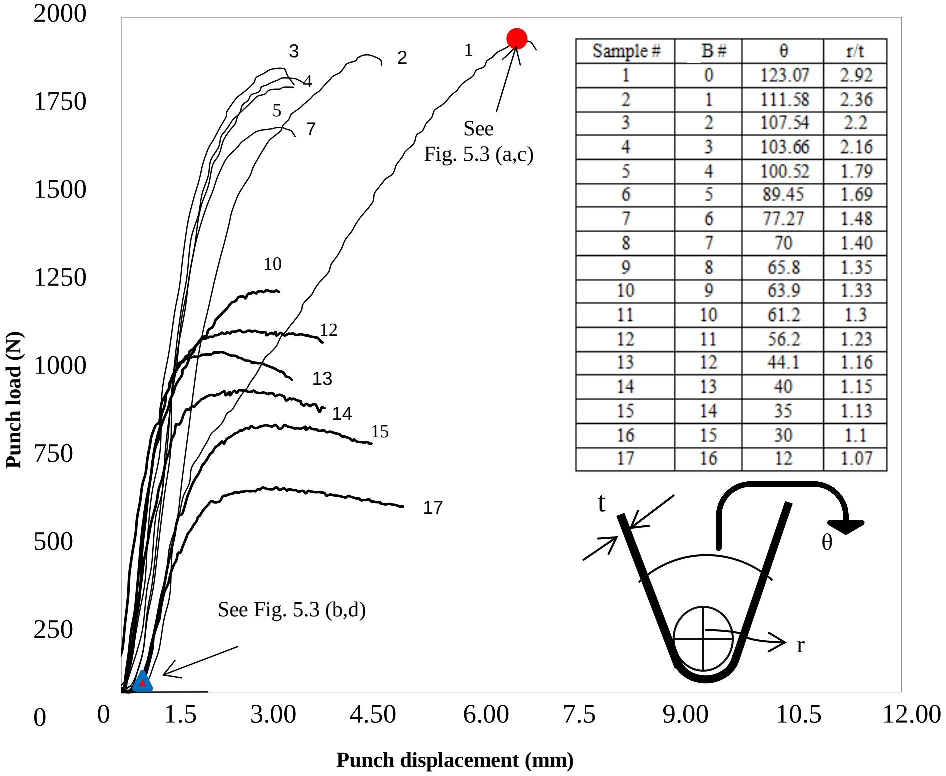

Sample #	B #	θ	r/t
1	0	123.07	2.92
2	1	111.58	2.36
3	2	107.54	2.2
4	3	103.66	2.16
5	4	100.52	1.79
6	5	89.45	1.69
7	6	77.27	1.48
8	7	70	1.40
9	8	65.8	1.35
10	9	63.9	1.33
11	10	61.2	1.3
12	11	56.2	1.23
13	12	44.1	1.16
14	13	40	1.15
15	14	35	1.13
16	15	30	1.1
17	16	12	1.07

Fig. 5.2. Bending mandrel load versus displacement traces, bending angle (θ) and bendability (r_{min}/t) for samples with number of bending steps (1-17).

The through-thickness microstructural modification of bend line during MBA in tensile, neutral and compressive regions is shown in Fig. 5.3. In the tensile region, a large number of deformation bands were introduced by bending (Fig. 5.3 (a)) and the grain size was reduced by annealing (see Fig. 5.3(b)). However, the grain size was gradually increased in the neutral region, as the bending strain was not high enough to promote recrystallization. In the compressive region, however, fewer deformation bands were observed during bending (see Fig. 5.3(c)). The grain size decreased by annealing as shown in Fig. 5.3(d).

The complex microstructure of MBA-bent sheet through the thickness is possibly linked to a through-thickness circumferential strain distribution during bending. As per the simple bending theory [12], the bending strain varies linearly from maximum tensile value at the outside surface to zero at the neutral layer and to maximum compressive value at the inner surface. As with other HCP materials [13], AZ31 shows deformation bands (see Fig. 5.3(a)) to accommodate high strains in the tensile region. The deformation bands develop mostly within the twin bands to accommodate large plastic strains [13]. Large strains could only be provided either by bending steps (such as step 1 and 2) or by strain localization prior to fracture. During annealing, these bands act as nucleation sites for recrystallization [13] and lead to grain refinement in tensile region as shown in Fig. 5.3(b).

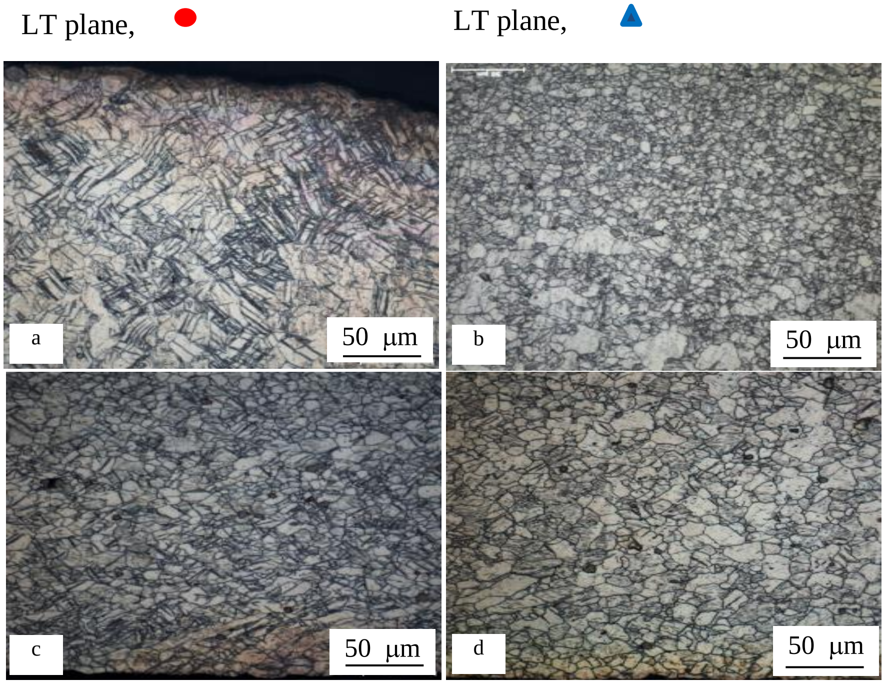

Fig. 5.3. The through thickness micro-structure for (a) B-1 tensile region, (b) MBA-1 tensile region, (c) B-compressive region (d) MBA-1 compressive region.

As discussed by Barnett [14], fine grains result in twin suppression and lead to slip dominated deformation in the subsequent steps of bending. In agreement with the results reported by Baird et al. [7], the strain in compressive region is only large enough to form the twin bands as seen in Fig. 5.3(c). The twin bands initiated from the compressive region in the first step of bending traversed the neutral band to the tensile region, as the bend angle decreased by MBA process (as discussed later when OIM results are presented in Figure 5.6). As the strain was very small in the neutral band region [12], some single twins were also introduced to accommodate the strain in MBA.

Detailed microstructural events of MBA were also observed in a bent specimen in the loaded state in a SEM. The strain accommodation occurred with the subdivision of individual coarse grains into regions of different orientations (see grain 1 in Fig. 5.4(a)). The resulting bands deform on different slip systems, but the lack of enough active slip system at room temperature and limited strain accommodation along the <c> axis [13] forced twining during bending (see Fig. 5.4(b)). The twins were restricted in length by grain boundaries of coarse grains, but in the large strain areas of tension and compression regions, they transcended to the neighboring grains across grain boundaries. This resulted in formation of twin bands (shown by white arrows in Fig. 5.4(c)) because of good strain compatibility between twins and the c-axis of grains [6]. As noted by Humphreys et al. [13], limited twinning shear can lead to more energetically favorable shear bands to accommodate the larger strains (see Fig. 5.4(c)). The shear bands first initiated at the grain level (see Fig. 5.4(b)) and then organized into macroscopic bands traversing several grains in the neighborhood of twin bands. The shear bands were mostly observed towards the end of each forming step [13] leading to plastic instability and a conspicuous drop in bending load (see Fig. 5.2). The drop was likely due to micro-cracks formation at intensified shear bands (Fig. 5.4(d, e)). Therefore, pre-bending values were selected in a manner to avoid micro-cracks, but some of them initiated earlier than load drop and were impossible to avoid (see Fig. 5.4(g)). Accumulation of the early formed micro-cracks in MBA could result in loss of formability, but annealing facilitated grain refinement in the neighborhood of micro-cracks. The grain refinement which is mostly observed in the tensile region (Fig. 5.4(f)) led to grain boundary strengthening in the damaged area and helped in regaining the formability. An example of this is shown in Fig. 5.4(h) where the grains were locally refined from 9.5 μm to 1.5 μm. The regions previously occupied by twin bands were also found vulnerable for micro-crack initiation. This source of micro-crack formation was also subjected to some grain refinement during annealing (Fig. 5.4(i)) and could also help neutralize the negative effect of micro-cracks during bending, as the post-instability displacement remained constant from steps 3 to 7 but increased from steps 13 to 17 (see Fig. 5.2). The grain refinement in the vicinity of micro-cracks, as shown in Fig. 5.4(d, e, h), is in contrast with our observation in multi-step uniaxial stretching and annealing (MUSA) of AZ31 sheet [15]. The twin-induced micro-crack formation and the cross-sectional thinning that followed in MUSA could not be suppressed by grain refinement in the cracked area. The difference between MBA and MUSA is due to the more severe mechanical constraint for the former process arising from the plane strain condition in bending compared to the uniaxial tension. The stored energy seems large enough to provide the required driving force for recrystallization in MBA leading to significant grain refinement in the micro-cracked region (see Fig. 5.4(g,h)). Microstructural observations in magnesium alloys by Nemko et al. [16] suggest that the void linkage has a larger influence on failure strain than the voids morphology. Therefore, modification of the microstructure by grain refinement in the inter-void region in MBA could possibly retard void coalescence into fracture. It is also to be noted that the gradual grain coarsening (from 10 to 35 μm) on the neutral plane did not significantly affect the bendability, as the neutral layer was subjected to small strains in bending [12].

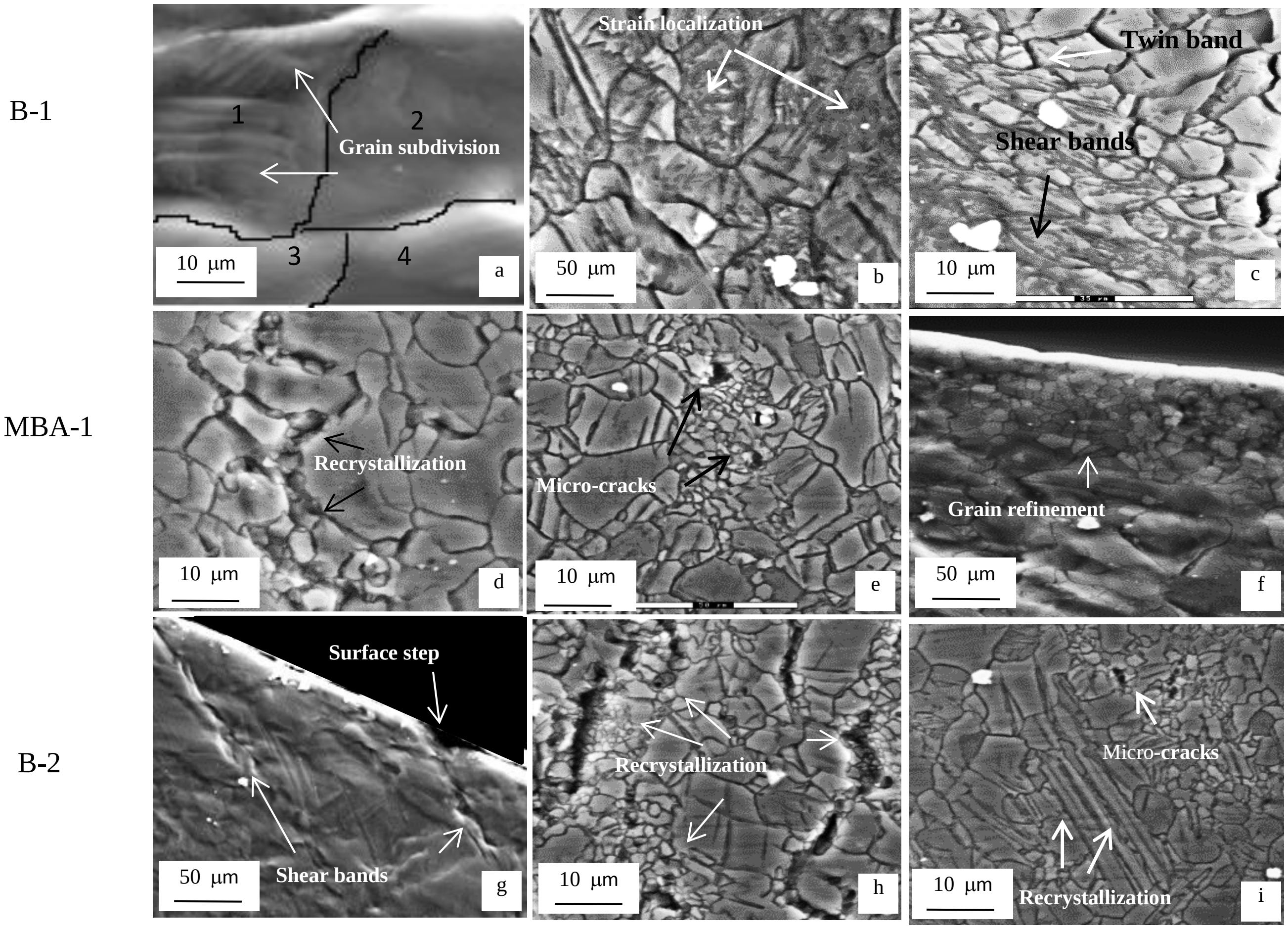

Fig. 5.4. SEM observations from the bent specimen for (a-c) B-1 on LT plane, (d-f) MBA-1 on ND plane and (g-i) B-2 on ND plane.

The texture of annealed AZ31 sheet (strong (0001) basal texture with the intensity of 10.0 from EBSD analysis) was modified differently by the MBA process through the thickness (i.e., at the top, middle and bottom regions along LT plane), as shown in Fig. 5.5. The bending influenced the texture by changing the pole intensity and randomization. The maximum intensity of grains in the annealed material having basal poles was increased slightly in compression and tension regions by bending (see Fig. 5.5(a,b)) and decreased by annealing (see Fig. 5.5(c,d)). It could be ascribed to the lower critical resolved shear stress (CRSS) value at room temperature for basal plane compared to other crystallographic planes [17]. A larger maximum intensity in the first bending step is likely from the larger strain that is imposed on the material in this step compared to the subsequent steps. Although bending was not as effective in randomizing the pole distribution in tensile part, a small tilt was observed in the texture of compressive and neutral regions by first bending leading to a larger rotation of the texture in the second step. The bimodal distribution of poles in Fig. 5.5(e, f) is induced by the twin bands and their movement from bottom region to center line during bending [7]. The additional bending in the second step was required to extend the previously formed twins to consume the entire grains and form a complete 90˚ tilt of the poles distribution. In the mid-thickness region, annealing removed the bimodal pole distributions that resulted from bending, as shown in Fig. 5.5(g,h). As reported by Levinson et al. [18], it could be ascribed to negligible contribution of recrystallization on contraction and extension twins in the final texture. This, however, is in contrast with the observation in compressive region where bending led to stronger bimodal distribution (see Fig. 5.5(i, j) that remained unaffected by annealing (see Fig. 5.5(k, l)). Development of new texture components in compressive region with angle of about 36˚ indicates that the recrystallized grains originated from twin bands. These grains grew rapidly to consume the remaining deformed microstructure and influence the final texture [14]. Annealing also helped texture randomization by weakening the maximum intensity. The annealed texture was found to have some common components with the deformed texture, but with a larger drop in the maximum intensity in the tensile and compressive regions. The texture, however, remained largely unaffected in the vicinity of the neutral plane perhaps due to smaller strains in this area during bending. Annealing was also effective in changing the texture of tensile and compressive regions by recrystallization at the shear and twin bands [13]. In the tensile part, grain size reduction suppressed the twining and led to non-basal slip activation during bending [14]. The gradual texture randomization in tensile part conforms well to the texture randomization by MUSA process which is discussed in detail in the companion paper [15]. However, the maximum intensity was higher for MUSA for the same annealing condition due to grain coarsening.

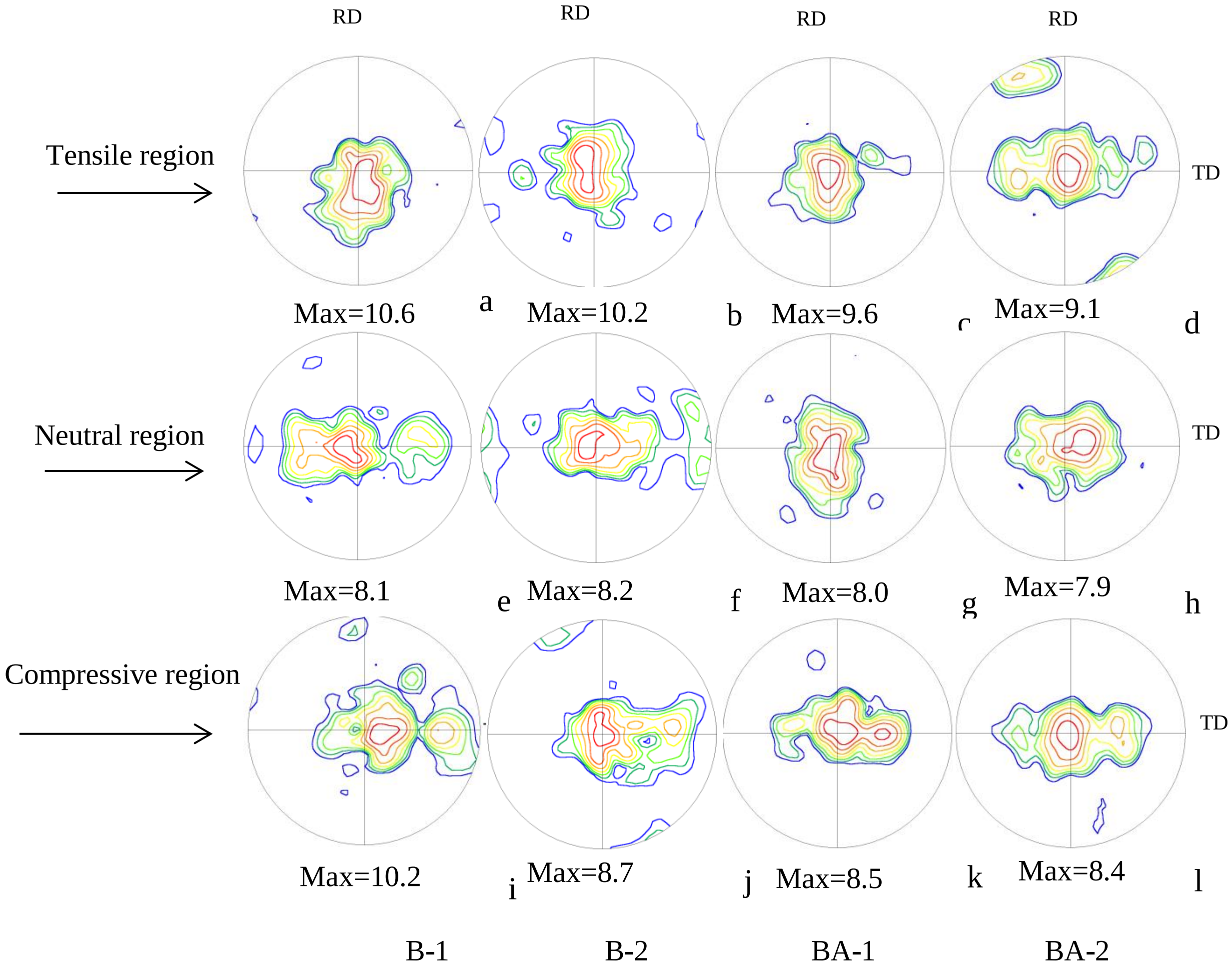

Fig. 5.5 The through thickness micro-texture of bend (B-1, 2) and annealed (MBA-1, 2) materials by (0001) pole figure (PF) for the top, middle and bottom regions of bend line.

The increase in the number of twins, as shown in EBSD micrographs of the neutral region in Fig. 5.6 (a,b), confirms the twin band movement from the compressive side towards the neutral region. Misorientation analysis from Fig. 5.6(c,d) showed a large fraction of grains with the misorientation angle of extension twins $\{10\bar{1}2\}<10\bar{1}\bar{1}>$ of 86˚ and a smaller fraction of grains with the misorientation angle of double twins $\{10\bar{1}1\}<10\bar{1}2>$ of 36 ˚ on the twin bands. Double twins, however, were not reported by [7], perhaps because they are rather difficult to detect by EBSD due to their narrow width.

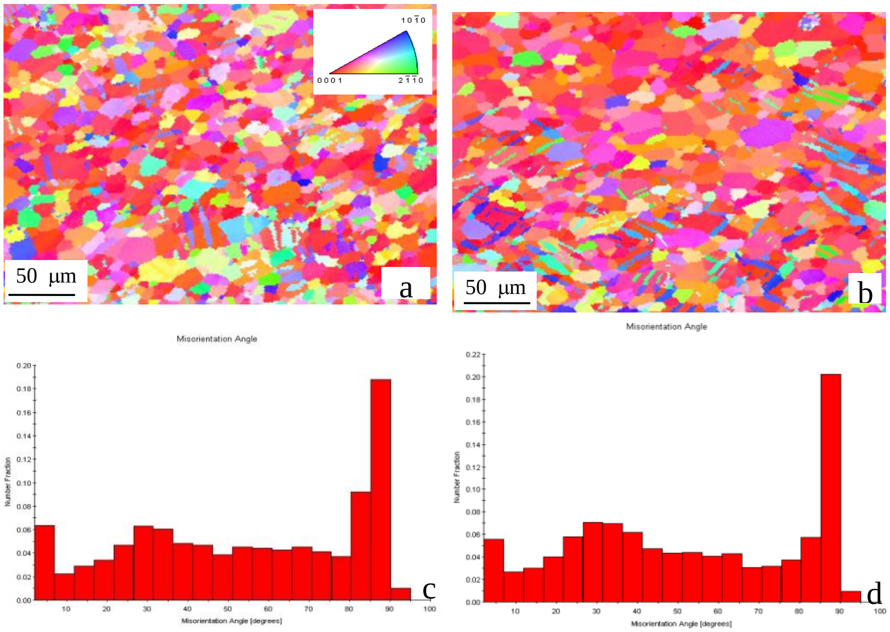

Fig. 5.6. EBSD micrographs showing the grain structure of neutral region in (a) B-1, (b) B-2, (c) the corresponding misoreintation angle for the neutral region of B-I, (d) the corresponding misoreintation angle for the neutral region of B-II.

In general, a comparison of MBA (tensile region) with MUSA indicates that the texture intensity and average grain size decreases by MBA whereas the post-instability displacement increases. This clearly indicates the effectiveness of MBA over MUSA and provides evidence as to why AZ31 could be deformed to large strain without any limitation in the MBA process. The improvement in cumulative bending could be attributed to microstructure and texture modification during MBA, whereas texture modification largely contributed to ductility improvement during MUSA [15].

[5.4]. Conclusions

In summary, MBA was found as a feasible forming technique to bend AZ31 to large strains at room temperature. Extensive deformation bands that formed in bending were replaced by new grains during annealing. The bending and subsequent annealing also promoted the local modification of the microstructure to regain some of the lost formability in the damaged areas. The grain size, especially in the micro-cracked regions, was reduced and the texture was modified by MBA. The MBA process resulted in more pronounced local grain refinement and texture weakening in the highly strained tensile region compared to MUSA.

Acknowledgments

The authors would like to thank Mr. Robert Kubic of GM R&D Center in Warren, MI, USA for his assistance with the EBSD work.

References

[1] J. Carsley, S. Kim, J. Mater. Eng. Perform., 16 (2007) 331-338.

[2] J. Carsley, Proc. Tools Mater. Sci. Tech., (2009) 20-25.

[3] A. A. Luo, K. A. Sachdev, Mater. Sci. Forum, 488-489 (2005) 477-482.

[4] S. Biswas, D. Kim, S. Suwas, Mater. Sci. Eng. A 550 (2012) 19–30.

[5] F. Z. Hassani, M. Ketabchi, Mater. Sci. Eng. A 528 (2011) 6426–6431.

[6] T. Lee, S. Hartfield-Wünsch, S. Xu, SAE Technical Paper, (2006), doi:10.4271/2006-01-0987.

[7] J. C. Baird, B. Li, S. Yazdan Parast, S. J. Horstemeyer, L. G. Hector Jr., P. T. Wang, M. F. Horstemeyer, Scripta Mater., 67 (2012) 471-475.

[8] I. Sato, S. Miura, T. Mohri, Mater. Sci. Forum, 654-656 (2010) 715-718.

[9] M. M. Avedesian, H. Baker, Magnesium and Magnesium Alloys, ASM International, Materials Park, OH, 1999.

[10] A. Ben-Artzy, L.G. Hector Jr., P. E. Krajewski, in: S.R. Agnew, N. R. Neelameggham, E. A. Nyberg, W. H. Sillekens (Eds.), Magnesium Technology, TMS, Warrendale, PA, (2010), 69-74.

[11] E. F. Emley: Principles of Magnesium Technology, first edition, Pergamon Press, 1966, P. 193.

[12] Z. Marciniak, J.L. Duncan, S.J. Hu, Mechanics of Sheet Metal Forming, Butterworth-Heinemann, 2002, P. 83.

[13] F. J. Humphreys, M. Hatherly, "Recrystallization and Related Annealing Phenomena", second ed, Elsevier Ltd., Oxford, 2004, P. 184.

[14] M. R. Barnett, Scripta Mater. 59 (2008) 696–698.

[15] M. Habibnejad-korayem, M. K. Jain, R. K. Mishra, to be submitted to Mater. Sci. Eng. A. 619 (2014) 370-377.

[16] M. J. Nemcko, D. S. Wilkinson, Magnesium Technology, TMS, San Diego, (2014), 33-37.

[17] M. R. Barnett, S. Jacob, B. F. Gerard, J.G. Mullins, Scripta Mater., 59 (2008) 1035-1038.

[18] A. Levinson, R. K. Mishra, R. D. Doherty, S. R. Kalidindi, Acta Mater., 61 (2013) 5966-5978.

Chapter 6

Microstructure modification and bendability improvement of AZ31 magnesium sheet by bending-unbending and annealing process

The study reported in this chapter was mostly conducted by this doctoral candidate (Mahdi Habibnejad-korayem) with continuous supervision, over a period of 4 .5 years, by his supervisor, Dr. Jain, and occasional technical advice from Dr. Mishra of General Motors (GM), the industrial sponsor of the project. Some experiments related to texture measurements were assisted by Mr. Kubic of GM as well. The chapter was prepared by this candidate with many discussions of its structure, focus, content, conclusions, language, and writing style with Dr. Jain. This paper has been accepted for publication in Materials Science and Engineering A (doi: 10.1016/j.msea.2015.09.047).

Microstructure modification and bendability improvement of AZ31 magnesium sheet by bending-unbending and annealing process

Mahdi Habibnejad-korayem [a,1], Mukesh K. Jain [a], Raja. K. Mishra [b]

a McMaster University, Department of Mechanical Engineering, Hamilton, ON, Canada L8S4L8

b General Motors Research and Development Center, Warren, MI 48090, USA

Abstract

AZ31 magnesium sheet was processed by room temperature multi-step cyclic bending-unbending (CBU) and subsequent annealing (CBUA) process to modify the microstructure and improve its bendability. The CBU process resulted in a complex stress and strain distribution through the thickness and a multi-layered microstructure after annealing. The grain structure, micro-texture, and micro-hardness of each of the layers were studied by optical microscopy, electron back-scattered diffraction (EBSD) and indentation measurements, respectively. The CBUA process resulted in static recrystallization of grains leading to average grain size of about 2.5 μm to a depth of about 40 μm from the surface. The grain size, however, significantly coarsened in two intermediate layers through the thickness. The recrystallization was studied by microstructural characterization and micro-hardness measurement after annealing. The through-thickness texture from EBSD experiments indicated texture spreading and weakening in the surface layers. The results are consistent with the mechanics of cyclic bending-unbending (CBU) process, mechanisms of strain induced static recrystallization, texture evolution and its stability with long term annealing. The grain refinement and texture spreading of multi-layered microstructure from CBUA process led to bendability (r_{min}/t value) improvement in V-bending tests at room temperature.

Keywords: AZ31; annealing; texture; microstructure; bendability

---

[1] Corresponding author

[6.1]. Introduction

Use of magnesium sheet material in automotive body panel applications has the potential to reduce vehicle weight and consequently fuel consumption and greenhouse gas emission. However, such usage is limited because of poor room temperature formability, and specifically bendability of commercially available magnesium alloy sheets in processes involving sharp bends such as hemming. Considerable global effort is being made to overcome this problem by modifying the microstructure and crystallographic texture of Mg alloys as well as by pre-heating blanks before hemming. A number of thermo-mechanical processing techniques have been explored over the years for grain refinement to enhance the mechanical property and formability of AZ31 sheet material. These processing techniques include equal channel angular pressing (ECAP), equal channel angular extrusion (ECAE), friction stir welding (FSW), accumulative roll bonding (ARB) and equal channel angular rolling (ECAR) to name a few [1-5]. However, many of these processes are rather difficult to apply on a commercial scale for large scale grain refinement of wide sheets. Therefore, multi-step bending and unbending process such as that encountered in roller leveling in industrial sheet production lines is potentially one of the more practical methods. A similar process of repeated unidirectional bending (RUB), based on pulling sheet material on a cylindrical support, resulted in improved room temperature tensile ductility and drawability of AZ31 by texture modification [6,7]. Another similar process of hot cyclic bending (HCB) has been also used to refine the grain size of Mg alloys [8, 9]. In this process, AZ61 is subjected to cyclic bending at relatively high temperatures for successive passes without reheating (or straightening) between the bending passes. The processed material, when water quenched, shows better tensile ductility due to grain size reduction and texture modification. These studies are, however, focused only on uniaxial tensile ductility improvement by multiple bending of Mg alloys. In general, there have been very few studies on improving bendability of magnesium sheet materials [10-14]. The focus of the bending studies in the past has been mostly on warm bending of magnesium alloys. In one study, bending behavior of AZ31 at an elevated temperature of 270° C was investigated for application to hemming of automotive closure panels where a complex pattern of grain structure through the thickness was noted [10]. In another study, local heat was applied in the bend region using laser beam to complete the hem without causing thermal distortion of the panel [11]. In two other separate studies, a temperature range of

150-200°C was employed to study bending of AZ31 tubes and profiles [12, 13]. A multi-step bending and annealing process was recently studied by the present authors to improve room temperature bendability of AZ31 sheet [14].

The present work is an attempt to explore the potential of multi-step cyclic bending–unbending process at room temperature as an alternative to more expensive high temperature bending or discontinuous multi-step bending with pre-strain annealing [14]. This work explores a cyclic bending-unbending and annealing (CBUA) process to modify the grain structure and texture of commercial grade AZ31 sheet. The deformation is carried out at room temperature and is assisted by intermediate annealing. The mechanics of CBU process as well as microstructures after CBU and CBUA processes in terms of grain size and texture evolution through the sheet thickness are studied. The effect of microstructure modification by CBUA process on subsequent room temperature monotonic bendability of AZ31 is also investigated.

[6.2]. Experimental procedure

[6.2.1]. Materials and processing

AZ31 magnesium sheets of 1.5 mm thickness in the H24 temper condition were annealed at 400°C for 2 hours and cut to long and narrow strips of size 400 mm × 38 mm along the rolling direction (RD). The strips were deformed by cyclic bending-unbending (CBU) process at room temperature using a set of three fixed cylindrical and parallel rolls of diameter 10 mm in a rigid roll housing, while the two end rolls (1 and 3) were fixed and the middle roll (2) could be adjusted by moving horizontally in and out of the space between rolls 1 and 3 to create a desired offset, as shown in Fig. 6.1(a,b). The bending-unbending device used in this study for CBU process was similar to the so-called draw-bead simulator typically used to measure the coefficient of friction at the tool-sheet interface in sheet materials. AZ31 strip sample was first introduced through a top port in the roll housing and through the set of 3-rolls to emerge from a bottom port. The bottom end of the strip was clamped with a grip attached to a long-stroke hydraulic actuator located directly below the rolls while the top end of the strip above the top roll was kept free. The middle roll was then moved towards the strip to contact and bend the strip until a middle roll offset of 7 mm was achieved. The strip sample was then pulled through the rolls at a speed of 10 mm/sec. The strip was turned sideways (i.e., rotated about its longitudinal axis by 180°) and reintroduced into the 3-roll device after each pass for a total of 3 passes. The entire process is referred as CBU-I in the following sections. This sample was then furnace annealed in air at 400°C for 30 seconds to obtain CBUA-I sample. The 3-pass process was then continued on CBUA-I sample for the second time to make CBU-II sample. The sample was then annealed at 400°C for 30 seconds to obtain a CBUA-II sample. Repeating the 3-pass process on CBUA-II sample resulted in CBU-III sample which on annealing provided a CBUA-III sample. The motivation for carrying out processing steps from CBU-I to CBUA-III was to gradually modify the microstructure by introducing large bending strains in smaller increments in the material without causing failure of the specimen.

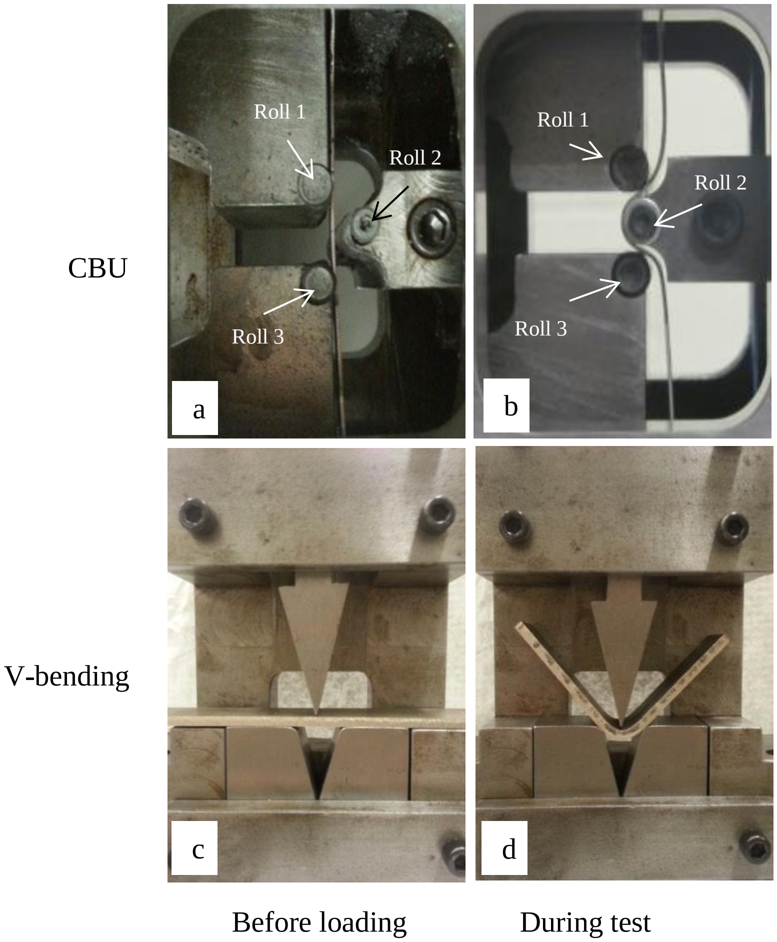

Fig. 6.1. Test configurations for (a) bending-unbending device before loading in CBU process, (b) bending-unbending device during CBU process, (c) V-bending punch and die before test, (d) V-bending punch and die during test.

[6.2.2]. Microstructural characterization

Specimens for microstructure study were prepared by sectioning, polishing and chemical etching. The polishing was done by 9 μm, 3 μm, and 1 μm size diamond particle suspensions, followed by 50 nm colloidal silica slurry. The polished samples were etched with picric acetic solution (1 ml acetic acid, 1 ml water, 420 mg picric acid, and 7 ml ethanol) for 3 seconds to reveal the grain structure. Average grain size was measured from optical micrographs by the grain count method in which an average grain size could be obtained from measurements of the number of grains per unit area on a polished surface. Since a wide range of grain sizes resulted from CBUA process, different image magnifications with values of 1000X, 200X and 50X were utilized. Samples for texture study were polished and etched as above, but given a final short etch (5–10 seconds) with a solution of 60% ethanol, 20% water, 15% acetic acid, and 5% nitric acid [15]. Crystallographic texture was obtained by EBSD experiments using an SEM (model LEO 438VP) at an acceleration voltage of 20 kV, a working distance of 18 mm, and a tilt angle of 70˚. The EBSD data was analyzed with commercial TSL® software. The data collection was carried out on ST plane in a window size of 1500 μm × 400 μm, and, for pole figures and OIM maps representation, projected onto ND plane with a 90˚ rotation about TD (transverse direction) axis to be consistent with the results for Mg sheets in the literature. All EBSD maps in this paper are presented for data points with a confidence index (CI) of 0.1 or higher and image qualities (IQ) of higher than 150. This value was obtained from fully recrystallized AZ31 in this study and it represents the minimum value for capturing the mis-orientation pattern in deformed grains. The grains with CI and IQ values below 0.1 and 150 were considered deformed and those with values of 0.1 and 150 or higher were considered deformation free.

[6.2.3]. Mechanical testing

Test strips in H-24, annealed, CBU-III and CBUA-III processed conditions were cut along the transverse direction (TD) to 30 mm × 20 mm size test coupons which were then bent in a V-bending jig (see Figure 6.1(c,d)) mounted on a computer controlled servo-hydraulic mechanical test system (MTS, model # 312.31). All tests were conducted at a speed of 2 mm/min using a sharp mandrel with an included bend angle of 30° and a tip-radius of 0.5 mm while keeping the bend line parallel to the rolling direction. The bendability values were calculated from photographs in the unloaded state by measuring the radius of the smallest fitted circle (r_{min}) in the bent area and dividing it by the initial sheet thickness (t).

Uniaxial tensile and compressive behavior of annealed AZ31 at room temperature was also determined using the above mechanical testing equipment. The samples were annealed at 400˚C for 2 hrs. The tensile tests were conducted according to ASTM standard (10.1520/B0557M-14) on machined samples of gauge width 10 mm and gauge length 100 mm along the rolling direction (RD) using a clip-on extensometer to control the strain rate. Uniaxial compression tests were carried out at the same initial strain rate as in tension on a rectangular parallelepiped coupon of 8 mm × 8 mm × 11 mm length, width and height respectively. The coupons were machined from a thicker AZ31 sheet with the same texture as the thinner sheet and compressed to fracture. Teflon films were used as a lubricant to reduce the friction at the die-test piece interface.

Vickers micro-indentations were made across the thickness of the polished sheet specimens using a pyramidal indenter to obtain through-thickness micro-hardness profiles after CBU and CBUA processing as well as after V-bending. For this purpose, an indention load of 25 gf for a dwell time of 15 seconds was utilized.

[6.3]. Results

[6.3.1]. Microstructural changes

Through-thickness microstructure of as-received (H-24) and annealed materials are presented in Fig. 6.2(a,b). As-received material exhibited deformed grains arising from the rolling process (Fig. 6.2(a)). The initial annealing at 400˚C for 2 hours completely recrystallized the as-received microstructure and resulted in a uniform grain structure with an average grain size of about 9.5 μm (Fig. 6.2(b)).

H-24 Annealed

Fig. 6.2. Through thickness micrographs of AZ31 in (a) H-24 and (b) annealed conditions.

A layered grain structure through the sample thickness resulted from CBU-I process as shown in Fig. 6.3(a) where thickness dimension is being shown horizontally across the various optical micrographs from one surface to another. The grain structure for CBU-I and II materials, when observed at larger magnifications, exhibited a large number of twins in the outer surface layers A and E and a significantly small number in less-distinct mid-thickness layers B, C and D (see Figure 6.3(a,b)). In the case of CBU-III, however, significant grain coarsening was observed in layers B and D as shown in Figure 6.3(c) where larger fractions of twins in layers A, B, D and E and a small fraction in layer C were observed.

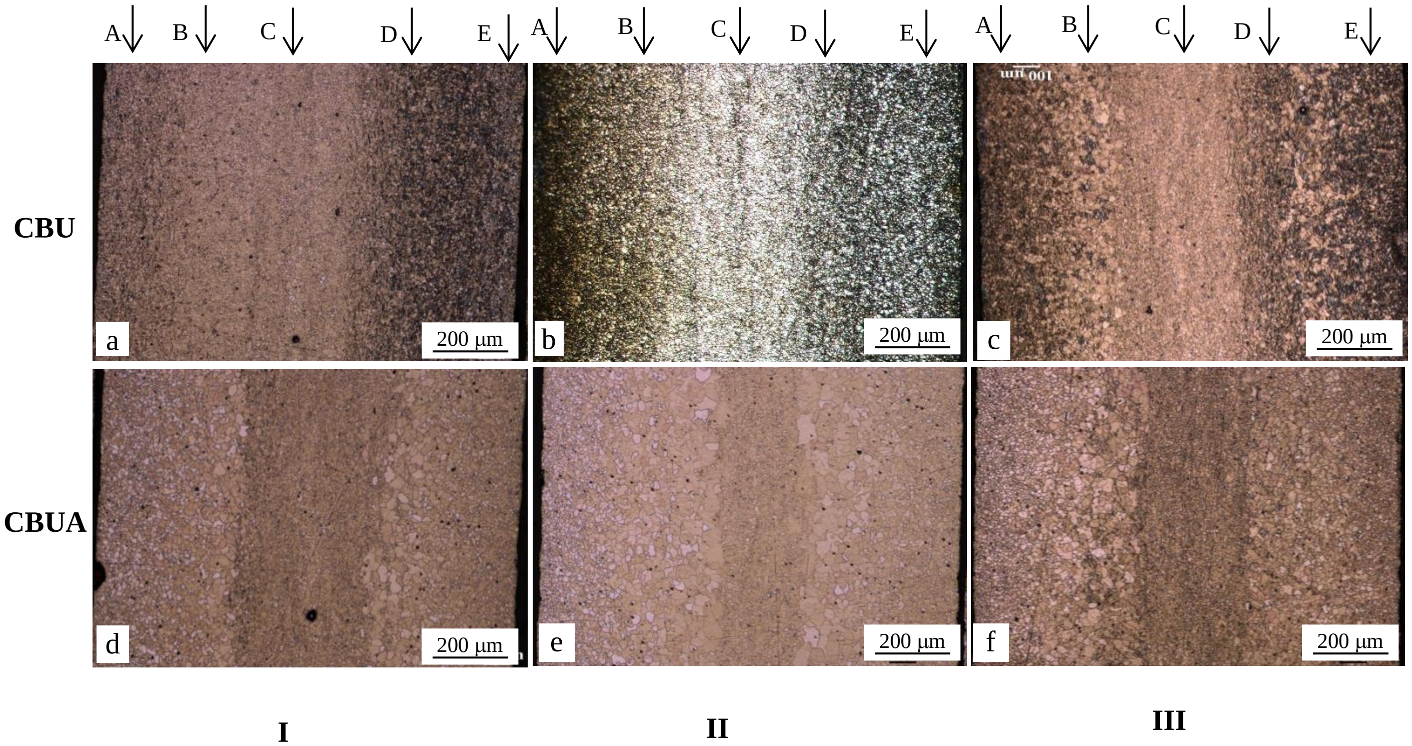

Fig. 6.3. Optical micrographs showing the microstructure of AZ31 deformed by (a) CBU-I, (b) CBU-II, (c) CBU-III, (d) CBUA-I, (e) CBUA-II and (f) CBUA-III.

Annealing the CBU processed materials resulted in a 5-layer microstructure through the sheet thickness, as shown in Fig. 6.3(d-f)). In all of CBUA processed materials, the grains were refined close to the surfaces and coarsened adjacent to these two refined layers. In the mid-thickness region, however, the grain size was similar to the original as-received material. For the case of CBUA-III, two surface layers were refined to an average grain size of about 2.5 μm and to the depth of 40 μm. The coarse-grained layers B and D exhibited an average grain size of 25 μm in layer B and 30 μm in layer D with a thickness of 200 μm in each of the two layers. Also, a further transition with a rather sharp boundary was observed from the coarse grained layers B and D to the mid-thickness layer C. The mid-thickness layer had an average grain size of 9.5 μm similar to the original as-received material (H-24) with a thickness of about 500 μm.

Fig. 6.4(a,b) shows higher magnification optical micrographs from fine and coarse grained layers A and B respectively for CBU-III processed material where a large fraction of twined grains can be observed. Most of the twins are visible as dark lines across the grains whereas twin free grains appear in a lighter grey.

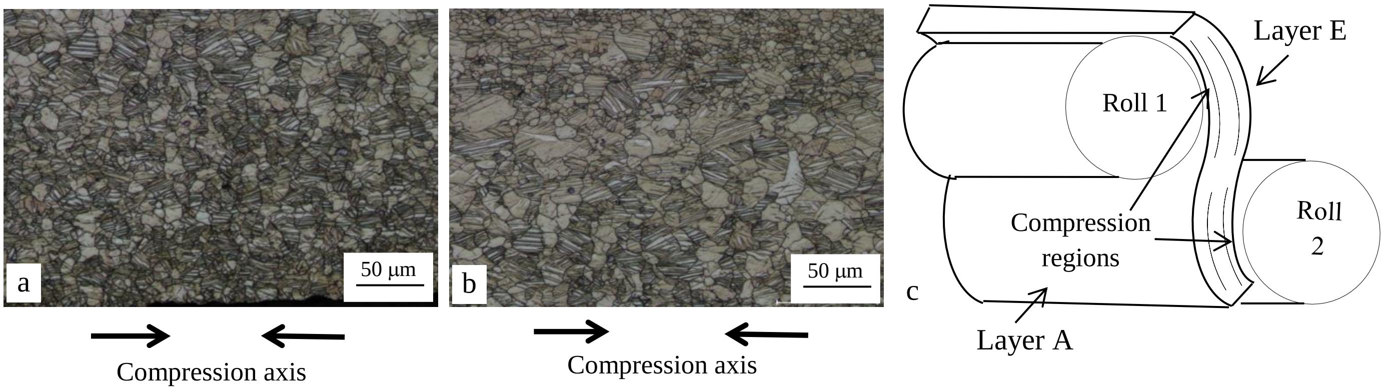

Fig. 6.4. Optical micrographs showing the microstructure of AZ31 deformed by CBU-III process in (a) region A, (b) region B and (c) a schematic of CBU process showing the compression regions.

Grains undergo compression during the cyclic bending-unbending process as shown with black arrows for regions A and B in Figure 6.4(a,b). A schematic of a multi-layered CBU specimen indicating compressive deformation region is presented in Figure 6.4(c). Compressive regions A and B cause the grains in them to elongate in the through-thickness direction (vertical in the two micrographs). The amount of compression and twin density appeared larger in surface layer A. SEM micrographs of layer D from ST plane of CBUA processed materials are shown in Fig. 6.5 where a gradual increase in the number of fine grains was observed over the three CBUA processes. The average grain size in layer A was reduced from 9.5 μm for CBUA-I to 5.2 and 2.5 μm for CBUA-II and III, respectively. It is to be noted that CBUA-II and CBUA-III microstructures in Figs. 6.5(b,c) also exhibit evidence of twins remaining after annealing, as shown by white arrows.

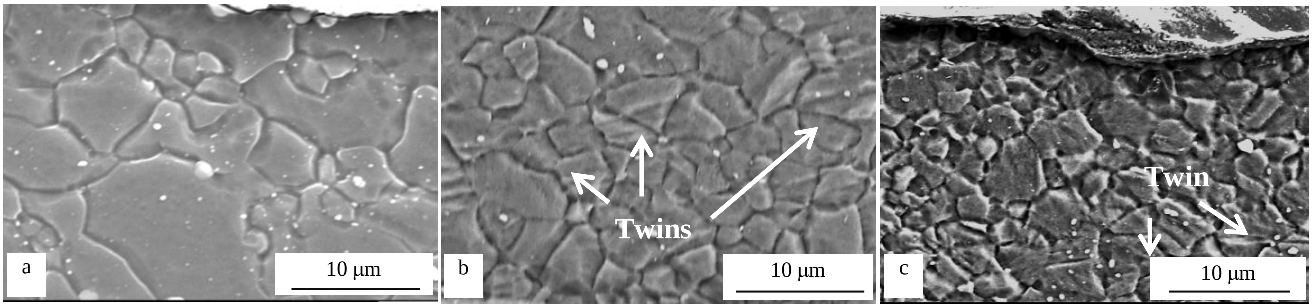

Fig. 6.5. SEM micrographs of the layer A on ST plane after (a) CBUA-I, (b) CBUA-II and (c) CBUA-III.

Strength reduction from annealing was assessed by conducting micro-hardness measurements on each of the through-thickness layers. Micro-hardness indents were made on etched samples so that location of each indent and corresponding layer could be readily identified. CBU samples were annealed at 400˚C for a range of times, namely, 0, 5, 10, 15, 30, 45, 60, 300, 600, 900 and 1800 seconds and tested in triplicates. Resulting micro-hardness versus annealing time plots are presented in Figure 6.6 where micro-hardness variation in repeat tests was within a band of ±3%.

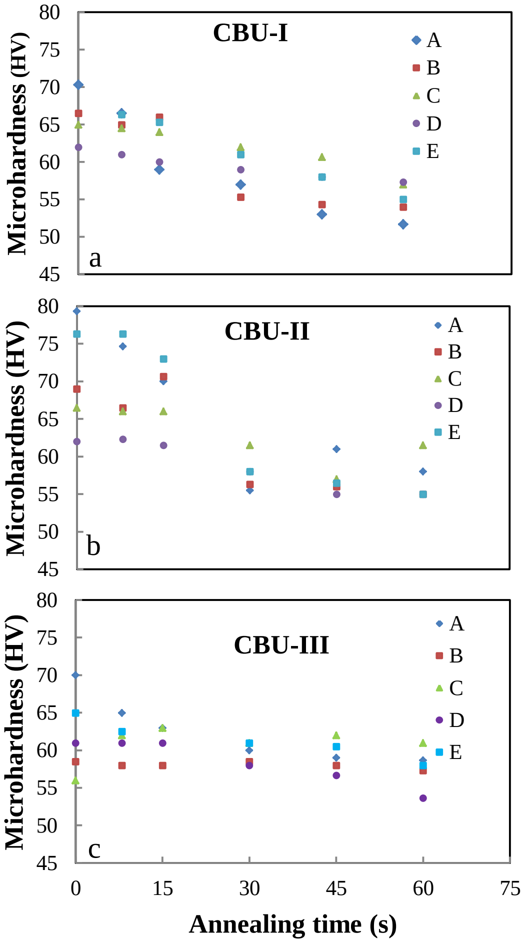

Fig. 6.6. Strength softening during annealing at different times for (a) CBU-I, (b) CBU-II and (c) CBU-III processed materials.

The results are shown for the first 60 seconds of annealing. It is to be noted that no significant change was observed in the hardness values at annealing times longer than 60 seconds. As shown in this figure, the softening starts almost immediately and ends after 45 seconds in layers A and

E. The rate of softening, in contrast, was very small for layers B and D and almost no softening was observed for mid-thickness layer C. In addition to micro-hardness, grain size changes for each microstructural layer were also measured in the annealing experiments. These were done using two separate micrographs from each layer resulting in a scatter in average grain size for each layer of about ±5%. Grain refinement occurred primarily in the surface layers A and E in the early stages of annealing as indicated in Fig. 6.7(a-e). Continued annealing of all CBU-processed materials, however, coarsened the grain size in these layers till the original grain size of 10 μm was regained. In contrast, significant grain coarsening on annealing from the start was observed in layers B and D. The grain size remained largely unchanged in region C during annealing and, in fact, layer C disappeared altogether for CBU-II and CBU-III materials after annealing times of 900 and 300 seconds respectively (see Figure 6.7(c)). Average thickness values in each of the microstructural layers (an average of three reading with a scatter of ±5%) as a function of annealing time are shown in Fig. 6.7 (f-j). For all CBUA processed materials, the surface layers appeared after 10 seconds of annealing with a thickness of about 150 μm. The thickness of layers A and E increased rapidly to 350 μm in the first 45 seconds of annealing and remained constant during the rest of annealing, although only about 40 μm of the thickness possessed refined grains. The thicknesses of these layers were generally observed to be lower in CBUA-III than the other two CBUA processes. Layers B and D also appeared through the thickness after 10 seconds of annealing resulting in a thickness of 200 μm. These layers thickened in CBUA-I process at the expense of layer C until the disappearance of layer C. In CBUA-II and III materials, thickness of layers B and D increased gradually until these two layers merged together which occurred after 900 and 300 seconds during CBUA-II and III, respectively. Mid-layer thickness, in contrast, reduced continuously during CBUA-II and III till this layer disappeared entirely from the microstructure.

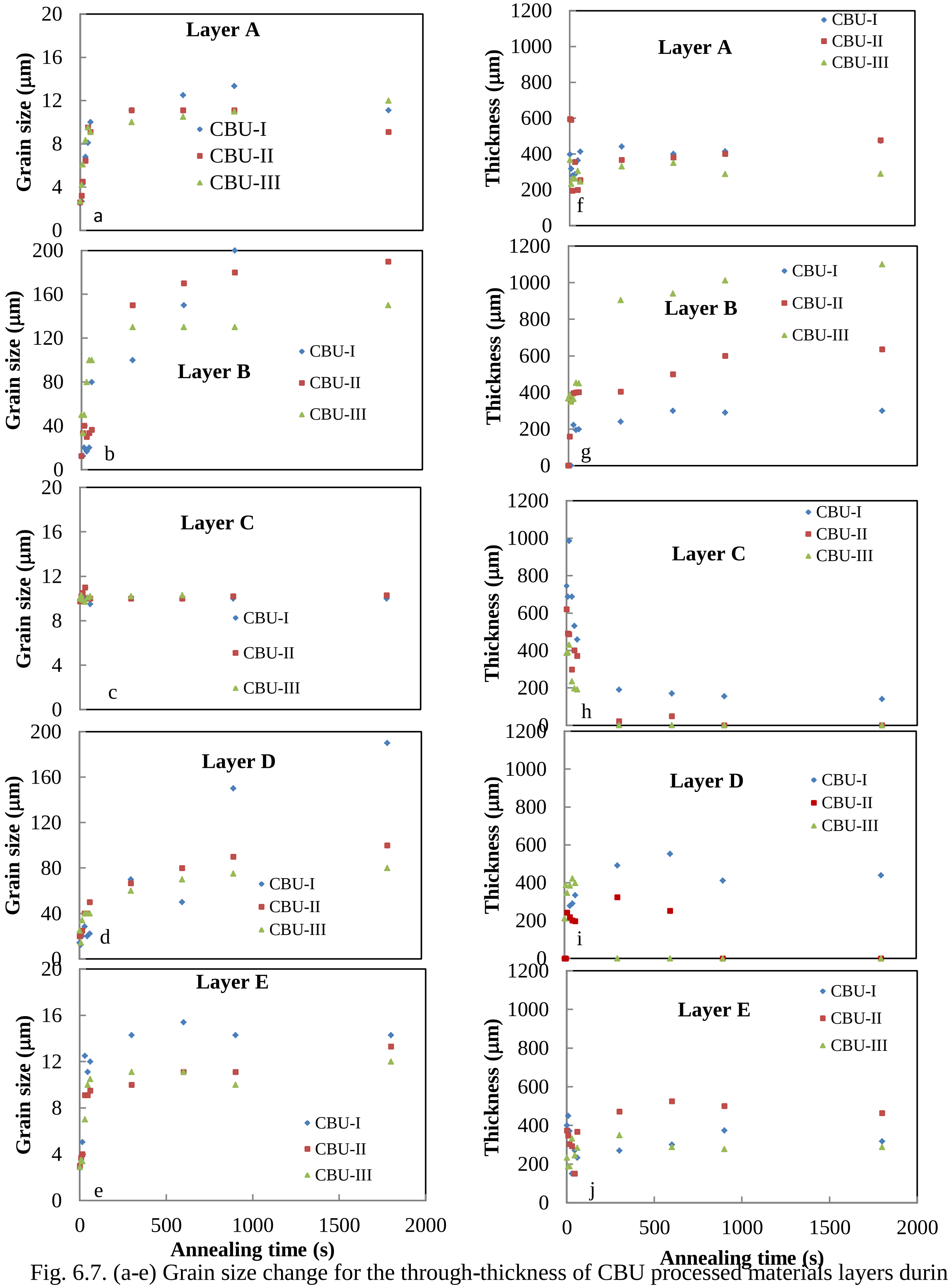

Fig. 6.7. (a-e) Grain size change for the through-thickness of CBU processed materials layers during annealing and (f-j) thickness change for the through-thickness layers during annealing.

[6.3.2]. Texture development

EBSD data from normal and short transverse planes of the annealed sheet is presented in the form of inverse pole figure (IPF) map and (0001) pole figure (PF) plot for annealed AZ31 in Fig. 6.8 where a large majority of grains are shown to have basal orientation. A strong basal texture with a maximum intensity of 9.19 is present from the rolling process at the center of pole figure.

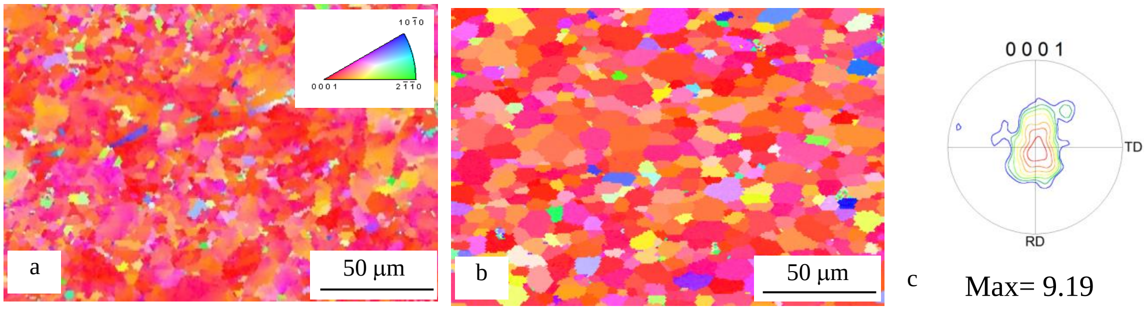

Fig. 6.8. OIM map and inverse pole figure for (a) ND plane, (b) ST plane rotated for 90˚ to be consistent with ND plane and (c){0001} pole figure from ND plane of annealed AZ31.

Through-thickness EBSD data from ST plane for CBU-III and CBUA-III samples are shown in Fig. 6.9 where a 5-layer microstructure is revealed (as earlier). Also, a rather large amount of deformation is concentrated in the surface layers A and E after CBU processing (Figure 6.9a). Mis-orientation pattern in these layers could not be reliably determined for most of the grains as they appeared dark and yielded CI and IQ values below 0.1 and 150. A few grains with $\{10\bar{1}0\}$ non-basal poles, in blue, could be observed on one side. No significant change in grain orientation through the rest of the thickness was observed as the grains stayed close to the basal pole distribution (in red and pink) after the CBU process. In contrast, CBUA process resulted in significant grain reorientation in each layer, and especially in surface layers A and E, as indicated in Fig. 6.9(b). Grains with non-basal orientations and having $\{10\bar{1}0\}$ and $\{2\bar{1}\bar{1}0\}$ poles appeared in layers A and E.

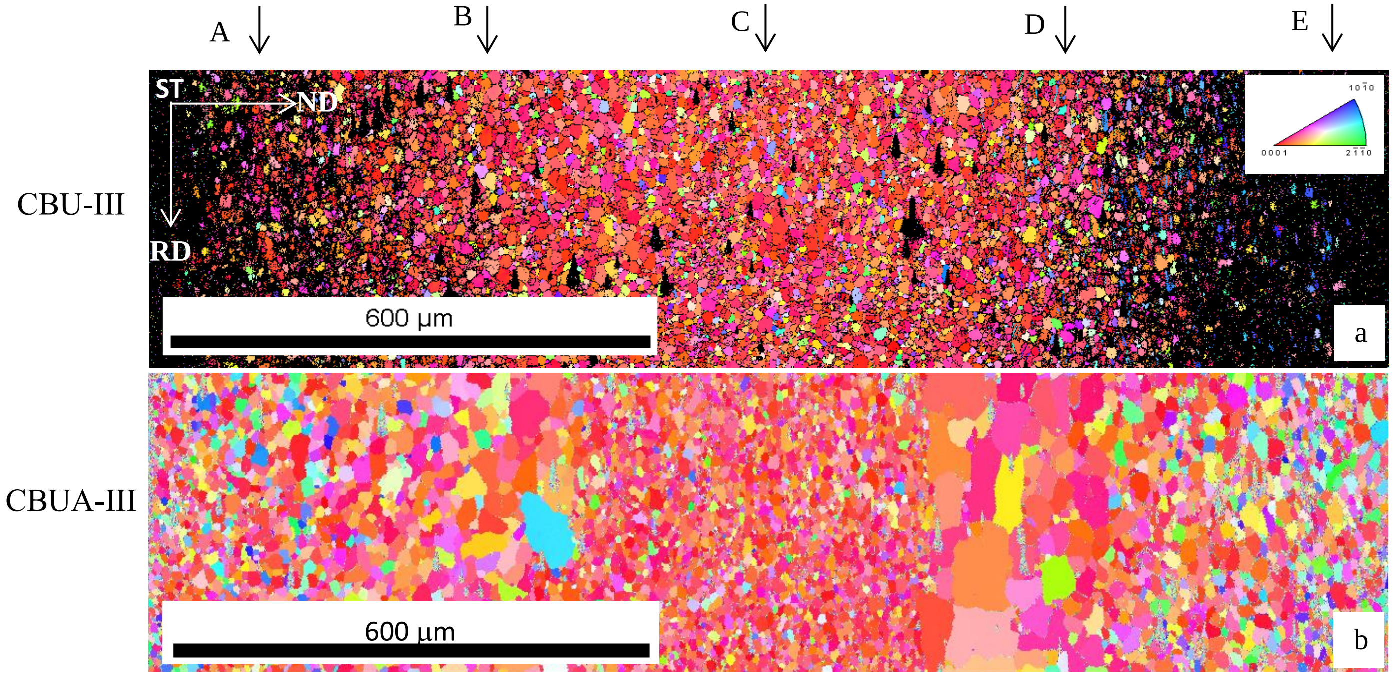

Fig. 6.9. EBSD micrographs showing the through-thickness microstructure of (a) CBU-III and (b) CBUA-III materials.

Grain reorientation tended to be less in layers B and D where grains, appearing in orange, yellow and pink, were rotated by less than 40˚ and only a few grains were left with basal orientation in the microstructure. A majority of the grains remained unchanged from their basal orientation in the mid-thickness layer C. The above observations are consistent with through-thickness (0001) pole figures of CBUA-III processed material as shown in Fig. 6.10. In surface layers A and E, a broader texture distribution was observed where the poles were roughly concentrated at 30° and 90° with respect to the original pole positions. Texture intensity was reduced in layers A and E from 9.19 in the original annealed material to 5.8 and 5.2 respectively. A bimodal pole distribution was mostly observed in the coarse grained layers B and D away from the center of the pole figure with a higher intensity pole distribution concentrated at 90˚ with respect to TD in layer B. Pole distribution was rather similar to that of the un-processed material in layer C. Texture intensity was increased in layers B and D and remained largely the same as annealed material in the mid-thickness layer C.

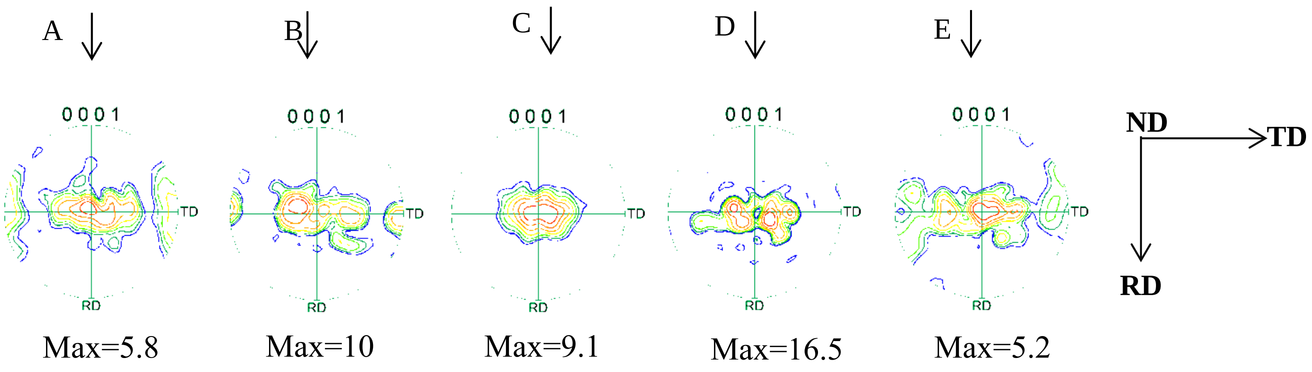

Fig. 6.10. Through-thickness {0001} pole figure of the CBUA-III processed materials for regions A to E.

[6.3.3]. Load-displacement traces from V-bending tests and bendability

Bending load versus displacement traces up to specimen failure from V-bending tests for as-received, annealed, CBU-III and CBUA-III processed materials are presented in Fig. 6.11(a). As expected, the CBU processed material shows smaller punch displacement compared to the originally annealed and CBUA processed materials. Mandrel displacement at fracture for the CBUA processed material was significantly larger than the other 3 materials. The values for CBU and CBUA materials were consistent with decreased and increased bendability respectively for the two materials as measured by the ratio of minimum radius and original sheet thickness (or $r_{\min}/t$ value) and bending angle (θ), as shown in Fig. 6.11(b). A $r_{\min}/t$ value of 2.32 for CBUA material was significantly better than that of the originally annealed material with a bendability of 2.92 (note that a lower $r_{\min}/t$ implies better bendability). Minimum bend angle, $\theta_{\min}$, was also reduced from 112.7° for annealed material to 95.9° for CBUA processed material.

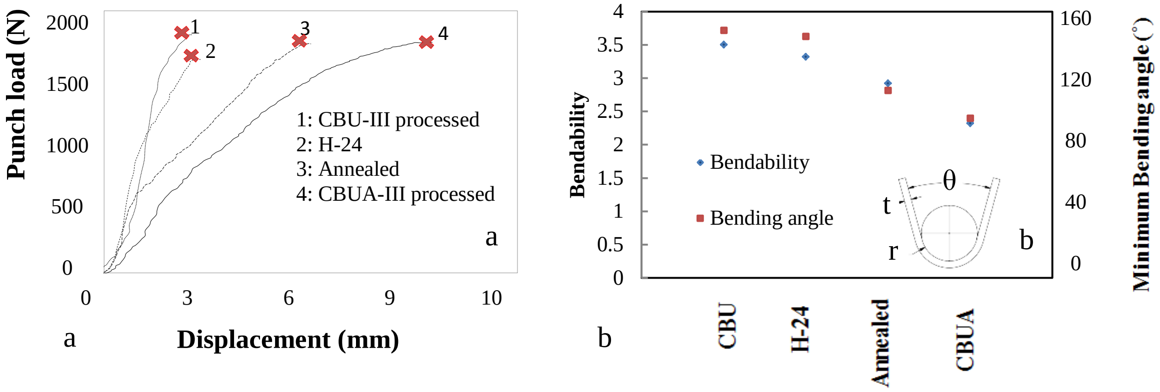

Fig. 6.11. (a) Punch load versus displacement traces from bending tests, (b) the corresponding bendability and bending angles.

Through-thickness micro-hardness profiles of as-received (H-24 temper), annealed, CBU-III and CBUA-III processed and subsequently bent materials are shown in Fig. 6.12.

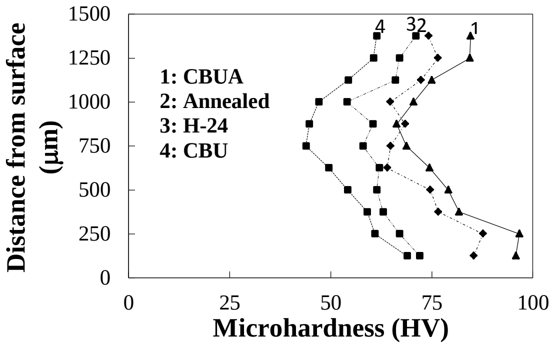

Fig. 6.12. Through-thickness microhardness profiles for the bent materials.

It is to be noted that the tests was interrupted at the start of visible crack formation when bending load started to drop. The micro-hardness values were higher for the CBUA processed material compared to CBU material and this is explained in the discussion section later. In each micro-hardness profile, layers A and E, corresponding to top and bottom of the curves respectively in Figure 6.12, showed highest micro-hardness values compared to the rest of thickness. The micro-hardness values decreased gradually to lowest in the mid-thickness layer.

Fig. 6.13 shows the LT plane through-thickness grain structure of the bent samples at the bend line. A small fraction of twins were formed during bending in H-24 material as shown in Figure 6.13(a). For annealed material with fully recrystallized grain structure, however, a higher fraction of twins were observed due to more severe bending compared to H-24, as shown in Fig. 6.13(b). Three-layer through-thickness microstructure of CBU-processed material was largely retained in bending where a large fraction of twins from the previous CBU process could be seen on the surface layers (see Fig. 6.13 (c)). CBUA material exhibited extensive twin formation and shear banding throughout the specimen thickness, with the exception of mid-thickness layer (Figure 6.13(d)). However, typical grain shape changes during bending such as significantly stretching in the tensile region and shrinking in the compressive layer were not observed in the bent specimens. Instead, twining and shear banding as mechanisms of bending strain accommodation were observed in layers A, B, D and E, but not in mid-thickness layer C, for all of the test specimens.

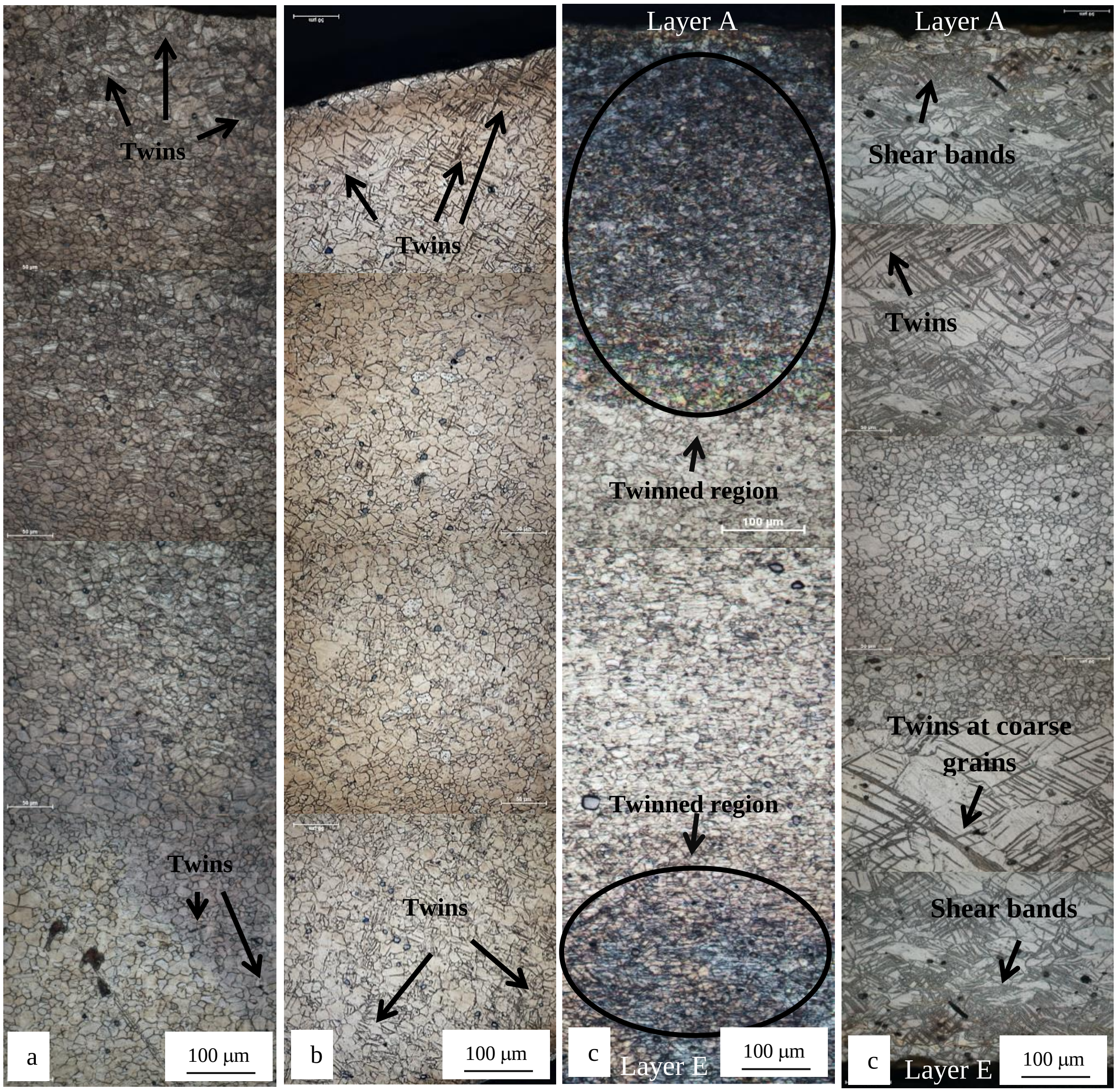

Fig. 6.13. LT plane through thickness micrographs of the bend microstructure for (a) H-24, (b) annealed AZ31 (c) CBU-III processed material and (d) CBUA-III process material.

[6.4]. Discussion

[6.4.1]. Cyclic bending-unbending process and through-thickness deformation characteristics

A schematic illustration of CBU process is shown in Fig. 6.14(a) to explain the mechanics of cyclic bending and unbending during drawing of AZ31 strip through the rolls. A single pass of CBU process subjects the material to 3 bending and 3 un-bending steps in each pass as the strip passes through the 3-roll set. Primary loading by the middle roll in CBU-I process, prior to drawing of the specimen, provides two tensions (from rolls 1 and 3) and one compression (from roll 2) to layer A, and *vice versa* for layer B. Each side of the processed sheet, therefore, is subjected to a different sequence of deformation consisting of either Tension-Compression-Tension (TCT) or Compression-Tension-Compression (CTC) over 3 passes. The stress-strain responses of AZ31 sheet in typical compressive and tensile loading are shown in Fig. 6.14(b).

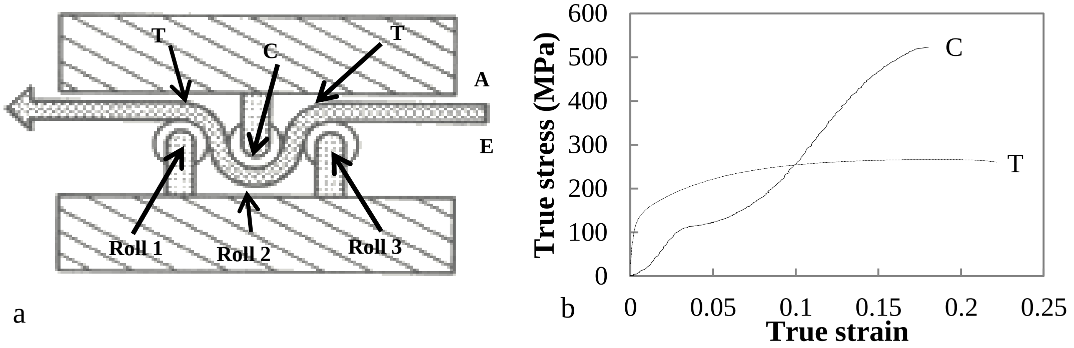

Fig. 6.14. (a) A schematic drawing of CBU process and (b) stress-strain responses of AZ31 in uniaxial tension and compression.

In uniaxial compression, AZ31 sheet typically exhibits a sigmoidal (or S-shape) hardening curve revealing a lower yield stress compared to that in tension, and a lower initial hardening rate due to twinning [16]. At large compressive strains, however, deformation is dominated by slip and flow stress curve acquires a typical convex shape. In uniaxial tension, the flow behavior consists of a slip dominated uniform region of work hardening followed by early saturation in flow stress at large strains giving rise to asymmetric flow curves in uniaxial tension and compression [16, 17]. Uniaxial CTC and TCT deformations, however, exhibit unusual sigmoidal flow stress curves on reverse loading [17, 18]. For the CTC process, the reverse loading in tension activates a de-twining mechanism in previously twinned grains from compression, a deformation process that continues on any of the six available twinning planes depending on the critical resolved shear stress. However, only one of the six planes reorients the twinned region back to the parent orientation [17-19]. Other variants of the twin can give rise to new twinned orientations, referred to as re-twinning, and randomize the texture of CBU and CBUA materials, as shown in Figs. 6.9 and 6.10. Extension twins form during compression loading due to the loading axis being perpendicular to the c-axes of majority of grains oriented with basal texture (Figs. 6.4 and 6.15). As shown by point-to-point mis-orientation data in Fig. 6.15, formation of primary and secondary twins in the outer layers A and E leads to reorientation of basal poles towards the loading direction [20].

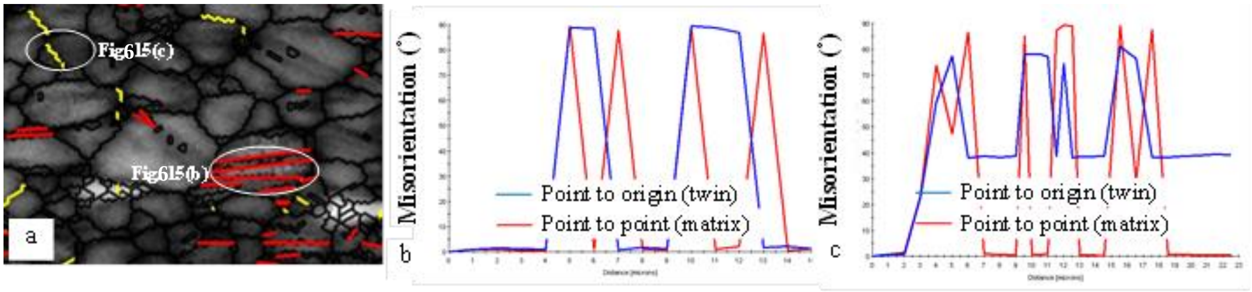

Fig. 6.15. (a) Reconstructed EBSD map showing the twins distribution in region B, (b) point-to-point misorientation analysis of extension twins and (c) point-to-point misorientation analysis of double twins.

A comparison of twin fraction of layers A and E in Fig. 6.3 suggests more twinning on one side in the CTC pass compared to TCT pass due to additional compressive loading in a 3-pass schedule.

In order to roughly estimate the cold work remaining in the test strip, through-thickness micro-hardness values before and after each annealing step during CBUA process were obtained. Fig. 6.16(a) shows higher micro-hardness values at the outer and inner fibers (layers A and E) of CBU-I processed material compared to the interior layers B, C and D. The transition regions (shown by arrows in the Figure) were observed to be about 600 μm away from the two surfaces for all CBU processed materials. This conforms well to the through-thickness microstructure of CBUA processed material presented earlier in Fig. 6.3(a) where the layer C was observed at the same location from the surface. Deformation induced by the rolls adds up cumulatively for all 3

CBU processes resulting in similar residual stress profiles through the thickness (see micro-hardness profile in Fig. 6.16(a)). This appears consistent with EBSD data presented earlier in Fig. 6.9(a) where highly deformed grains were seen on the surface layers and less deformed grains were observed at the center. CBU process does apply some uniaxial tension to the strip specimen during drawing through the rolls. Its contribution to plastic deformation is likely negligible due to application of a thick lubricant film on strip surface prior to drawing. It is worth noting that somewhat larger micro-hardness values were obtained in CBU-III process compared to CBU-I and CBU-II possibly due to increased work hardening contributions over the previous passes in comparison to thermal softening from incomplete intermediate annealing. Micro-hardness profiles remained largely unaltered after annealing (i.e., in the CBUA process) as shown in Fig. 6.16(b), although, a slight drop in micro-hardness values was observed. There appears to be a clear distinction in micro-hardness values from layer A to layer E. Since surface layers A and E were subjected to a larger amount of cold work and contained larger number of fine grains on annealing, they exhibited higher micro-hardness values compared to the other layers as shown in Figure 6.16(b). Conversely, lower micro-hardness values corresponded generally to intermediate layers B and D which contained smaller number of grains due to grain coarsening. In between the CBU passes, the elastic strains were released due to unloading but plastic strains, as well as asymmetric elastic residual stresses, remained in the material after unloading. The latter resulted in development of curvature (or springback) in the strip after it exited from the rolls.

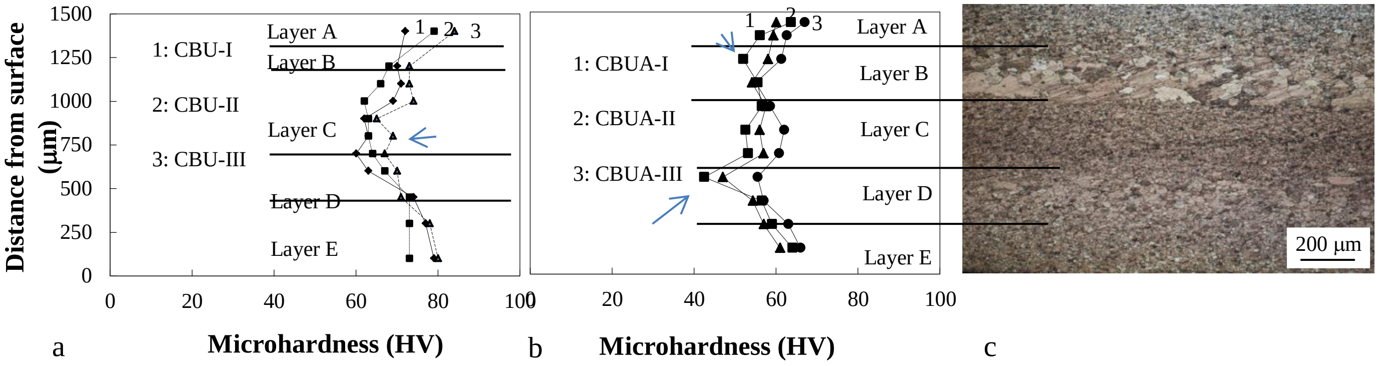

Fig. 6.16. (a) Through-thickness microhardness profile for the CBU processed materials, (b) through-thickness microhardness profile for the CBUA processed materials and (c) resulted microstructure in CBUA materials. Arrows show the transition regions.

[6.4.2]. Recrystallization and grain growth behavior during CBUA process

Redundant cold work and permanent deformation during the CBU process act as a 'driving force' for subsequent recrystallization and grain growth during annealing. Redundant cold work due to stress reversals that occur in each pass (for example, TCT), and possibly aided by a strength-differential effect in tension and compression, results in reduced dislocation density and driving force for recrystallization [21]. A slower recrystallization in turn is likely to result in larger recrystallized grain size. Thus, the redundant work is expected to play less of a role in grain recrystallization of the surface grains as well as in the growth of the interior grains. In fact, redundant cold work has been reported to be only 65% as effective in providing the driving force for recrystallization compared to permanent deformation [22]. Surface layers A and E of the multi-layered microstructure are characterized by more severe plastic deformation, and dense dislocation network from the CBU process and thus yielding higher micro-hardness values as shown earlier in Figure 6.16(a)). Consequently, these layers exhibit a higher rate of softening on annealing as shown earlier in Figure 6.6. It is likely that strain induced boundary mobility (SIBM) occurs in surface layers during the CBUA process that leads to recrystallization of new dislocation-free grains within twin and grain boundaries [21]. In addition, the stored cold work (or permanent deformation) in these layers is large enough to complete the recrystallization (but no grain growth) resulting in a fine recrystallized grain size (see Figure 6.17(a)).The layers B and D, adjacent to layers A and E respectively, however, receive a lower amount of stored cold work from the CBU process as indicated by their lower micro-hardness values in Fig 6.16(a,b). The grain coarsening initiates within these layers and continues towards the mid-thickness layer C, but not towards the outer layers A and E, as shown earlier in Fig. 6.3(d-f). It is possible that layers B and D do not coarsen towards the surface layers because of the larger fraction of twins (and partially recrystallized grains on twins) in these layers. This could be attributed to lower mobility of twin boundaries compared to grain boundaries in Mg alloys and sluggish growth of grains nucleated in the twins [23, 24]. On the other hand, mid-thickness layer C with smallest amount of cold work during CBU process (and lowest hardness values, Figure 6.16(a)), remains below the critical amount of cold work for activation of recrystallization. Consequently, this layer is consumed by rapidly growing grains of layers B and D.

Cumulative through-thickness cyclic plastic deformation that occurs over 3 CBU passes as reflected by the micro-hardness values in Figure 6.16(a) results in varying amount stored cold work through the sheet thickness. This can lead to abnormal grain growth after recrystallization in regions such as layers B and D where stored cold work is lower [22]. This is also supported by separate experiments involving monotonic pre-straining in uniaxial tension followed by annealing where a smaller pre-strain of 0.05 led to significant abnormal grain growth but larger pre-strains (in the range 0.10-0.17) resulted in a more uniform grain growth. The grains within layers B and D with many sides and characteristic concave shaped boundaries were observed (see Fig. 6.17(c,d)).

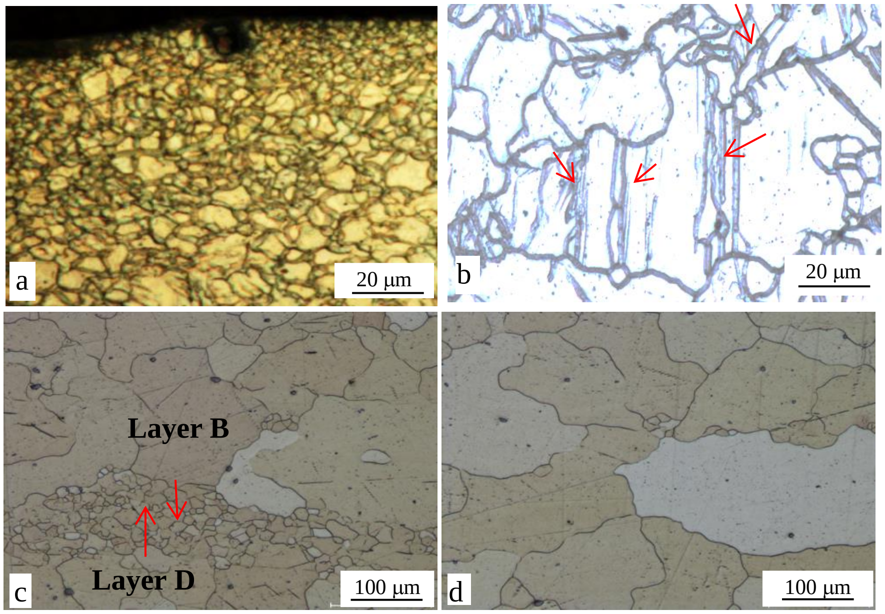

Fig. 6.17. Optical micrographs showing the microstructure of AZ31 deformed by CBU-III process and annealed at 400˚C for (a) layer A after 30s, (b) layer B after 10s, (c) layers B, C and D after 900 s, (d) layer C after 1800 s. Arrows in Figure 6.17(b) point to twin induced recrystallization and in Figure 6.17(c) point at the growth direction.

Such grains likely possessed higher curvature (and driving force) resulting in grain coarsening at the expense of neighboring grains from layer C. Further, preferred grain mis-orientation may have played some role in grain coarsening as discussed in the following section.

[6.4.3]. Texture evolution through the thickness in CBUA processed materials

The texture modification in CBUA processed AZ31 sheet results from two primary mechanisms, grain recrystallization and grain coarsening. The first mechanism occurs mostly in the surface layers (A and E) where applied cold work is at its maximum. Due to limitation of basal slip to accommodate large deformation, the initial texture decreases in strength and new near {0001} textural components appear by slip-and twin-controlled mechanisms during CTC and TCT deformation passes. Recrystallization on these additional deformation features led to a more diffuse distribution around the pole as shown earlier in Fig. 6.10. The texture components representing twin orientations were mainly recrystallized grains on twins from annealing. However, contribution of primary twins to annealing texture in Mg alloys has been shown to be quite limited due to sluggish growth of grains nucleated within the twins [Levinson et al. [24] and Martin et al. [25]]. Although most of the twin boundaries had lost their character on annealing, as noted in Figure 6.10, some new grains still remained in the microstructure. These were recrystallized grains on secondary twins with elongated shapes similar to that of the twins themselves, as shown in Figure 6.18.

Longer annealing of CBU processed material at 400˚C for 30 minutes resulted in a more stable randomized CBUA texture as evident from through-thickness EBSD maps and PFs in Fig. 6.19. A comparison of this figure with earlier Fig. 6.9 (b) indicated that bimodal texture spreading in layers A and E became stable by further annealing. The grain coarsening that developed towards the sheet interior at longer annealing times also resulted in a more stable texture and may be advantages for the growing grains over their competitors in layers B and D. As non-basal texture became more stable compared to basal texture, the grains with non-basal orientations in layers B and D were able to consume the grains with basal orientation in mid-thickness layer C. A stable and randomized texture on annealing of deformed multi-layered grain structure in AZ31 sheet via CBUA process is a significant previously unreported observation that is thought to be responsible for bendability improvement. The extent of texture spreading without any significant reduction in thickness compares favorably with those of conventional methods based on severe plastic deformation [26-29].

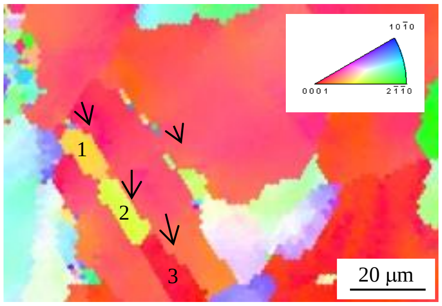

Fig. 6.18. EBSD map showing a partially recrystallized twin in CBUA-III materials. Arrows point to newly recrystallized grains on twins.

[6.4.4]. Bending behavior

From the microstructure point of view, grain structure and texture play a crucial role in affecting the limit strain in bending (i.e., bendability). The poor bendability of H-24 and annealed material could be attributed to a strong basal texture in AZ31 sheet, as shown in Fig. 6.8. It is well established that the strong basal texture yields easily activation of basal slip systems at room temperature which alone cannot accommodate general plastic deformation [30]. The work hardening history resulting from CBU process increased the stored dislocation density in the material and, as-expected, reduced its bendability. Subsequent annealing treatment via the CBUA process generated new dislocation-free grains by static recrystallization of high dislocation density layers and twinned regions.

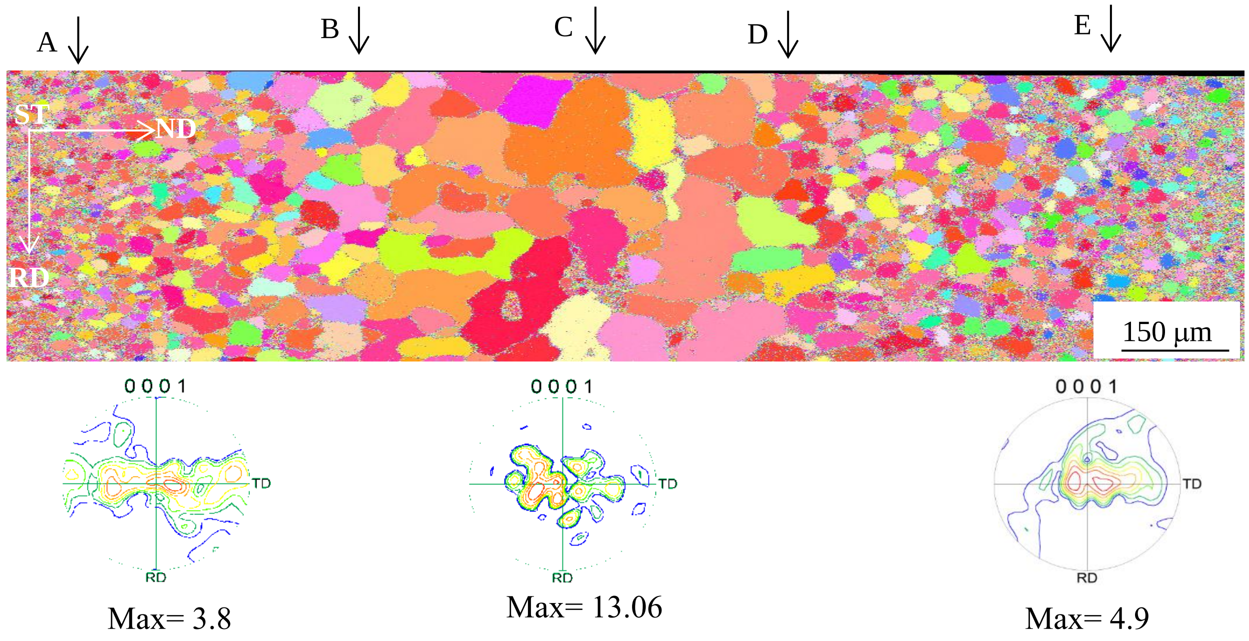

Fig. 6.19. EBSD micrographs showing the through-thickness microstructure of CBUA-III processed materials annealed at 400˚C for 30 min as well as the corresponding pole figures for each section (left, middle and right).

The newly recrystallized grains deform more readily in bending compared to the original annealed grains because of their smaller size and randomized pole distributions [31]. The grain refinement provides larger grain boundary area acting as a source of dislocations in plastic bending and offers homogeneous deformation through grain boundaries and within the grains [32]. Due to constraint applied by grain boundaries, slip could occur in several slip systems in fine-grained materials even at low strains and significantly improve bendability.

As shown earlier in Fig. 6.8, the initial rolling texture of H-24 with the c-axes of grains parallel to the center was modified with CBU process to a texture with alignment of the c-axes away from the center in different layers. Therefore, the c-axes of most grains through the thickness have been aligned along the directions that cause easier activation of slip. Further, mechanical twinning to accommodate the thickness strain is likely favored due to texture modification. A combination of these two further improves the bendability. Additionally, such grains are positioned on the surface where the bending strains are larger (see Fig. 6.12). On the other hand, relatively coarser grains with basal pole on the surface of fully annealed sheet are not able to accommodate similar level of strains and thus result in comparatively lower bendability values.

The number of twins remains largely constant in bending regardless of the punch displacement and bending angle [33]. Also, limited strain accommodation capability of twins [22] causes the shear bands to form to accommodate larger strains. A larger number of shear bands in CBUA-processed material, as shown in Fig. 6.13, is perhaps due to larger bending strains that could be accommodated compared to other processing conditions (i.e., H-24, annealed and CBU). A recent in-situ V-bending study by present authors showed that shear bands form towards the end of bending process and result in fracture due to micro-voids within shear bands that ultimately coalesce to form micro-cracks [14]. Micro-cracks grow rapidly within the shear bands due to large strain and strain rate within the band resulting in catastrophic fracture [22]. Similar damage phenomena were observed for the CBUA material (see Fig. 6.20(a)). Larger and thicker shear bands were observed in the coarser grains in layers B and D whereas smaller ones could be seen in finer grains of layers A and E due to presence of larger fraction of grain boundary in these layers (see Fig. 6.20(b)). Finally, it should be noted that there are other mechanical considerations of stress state, material specific yield criterion, material constitutive law, strain localization and surface condition which need to be studied to fully appreciate improvements in bendability of layered microstructure of CBUA material. It is likely that the overall constitutive bending response of CBUA layered microstructure will depend upon the constitutive properties of the individual layers. These aspects are, however, not in the scope of the present work.

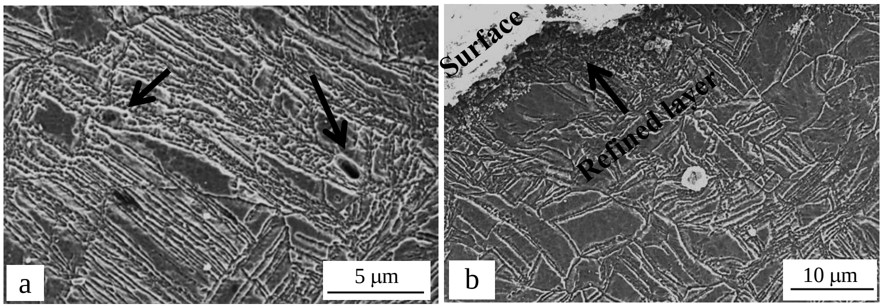

Fig. 6.20. SEM micrographs of the tensile region for CBUA material bent to a small radius of 3.5 mm showing (a) micro-cracks introduction through shear bands, (b) refined grains on side A.

[6.5]. Summary

A multi-pass cyclic bending-unbending and annealing (CBUA) technique based on drawing a sheet through a set of 3 rolls was proposed and explored as an effective sheet processing method to modify the microstructure and texture of annealed AZ31 sheet and to improve its bendability. Multi-pass cyclic bending-unbending (or CBU) process, precursor to CBUA, resulted in different fractions of twins through the sheet thickness, larger at the surface layers and smaller in the mid-thickness region, to accommodate through-thickness strains. Such a twinned structure on annealing resulted in a 5-layered, multi-size grain structure through the sheet thickness on annealing. The grain refinement was observed on the two surface layers and two coarse-grained layers were observed adjacent to the surface layers. The grain size of mid-thickness layer, however, remained the same as the original annealed grain size. On further annealing, the coarse layers grew at the expense of the mid-thickness layer but the thickness of surface layers remained unchanged. The initial basal texture of sheet was significantly modified by above processing method to create new non-basal components in each layer. Diffused texture appeared on the surface layers with progressive reduction in grain reorientation towards the mid-thickness region. Majority of the grains remained unchanged from their basal orientation in the mid-thickness layer C. Long term annealing of the CBUA processed material showed that texture randomization is stable. The grain coarsening due to preferred orientations resulted in disappearance of the basal textured grains in layer C. The overall bendability of the multi-layered material was improved as a result of grain refinement and texture spreading in CBUA processed material. The proposed processing methodology can be readily adapted to a sheet rolling mill environment to create a multi-layered magnesium sheet that has superior room bendability compared to conventionally rolled and annealed sheet.

Acknowledgments

The authors would like to thank Mr. Robert Kubic of GM R&D Center in Warren, MI, USA for his assistance with the EBSD work.

References

1. J. A. Del Valle, F. Carreno, O. A. Ruano, Acta Mater. 54 (2006) 4247-4259.
2. J. Koike, Metall. Mater. Trans. A, 36A (2005) 1689-1696.
3. J. H. Cho, H. W. Kim, S. B. Kang, T. S. Han, Acta Mater. 59 (2011) 5638-5651.

4. I. Balasundar, M. S. Rao, T. Raghu, Mater. Design., 30 (2009) 1050–1059.
5. F. Z. Hassani, M. Ketabchi, Mater. Sci. Eng. A 528 (2011) 6426– 6431.
6. G. Huang, H. Li, B. Song, L. Zhang, T. Nonferr, Metal. Soc., 20 (2010) 28-33.
7. L. Zhang, G. Huang, H. Li, and B. Song, J. Mater. Process. Tech., 211 (2011) 644-649.
8. Y. Jiang, X. Yang, L. Zhang, Mater. Sci. Forum, 667-669 (2011) 623-627.
9. Q. Huo, X. Yang, J. Ma, H. Sun, J. Qin, Y. Jiang, Mater. Charact. (2013) 43–51.
10. J. Carsley, S. Kim, J. Mater. Eng. Perform.,16 (2007) 331-338.
11. J. Carsley, Proc. Tools Mater. Sci. Tech., (2009) 10-14.
12. A. A. Luo, K. A. Sachdev, Mater. Sci. Forum, 488-489 (2005) 477-482.
13. H. Xiao, J. Liu, S. Zhang, X. Zhang, Q. Wang, Adv. Sci. Lett., 4 (2011) 1002-1006.
14. M. Habibnejad-korayem, M.K. Jain, R.K. Mishra, Mater. Sci. Eng. A. 619 (2014) 370–377.
15. M. Habibnejad-korayem, M.K. Jain, R.K. Mishra, Mater. Sci. Eng. A. 619 (2014) 378-383.
16. E. Yukutake, J. Kaneko, M. Sugamata, Mater. Trans. 44 (2003) 452-457.
17. X.Y. Lou, M. Li , R.K. Boger, S. R. Agnew, R.H. Wagoner, Int. J. Plast. 23 (2007) 44-86.
18. W. Muhammad, M. Mohammadi, J. Kang, R. K. Mishra, K. Inal, Int. J. Plast.70 (2015) 30-59.
19. M. G. Lee, R. H. Wagoner, J. K. Lee, K. Chung, H. Y. Kim, Int. J. Plast. 24 (2008) 545-582.
20. H. Wang, P. D. Wu, C. N. Tome, J. Wang, Mater. Sci. Eng. A 555 (2012) 93-98.
21. F. J. Humphreys, M. Hatherly, Recrystallization and Related Annealing Phenomena, second ed., Elsevier Ltd., Oxford, 2004.
22. E. Lindh, B. Hutchinson, S. Ueyama, Scr. Met. et Mat., 29 (1993) 347-355.
23. K. Eswar Prasad, K. T. Ramesh, Mater. Sci. Eng. A 617(2014)121–126.
24. A. Levinson, R. K. Mishra, R. D. Doherty, S. R. Kalidindi, Acta Mater. 61 (2013) 5966–5978.
25. É. Martin , R. K. Mishra, J. J. Jonas, Phil. Mag. 91 (2011) 3613–3626.
26. S. R. Agnew, J. A. Horton, T. M. Lillo, D. W. Brown, Scripta Mater., 50 (2004) 377.
27. X. Huang, K. Suzuki, A. Watazu, I. Shigematsu, N. Saito, Mater. Sci. Eng. A 488 (2008) 214.
28. Yuan W, Mishra RS. Mater Sci Eng A 2012;558:716.
29. S. R. Agnew, P. Mehrotra, T. M. Lillo, G. M. Stoica, P. K. Liaw. Mater. Sci. Eng. A 408 (2005) 72.

30. L. Wu, A. Jain, D. Brown, G. Stoica, S. Agnew, B. Clausen, D. Fielden, P. Liaw, Acta Mater., 56 (2008) 688-695.
31. L. Wang, G. Huang, H. Zhang, Y. Wang, L. Yin, J. Mater. Proc. Tech. 213 (2013) 844–850.
32. G. E. Dieter, Mechanical Metallurgy, McGraw-Hill, United Kingdome, 1988, 186.
33. I. Sato, S. Miura, T. Mohri, Mater. Sci. Forum, 654-656 (2010) 715-718.

Chapter 7
Discussion

7. Discussion

As mentioned at the beginning of the thesis, magnesium sheet materials typically do not possess enough formability in room temperature stamping application. This material limitation is being addressed by global material and manufacturing research community by developing new alloys and processing methods. For example, a new variant of commercial AZ31 sheet with rare earth element additions designated as ZEK 100 has become recently available which exhibits superior formability to AZ31 sheet [1]. With regard to processing, as mentioned earlier, many methods are now available in the literature that have shown good success, in the laboratory environment, in improving room temperature formability of magnesium sheet. The main limitations of many of the processing methods are with regard to the blank size that can be processed and the processing cost. In fact, many of the processing methods do not even target an automotive gauge sheet material and some, such as ECAP, even utilize a different starting product size and shape [2,3]. In the present research, the focus has been squarely on processing of automotive AZ31 sheet. Specifically, the interest has been in re-processing of AZ31 automotive magnesium sheet that was received in H-24 (hot rolled) temper in a manner that causes microstructural and textural changes to the sheet and yet no significant change in the sheet thickness or its flatness. Further, there was interest in exploiting processing methods that could be easily scaled up to industrial blank sizes in a cost-effective manner in the future. The two processing methods (WBA and CBUA) presented in Chapters 4 and 6 meet all of the above primary goals and both have been shown to result in useful enhancement in room temperature formability of AZ31 sheet.

In addition to re-processing of AZ31 to modify its as-received (H-24) microstructure and texture, the thesis has also focused on two multi-step pre-strain annealing processes (MUSA and MBA, Chapters 3 and 5). Both of these processes involve, as the name suggests, multiple steps of pre-straining and annealing which makes them more expensive and less efficient compared to a conventional single–step room temperature forming process that have been around for many decades for steel and aluminum sheet materials. However, both of the proposed processes do exhibit features that can be ‘tuned’ to bring the production costs and part quality to a level superior to the current high temperature forming of magnesium sheet to produce automotive components. Further, these two processes can easily accommodate various blank sizes for automotive body panel stamping applications.

Lastly, the research also focusses on development of a microstructure-based model of single step PSA process (Chapter 2). This model is shown to provide good predictions of post-anneal grain size as well as mechanical properties. Such a model can play a useful role in efficiently optimizing the selection of pre-strains, annealing temperatures and times for a single step PSA process rather than the laborious and expensive experimental trials. It is to be noted that single-step PSA process may be relevant to automotive parts that do not undergo very larger deformations. Also, the proposed modeling framework can be extended to cover multi-step PSA process in the future.

In the rest of this rather short chapter, a general discussion is presented to compare the advantages and limitations of the different processes that have been developed and analyzed in this study. Also presented in this chapter are the similarities or differences in the underlying microstructural mechanisms that have been activated via each process to improve the final formability. As explained in Chapters 2-6, room temperature deformation at uniaxial tension, plane strain bending, cyclic bending-unbending and shear modes followed by intermediate or final isothermal annealing step have been employed to develop new approaches of PSA, MUSA, CBUA, MBA and WBA. The main role of pre-deformation in all of the above processes has been identified as an ‘activator’ of different deformation features such as dislocation networks, slip bands, twins or shear bands to either directly reorient the deformed grains or provide driving force and potential sites for the subsequent recrystallization. Most of the microstructural modification takes place during thermally activated processes of annealing. The use of multi-steps (or multi-passes in CBUA) with intermediate annealing between passes (in some cases) to achieve cumulative gains in room temperature ductility and bendability was necessitated by the fact that uniform deformation in a single-step was still limited and strain localization of any kind had to be avoided.

7.1. Effect of pre-strain

Depending on the nature of applied loading, microstructure of processed sheet has been affected ‘globally’ (such as throughout the entire specimen) or locally (such as at specific layers within the sheet thickness). For example, the entire microstructure of gage length was subjected to deformation during PSA and MUSA, as the deformation occurs in the plane of the sheet during these processes. As was shown in Chapter 3, only small fraction of twins formed during deformation steps of these two processes and the rest of deformation was accommodated by slip. It was also shown that the twins contributed towards strain accommodation (as well as twin-induced fracture at large strains) in the MUSA process. During MBA process, however, the top and bottom surfaces were subjected to uniaxial tensile and compression modes of deformation and microstructure was locally modified. The twin-induced micro-crack formation during pre-bending was indeed more extensive compared to uniaxial stretching due to severe mechanical constraint arising from the plane strain condition in bending compared to the uniaxial tension. However, this provided a chance to locally modify the microstructure of these regions in annealing and continue MBA process to larger strain levels and step numbers compared to MUSA process. In WBA process, the entire surface of sheet material was subjected to severe plastic shear deformation. On the processed sheet, a highly deformed layer leading to significant modification of surface microstructure was observed after annealing. During CBUA process, each side of the processed sheet was subjected to different sequence of deformation consisting of either Tension-Compression-Tension (TCT) or Compression-Tension-Compression (CTC). Due to this complex regime of deformation, a combination of twining and de-twining occurred through the thickness. Deformation in this process was highly concentrated on the surface but the entire through-thickness microstructure and texture, including both the deformed and non-deformed layers, was modified due to subsequent grain refinement and coarsening on annealing.

7.2. Effect of annealing

7.2.1. Grain structure modification

Amount of applied deformation and extent of annealing have been recognized as governing factors in all of the above mentioned processes for grain structure modification. In all of the cases, pre-deformation provides the required driving force for subsequent annealing related phenomena including recovery, recrystallization or grain growth. The extent and rate of these mechanisms then depended on the selected annealing temperatures and times. Compared to processes such as WBA-MUSA and MBA, the as-received materials were pre-strained to larger strains and to higher fraction of recrystallization on annealing. Also, due to uniformity of deformation in MUSA and PSA processes, the grain refinement from recrystallization as well as grain coarsening occurred more evenly throughout the microstructure. However, local deformation during WBA, CBUA and MBA processes resulted in both refined and coarsened layers through some specific layers of the thickness.

7.2.2. Texture modification

A combination of complex distribution of deformation and annealing led to texture randomization in many of the developed processes. While almost no texture randomization was observed in single step PSA process, larger activation of twins and additional slip systems in MUSA process resulted in a noticeable texture randomization. Wire brushing, as presented in Chapter 4, led to introduction of shear texture due to application of severe plastic shear on the surface. This deformation mode resulted in horizontally spread of texture across the basal pole. The texture intensity then dropped on annealing while retaining much of the general characteristics of the wire brushed texture. Due to totally different regimes of deformation, Tension-Compression-Tension (TCT) and Compression-Tension-Compression (CTC), the initial texture of CBUA processed materials decreased in strength and new near basal components appeared by slip-and twin-controlled mechanisms through the thickness. Once annealing step was performed, recrystallization occurred at different rates and graded microstructure in terms of crystallographic texture resulted through the thickness from this process.

7.3. Microstructure, texture and formability

Improvement in a specific ‘formability’ property was achieved in each process. From uniaxial pre-straining and annealing (as in PSA and MUSA), for example, cumulative tensile ductility at room temperature was increased. Similarly, the material subjected to several bending and annealing steps (as in MBA) improved the monotonic and cumulative bendability. In general, grain refinement and texture randomization have been shown to improve the subsequent formability of processed sheet for most of the above mentioned processes. The effect of grain refinement in activation of other slip systems (other than basal slip system) such as prismatic slip and the effect of texture randomization to provide favorably oriented grains for activation of different slip systems could be considered for all of the processed sheets. In spite of clear disadvantages of grain coarsening towards formability improvement, this mechanism was also shown to improve twin activity at some cases (such as MUSA and WBA) which led to formability improvement. But in most of the cases, it led to ductility lost and strength drop, specifically if the grains had abnormally grown. Besides these general mechanisms, some of the approaches such as MBA, WBA and CBUA benefit from additional mechanisms. A modified layer on the surface via these processes can inhibit shear band propagation from the surface and thus delay the onset of necking and initiation of fracture in monotonic testing. On the other hand, MBA is effective in local microstructure modification between and within the voids and cracks. As microstructural observations in literature (presented in chapter 5) suggested, the void linkage has a larger influence on failure strain than the voids morphology in Mg alloys. Therefore, modification of the microstructure by grain refinement in the inter-void region in MBA could significantly retard void coalescence into fracture.

7.4. References

1. H. E. Friedrich, B. L. Mordike, Magnesium Technology: Metallurgy, Design Data, Automotive Applications, Springer Science & Business Media, 2006, Germany.
2. R.Z. Valiev, R.K. Islamgaliev, I.V. Alexandrov, Progress in Materials Science 45 (2000) 103-189.
3. B. Altan, Severe Plastic Deformation: Toward Bulk Production of Nanostructured Materials, Nova Publishers, USA, 2006.

Chapter 8
Conclusions and future work

8.1. Conclusions

The following conclusions can be drawn from the studies carried out in Chapters 2-6 of this thesis.

[1]. Pre-straining and annealing was found to be a feasible forming technique to modify the grain structure and misorientation of AZ31 and improve its tensile ductility and bendability at room temperature. Different pre-strain values, annealing temperatures and times were employed and the advantages and limitations of pre-straining and annealing (PSA) process were experimentally quantified. Depending on the PSA conditions, different responses in terms of microstructure and mechanical properties were observed from the processed sheet. Smaller values of pre-strain resulted in grain size increase and significant flow stress drop as a result of strain localization. Larger values of pre-strain resulted in grain refinement and improved cumulative ductility. A microstructure-based model was then developed to predict the static recrystallization in isothermal condition and estimate the resulted properties from PSA process. The main feature of the model was to capture the concurrent effect of recovery on both nucleation and growth of recrystallization. These allowed for prediction at different degrees of deformation during pre-straining employing non-constant nucleation rates and non-constant growth rates. The model was also successfully extended to predict the grain size change during the PSA process. Based on physical modelling of recrystallization, the resulting microstructure could be assumed as a composite of un-recrystallized and recrystallized regions to predict the mechanical properties. Also, grain coarsening was taken into account to make up for the softening due to Hall-Petch effect. In spite of limitations and simplifications, the model predictions were in reasonable agreement with the experimental results.

[2]. Experimental PSA process was further extended to multi-step uniaxial stretching and annealing (MUSA) condition. MUSA was shown as an effective process to enhance the uniaxial tensile ductility of AZ31 at room temperature. The grain size, twin fraction

and texture were shown to be affected by the MUSA process parameters. The property improvement in each step of pre-forming were quantified and found to be dependent upon pre-strain values as well as the temperature and time of intermediate annealing. Grain structure and texture modification were found to be the governing mechanisms in property improvement during MUSA process.

[3]. A wire brushing technique using modified processing parameters was utilized to modify the microstructure and tensile property improvement of AZ31. The process was found effective in fine surface grain generation and basal texture modification with good surface quality and significant improvement in room temperature uniaxial tensile ductility. Further enhancement to room temperature cumulative uniaxial tensile ductility of WBA-processed AZ31 sheet was achieved by utilizing multi-step uniaxial stretching and subsequent annealing (MUSA) method. Microstructure and texture development on AZ31 magnesium sheet surface and in the interior as well as its uniaxial stress-strain response was studied for WBA-MUSA and standard-MUSA processes. These studies revealed grain growth, twin formation within larger grains, non-basal texture development and texture spreading, and consequent changes to material work hardening behavior, as a function of number of MUSA steps.

[4]. Multi-step pre-straining and annealing was performed in plane strain bending condition resulting in improvement in cumulative bendability over a large number of intermediate pre-bending and annealing steps. The process was found as a feasible bending technique to bend AZ31 to a small radius at room temperature. Extensive deformation bands that formed in bending were replaced by new grains on annealing. The bending and subsequent annealing also promoted the local modification of the microstructure to regain some of the lost formability in the damaged areas. The grain size, especially in the micro-cracked regions, was reduced and the texture was modified by MBA.

[5]. A multi-step cyclic bending-unbending and annealing (CBUA) technique was explored as an effective sheet processing method to modify the microstructure and texture of annealed AZ31 sheet and to improve its bendability. The process resulted in graded 5-layer microstructure through the thickness of AZ31 sheet with grain refinement on the

surface, grain coarsening adjacent to these layers and unaffected layer in the mid-thickness region. The initial basal texture of sheet was significantly modified by above processing method to create new non-basal components in each layer. Long term annealing of the CBUA processed material showed that texture randomization is stable. The overall bendability of the multi-layered material was improved as a result of grain refinement and texture spreading in CBUA processed material.

8.2. Future work

This thesis presents an extension of the PSA to MUSA and MBA processes. Also, some work has been undertaken to extend PSA to biaxial out-of-plane dome tests and forming limits in the Metal Forming Laboratory at McMaster. However, to cover the entire range of forming behavior observed in automotive stamping, it would be useful to further study single and multi-step room temperature deformation behavior of AZ31 in uniaxial compression, cup drawing, stretch-bending and perhaps other combined modes of deformation.

In terms of microstructure-based modelling of single step PSA process, it would be more useful to consider a non-uniform distribution of stored energy through the microstructure which is in agreement with the experimental results. To account for the heterogeneity of deformation, one should develop a two-site model which assumes highly deformed region having high stored energy with smaller effective grain size as one site and less deformed region possessing low stored energy with larger effective grain size as the other site. The key advantage of two-site model is better prediction of grain size and properties for the heterogeneously pre-strained material. Also, the single-step model should be extended to MUSA process.

The wire brushing process could be further developed by studying wire brushing passes in different directions with respect to the sheet rolling direction. This may further remove the brush-induced scratches on the surface and provide new orientations for the texture randomization of the surface layer. Also, a microstructure based model of the wire brushing process would be quite useful in understanding the relationship between the microstructural and wire brushing parameters and the resulting mechanical responses.

The cyclic bending and un-bending process also requires further investigation in terms of intermediate annealing condition to remove the observed grain growth through the thickness of processed sheet. Also, characterization of the response of processed sheet under different mechanical testing or forming conditions could perhaps lead to exploitation of the process on a commercial-scale. Future work on this topic also requires a rigorous study by finite element modelling of the CBU process to understand the response of material in terms of neutral axis shift and residual stress distribution through the thickness.

END